TUDelft

Delft University of Technology

Multiscale microstructure-based modelling of cleavage in high strength steels

Jiang, Quanxin

Important note
To cite this publication, please use the final published version (if applicable).
Please check the document version above.

MULTISCALE MICROSTRUCTURE-BASED MODELLING OF CLEAVAGE IN HIGH STRENGTH STEELS

Quanxin JIANG

MULTISCALE MICROSTRUCTURE-BASED MODELLING OF CLEAVAGE IN HIGH STRENGTH STEELS

Dissertation

for the purpose of obtaining the degree of doctor
at Delft University of Technology,
by the authority of the Rector Magnificus prof. dr. ir. T.H.J.J. van der Hagen,
chair of the Board for Doctorates,
to be defended publicly on
Monday 27 March 2023 at 12:30 hours

by

Quanxin JIANG

Master of Science in Civil Engineering,
Delft University of Technology, Delft, The Netherlands,
born in Jinan, China.

This dissertation has been approved by the promotors.

Composition of the doctoral committee:
Rector Magnificus,   chairperson
Prof. dr. ir. J. Sietsma,   Delft University of Technology, promotor
Dr. C. L. Walters,   Delft University of Technology, copromotor
Dr. V. Popovich,   Delft University of Technology, copromotor

Independent members:
Prof. dr. ir. L.J. Sluijs   Delft University of Technology
Prof. dr. M. Veljkovic   Delft University of Technology
Prof. dr. J. Besson   MINES ParisTech
Prof. dr. J. Faleskog   KTH Royal Institute of Technology

To my grandmother 田俊玲

Contents

Summary

The need for more accurate cleavage modelling is particularly acute for a new generation of high-strength steels because they obtain their favourable properties through complex, multi-phase microstructures. One of the challenges in cleavage modelling is the strong sensitivity to material characteristics at the microlevel. Recent developments of the local approach attempted to utilize multiple-barrier models to relate the microstructural behaviour to the continuum-level properties. However, a physics-based relation between microstructure, micromechanisms of cleavage fracture and macroscopic fracture toughness is still missing. This thesis proposes a novel framework that can quantitatively capture the interaction of complex microstructural aspects in cleavage, allowing to calculate the probability of cleavage failure in high strength steels of complex multiphase microstructures. This method is validated with detailed experiments on different types of steels and on steels that have been subjected to heat treatments.

The framework is developed in Chapter 4 from a multi-barrier theory with the particular intention to include the effect of plastic strain and deactivation of hard inclusions. In order to quantitatively determine the inclusion stress from far-field stress on a matrix, analytical equations are first derived in Chapter 3. This solution is validated for different inclusion shape, inclusion orientation, far-field stress state and matrix material properties by finite element modelling of a representative volume element containing a hard inclusion.

In Chapter 4, the proposed framework is first validated with examples of specimens taken from a S690 QT steel plate fractured at -100°C. Centreline segregation bands (CLs) are present in the middle-section specimens, containing smaller grains and elongated inclusion clusters. Two modelling approaches are compared to discuss the effect of CLs in cleavage modelling. A sensitivity study is performed to explore the influence of volume fractions, yield strength, and spacing of CLs.

Then, the modelling approach proposed in Chapter 4 is applied to determine the cleavage parameters across different types of steels in Chapter 5. Cleavage parameters are compared among three tempered bainitic (S690) steels, an as-quenched martensitic steel, and a ferritic steel. The top quarter and middle sections of the S690 steels are separately modelled in terms of tensile properties, grain sizes, inclusion distribution, and cleavage parameters. The other two types of steels are studied for a single thickness position. The variation of cleavage parameters is discussed considering the influence of the matrix types and the hard particle types.

The modelling approach proposed in Chapter 4 is used to model the cleavage behaviour of heat treated S690 steel at -100°C and -40°C in Chapter 6. Cleavage simulations of the steel after rapid cyclic heating and of microstructures representing heat affect zones are performed. The simulations

are compared with experiments that feature parametric variations of grain size, second-phase particle size, and second-phase particle density. The effect of different types of microstructures generated by heat treatments is quantitatively established.

This research delivers a unique functional tool for toughness optimization, where microstructural aspects, structural geometry and performance constraints can be simultaneously taken into account. The proposed framework serves as a link between the material microstructure and the structural performance of a component, which constitutes a bridge between material process information and structural performance. It can be used to aid the material and weld designers to perform trade-offs between various microstructural parameters for control of toughness; optimizations that would otherwise require extensive trial-and-error experimentation.

Samenvatting

De behoefte aan nauwkeuriger modellering van brosse breuk is bijzonder acuut voor een nieuwe generatie hoogsterktestaalsoorten, aangezien deze hun gunstige eigenschappen verkrijgen door complexe, multi-fasige microstructuren. Een van de uitdagingen bij breukmodellering is de sterke gevoeligheid voor materiaaleigenschappen op microniveau. Recent zijn er ontwikkelingen geweest op basis van een lokale aanpak, die probeerden gebruik te maken van modellen die meerdere barrières veronderstellen om het microstructurele gedrag te koppelen aan de eigenschappen op continuüm-niveau. Echter, een fysisch gebaseerde relatie tussen microstructuren, micromechanismen van breuk en macroscopische breuksterkte ontbreekt nog steeds. Dit proefschrift stelt een nieuwe systematiek voor, die de interactie van complexe microstructurele aspecten tijdens breuk kwantitatief kan vastleggen, waardoor de kans op breuk in hoogsterktestaal met complexe multi-fasige microstructuren kan worden berekend. De methode is gevalideerd met gedetailleerde experimenten aan verschillende types staal en aan staal dat onderworpen is aan warmtebehandelingen.

De modellering wordt ontwikkeld in Hoofdstuk 4 vanuit een theorie van meerdere barrières met de specifieke bedoeling om de invloed van plastische vervorming en deactivering van harde insluitsels op te nemen. Om de spanning op een insluitsel, resulterend van de overall spanning op de matrix te bepalen, worden eerst in Hoofdstuk 3 analytische vergelijkingen afgeleid. De oplossing wordt gevalideerd voor verschillende vormen en oriëntaties van insluitsels, overall spanningstoestand en materiaaleigenschappen van de matrix door middel van berekeningen met de eindige-elementmethode van een representatief volume-element met een hard insluitsel.

In hoofdstuk 4 wordt de voorgestelde systematiek eerst gevalideerd met voorbeelden van proefstukken genomen uit een S690 QT staalplaat die is gebroken bij -100°C. Centrale segregatiebanden (CS's) zijn aanwezig in de proefstukken genomen van de middelste sectie, die kleinere korrels en uitgerekte clusters van insluitsels bevatten. Twee modelleringbenaderingen worden vergeleken om het effect van CS's in modellering van breuk te bediscussiëren. Een gevoeligheidsstudie wordt uitgevoerd om de invloed van volumefracties, treksterkte en afstand tussen CS's te testen.

Vervolgens wordt de in hoofdstuk 4 voorgestelde modelleringsbenadering toegepast in hoofdstuk 5 om de breukparameters te bepalen voor verschillende types staal. De breukparameters voor drie geharde bainitische (S690) staalsoorten, een niet-ontlaten martensitisch staal en een ferritisch staal. Het bovenste kwart en middengedeelte van de S690 staalplaten worden apart

gemodelleerd met betrekking tot treksterkte, korrelgroottes, insluitselverdeling en scheurparameters. De andere twee types staal worden bestudeerd voor één dikte-positie. De variatie van de scheurparameters wordt bediscussieerd, rekening houdend met de invloed van de matrixsoorten en de soorten harde deeltjes.

De in hoofdstuk 4 voorgestelde modelleringsbenadering wordt gebruikt om het breukgedrag van warmtebehandeld S690-staal bij -100°C en -40°C te modelleren in hoofdstuk 6. Breuksimulaties van het staal na snelle cyclische warmtebehandeling en microstructuren die warmte-beïnvloede zones representeren worden uitgevoerd. De simulaties worden vergeleken met experimenten met variabele korrelgrootte, grootte en dichtheid van tweede-fasedeeltjes. Het effect van verschillende soorten microstructuren die door de warmtebehandeling zijn ontstaan wordt kwantitatief vastgesteld.

Dit onderzoek levert een uniek functioneel hulpmiddel voor optimalisatie van de taaiheid, waarbij microstructurele aspecten, geometrie van de structuur en belastingscondities tegelijkertijd in rekening kunnen worden gebracht. De voorgestelde systematiek fungeert als een verbinding tussen het microstructurele materiaalmodel en de prestatie van een component, hetgeen een brug vormt tussen materiaalprocesinformatie en functioneren van het materiaal. Het kan worden gebruikt om materialen- en lasontwerpers te helpen bij het vinden van optimale compromissen tussen verschillende microstructurele parameters voor de beheersing van taaiheid; optimalisaties die anders omvangrijke proefondervindelijke experimenten zouden vereisen.

1

Introduction

1.1 Introduction

High strength steels are widely used in stress-critical situations, and their applications include the civil, offshore and maritime sectors. Mechanical integrity assessment of steel structures frequently requires knowledge of their resistance to catastrophic failure by fast, unstable crack growth, expressed as fracture toughness. Cleavage fracture is classified as transgranular fracture by separation across well-defined crystallographic planes. It is a very dangerous form of fracture due to the very brittle behaviour. Toughness in the lower shelf temperature region and the transition temperature region is related to cleavage fracture. Many material requirements, for example, Charpy test requirements, are therefore related to prevention of cleavage.

In most engineering applications, the trade-off between various controllable parameters (e.g. heat input, weld travel speed, process, wire composition, cooling rate, etc.) to generate both cost-effective and sufficiently tough base-metal/weld/HAZ (heat-affected zone) combination is widely accepted (e.g. [1]). These parameters have relationships with the microstructure features of the material, such as prior austenite grain size [2], carbide size [3], the presence of inclusions [4], M-A (martensite-austenite) phases [5], precipitates [6], etc.

Cleavage fracture is a highly localized phenomenon, which exhibits a strong sensitivity to material characteristics at the microlevel dependent on material and structure fabrication, and is coupled with a constraint effect originating from the loading pattern, thus being strongly related to structural design. This coupling complicates the development of fracture mechanics assessments based on available standard specimen data.

Current structural integrity assessment procedures for steels focus on the utilization of fracture specimens (*J*-Integral, K_{IC}, CTOD – Crack Tip Opening Displacement) to experimentally measure fracture toughness. These experiments can be particularly expensive for thick (> 60 mm), high strength steels because they require very high forces. Fracture testing is especially costly when new

materials or processes are being considered, and material samples need to be fabricated for testing in a design iteration loop. Moreover, measurement of steel fracture toughness is accompanied by large scatter [7], which is mostly caused by microstructural and metallurgical inhomogeneities, especially in the case of multiphase steels. Welded structures, which include different heat affected zones, commonly exhibit a heterogeneous microstructure with specific microstructural features and their own characteristic properties. In thick section steels (> 60 mm), scatter in results is inevitable due to a gradient of cooling and limited hardenability, through-thickness variation exhibiting coarse and fine microstructures, as well as a combination of multiple phases (e.g. [8]). The rolling of thick plates can also give rise to so-called segregation bands or spatial segregation of both alloying and impurity elements (e.g. [9] [10]). The consequence of such inhomogeneous and multiphase microstructures is a large scatter of properties through the thickness (e.g. [5]). A probabilistic approach is therefore required, as a fully (physics-based) deterministic model would require an unfeasible computational power for the foreseeable future.

This is especially acute for a new generation of high and very high-strength steels (yield strength of 500 to 1000 MPa), because they have generally lower toughness, and therefore, the safety margin becomes a more critical driver. Furthermore, these classes of steels obtain their favourable properties through their complex microstructures. Such steels may present complex microstructural characteristics, chemical composition and stress states, which can all affect fracture resistance. This complicates the guarantee of quality and avoidance of catastrophic cleavage-driven failures. As the tendency in the offshore and maritime industries is towards designing for higher loads, the use of high-strength steels and thick sections is becoming more common. This poses new challenges for production and often requires new and/or updated rules and regulations to ensure structural safety. Hence, to judge the susceptibility of such steel structures to catastrophic failures, a quantitative, physics-based method taking into account the statistical and multi-parametric nature of steel microstructures is required.

1.2 Research objectives

This research aims to establish a physics-based statistical relationship between multiple critical microstructural parameters and macroscopic fracture toughness. The research objectives of this thesis are:

- Development of a microstructurally informed statistical model for cleavage fracture that accounts for several microstructural features simultaneously.

- Demonstration of the model by a *posteriori* simulation, and validation of the model by a priori prediction of fracture behaviour.

- Identifying physical complexity governing cleavage crack initiation and propagation.

- Development of physics-informed relationships between microstructural parameters and macroscopic toughness.

A framework is developed from a multi-barrier theory in this thesis to calculate the probability of cleavage failure in high strength steels containing complex multiphase microstructures. This framework quantifies the relationship between microscale cleavage events and macroscale fracture toughness in a decoupled method, by incorporating microstructural information with continuum level stress-and-strain field from finite element analysis. Analytical equations to quantitatively calculate the stress on a hard inclusion from far-field stress on a matrix are first derived in order to allow the consideration of plastic strain and deactivation of hard particles in the framework. The framework is validated through micromechanical and macroscopic experiments. Physical complexity governing cleavage crack initiation and propagation are studied with the model for different type of steels and steels with heat treatments. This research delivers a new functional tool for toughness optimization, where microstructural aspects, structural geometry and performance constraints can be simultaneously taken into account. It can be used to facilitate the material and weld designers to perform trade-offs between various microstructural parameters in toughness control and optimizations that would otherwise require extensive trial-and-error experimentation.

1.3 Outline

This thesis contains one introduction chapter, one literature review chapter, four main research chapters, and one final concluding chapter. The outline is summarized below:

Chapter 2 reviews the recent development of cleavage fracture modelling in steels and identifies the existing challenges. The complex multiparametric nature of the microstructures of high strength steels and its influence on cleavage fracture is introduced. A review is given on the main perspectives and models of micromechanisms of cleavage fracture in steels. Discussion is focusing on the link between micromechanisms and the local approach in cleavage fracture modelling. As a result, the chapter gives the state of the art on microstructural mechanics and local approach methods of cleavage fracture modelling in structural steels.

Chapter 3 presents analytical equations to quantitatively determine the stress of the microstructural inclusions from the far-field stress of the matrix. The analytical equations account for the inclusion shape, the inclusion orientation, the far-field stress state and matrix material properties. Finite element modelling of a representative volume element containing a hard inclusion shows that the equations provide an accurate representation of the local stress state. The equations are implemented into a multi-barrier model and compared with three-point-bending experiments with two different levels of constraint.

Chapter 4 presents a multi-barrier model for cleavage that is modified to include the effect of plastic strain and deactivation of hard inclusions. The analytical equations derived in Chapter 3 is used in the model developed in Chapter 4 to calculate the representative stress in brittle particles. Thick-section S690 QT steel is modelled with the proposed model. Segregation bands are modelled as discrete layers which have different grain size, yield properties, and local fracture parameters from outside the bands. The results show that embrittlement from segregation bands can only be adequately reflected if the inhomogeneities of the fracture parameters are accounted for. The present methodology quantitively captures the combined effects of complex microstructural features in cleavage.

Chapter 5 determines mesoscale cleavage parameters corresponding to fracture initiation at a hard particle and crack propagation overcoming grain boundaries for three bainitic steels, a martensitic steel, and a ferritic steel. The variation of cleavage parameters is discussed considering influence of the matrix types and the hard particle types. The determined cleavage parameters present a much lower variation relative to other methods, which allows the further application on microstructure design to control macroscopic toughness.

Chapter 6 applies the microstructure-based method presented in Chapter 4 to model the cleavage behaviour of heat treated S690 steel. Cleavage simulations of steel after rapid cyclic heating and of Gleeble simulated heat affect zones are performed. The simulations are compared with experiments that feature parametric variations of grain size, second particle size, and second particle density. This study can help inform the trade-off between microstructural parameters, and helps a designer choose a process for controlling toughness.

The final Chapter 7 concludes the thesis and gives the recommendations for possible future work. The connections are also discussed from the conclusions obtained from each chapter.

Reference

[1] EN 1011, CEN (2009). Welding – Recommendations for welding of metallic materials.

[2] Li, X., Ma, X., Subramanian, S.V., Shang, C., Misra, R.D.K. (2014). Influence of prior austenite grain size on martensite-austenite constituent and toughness in the heat affected zone of 700MPa high strength linepipe steel. Mater Sci Engng, A, 616: 141–147.

[3] Lee, S., Kim, S., Hwang, B., Lee, B.S., Lee, C.G. (2002). Effect of carbide distribution on the fracture toughness in the transition temperature region of an SA 508 steel. Acta Mater, 50(19): 4755–4762.

[4] Zhou, M..W, Yu, H. (2012). Effects of precipitates and inclusions on the fracture toughness of hot rolling X70 pipeline steel plates. Int J Miner Metall Mater,19(9): 805–811.

[5] Popovich, V.A., Richardson, I.M. (2015). Fracture toughness of welded thick section high strength steels and influencing factors. In: The Minerals, Metals & Materials Society, editor. TMS 144th annual meeting & exhibition: 1031–1038.

[6] Trampus, P. (2007)Micro structural aspects of unstable crack propagation in ferritic steels. Mater Sci Forum 537–538:465–472.

[7] Wallin, K. (1984). The Scatter in KIC Results. Engineering Fracture Mechanics, 19(6), 1085–1093.

[8] Di, X., Tong, M., Li, C., Zhao, C., & Wang, D. (2019). Microstructural evolution and its influence on toughness in simulated inter-critical heat affected zone of large thickness bainitic steel. Materials Science and Engineering A, 743, 67–76.

[9] Echeverría A, Rodriguez-Ibabe JM. Brittle fracture micromechanisms in bainitic and martensitic microstructures in a C-Mn-B steel. Scr Mater, 41:131–136.

[10] Guo, F., Wang, X., Liu, W., Shang, C., Misra, R.D.K., Wang, H., et al. The Influence of Centerline Segregation on the Mechanical Performance and Microstructure of X70 Pipeline Steel. Steel Res Int, 89(12): 1800407.

1

2

Cleavage fracture modelling in steels: aspects on microstructural mechanics and local approach methods

The contents of this chapter have been published as a review article in Proceedings of the ASME 2019 38th International Conference on Ocean, Offshore and Arctic Engineering. Volume 4: Materials Technology. Glasgow, Scotland, UK. June 9–14, 2019.

Abstract

This chapter reviews the recent development of cleavage fracture modelling in steels and identifying the existing challenges to inspire further research. The chapter contains three parts aimed at explaining how methods are developed and utilized to predict fracture toughness of steel from its microstructures. (1) The complex multiparametric nature of the microstructures of ferritic steels and its influence on cleavage fracture is introduced. (2) A review is given on the main perspectives and models in micromechanisms of cleavage fracture in steels. (3) Discussion is contributed to the link between micromechanisms and the local approach in cleavage fracture modelling. As a result, the chapter gives a state of the art on microstructural mechanics and local approach methods of cleavage fracture modelling in structural steels.

2.1 Introduction

Steel structures operated in low-temperature offshore environments require the use of analysis methods that are capable of reliably predicting cleavage (brittle) fracture of high strength steels in order to guarantee the structural integrity during service. Rules and criteria for mechanical conditions based on test conditions have been established for valid fracture toughness measurements, such as J-Integral,

K_{IC}, CTOD (e.g. [1]]). The "global" approach models for the prediction of failure of cracked structures and components are based on the development of linear elastic fracture mechanics (LEFM) and elastic–plastic fracture mechanics (EPFM) [2]. In this method, it is assumed that the stress field at a crack tip can be characterized by the global parameter. The material is considered to fail when that global parameter is equal to a critical value that was measured in testing.

The global approach is very useful and absolutely necessary, but there are also many limitations, especially when large-scale yielding conditions are encountered [3]. The difference between small-scale yielding (SSY) and large-scale yielding (LSY) is important for the global approach. SSY corresponds to the case where the size of the plastic area is much smaller than the size of the specimen or structure. LSY corresponds to the opposite case: the size of the plastic zone ahead of the crack tip is large relative to the geometrical parameters associated with the specimen or structure. Most of test standards in the global approach require the sample (e.g. single-notched beam) to maintain a SSY condition. However, as the fracture toughness properties continue to increase, these requirements are becoming increasingly difficult to meet. More importantly, the global approach encounters problems whenever the assumptions of testing are not met, such as the level of constraint present in the test (never purely plane stress or plane strain) or when the loading condition is different in the test than in the structure or if the strain rate is not the same in the test and the structure. This raises important issues related to transferability from testing laboratory in conditions to the large components in real structures [4]. Another limitation of the global approach is the size effect, which is usually observed when structural ferritic steels are tested in the brittle zone and the ductile-brittle transition zone. It is widely known that even in the lower shelf of the ductile-brittle transition, the fracture toughness depends on the specimen size (e.g. [5]). This is the reason why "local approach" to fracture is particularly beneficial: the parameters of models for the local approach depend only on the material and not on the geometry or loading conditions, so results should be transferable from one level of constraint (e.g. at the specimen scale) to another (e.g. at the structural scale).

Fracture toughness models for cleavage based on the local approach are typically physically-driven statistical models that account for the probability of failure based on the local stress (and sometimes strain) field. The modelling of fracture toughness is based on a local fracture criterion and then is upscaled from unit volume to a specimen. Local approach based models require two types of knowledge: (1) the micro-mechanisms of fracture process must be formulated; (2) the local stress-strain field around a stress concentration area (e.g. crack tips) must be known or calculatable through simulation. Physical events of cleavage at different size scales and influenced by multiple microstructural parameters can be reflected by local approach models. The local approach models offer a better transferability from specimens to structures and the capability to predict cleavage fracture of nonhomogeneous material.

The prediction of fracture toughness of steels based on the microstructure has received great attention, and relevant techniques have been continuously developed.

2.2 Effect of microstructures on cleavage fracture toughness

Microstructures of steels can strongly influence the cleavage fracture micromechanisms [6]. The main microstructural features governing brittle fracture initiation and propagation in steels are: grains, carbides, inclusions and M-A constituents. The impact of those features can be estimated by different parameter studies, such as size, phase, orientation, volume fraction, chemical composition and morphology ([7-10]). A review of those microstructural features and their effects on cleavage fracture is presented below.

2.3.1 Grains

The relationship between the grains and fracture behaviour of steels is more associated to the crack propagation process rather than crack initiation. The effect of grains can be divided into phases, grain size (for a specific phase) and grain orientations. Due to factors such as varying chemical composition, peak temperatures and cooling rates during heat treatments and welding, the resultant steel can be composed of multiple phases. Some examples of phases that can be found in ferritic steels are martensite, bainite (granular bainite, upper bainite and lower bainite), acicular ferrite and grain boundary ferrite ([9-12]). Each one of these phases has a specific fracture behaviour, and it will affect the global fracture behaviour of the material in different ways. For example, acicular ferrite is well known for improving fracture toughness due to its fine interlocked microstructure and high angle boundaries which act as obstacles, making crack propagation difficult ([12], [13]), while granular bainite is reported as detrimental to fracture toughness since the M-A islands are harder than the ferrite matrix, thus aiding debonding and cracking initiation ([14], [15]).

The effect of grain size on fracture toughness has also been well established in connection to the Hall-Petch equation, showing that coarse grains have lower resistance and, therefore are not able to efficiently control the crack propagation process [16]. In addition, in ferritic steels, a cleavage crack can change its propagation direction as it crosses one grain to the other due to the differences in the orientation of the cleavage planes of two neighbouring grains. For example, when an advancing crack encounters a grain with a different orientation and, consequently, a high-angle boundary, it will either require more energy for further crack propagation or a crack path change. Therefore, grain boundaries act as natural barriers in cleavage fracture, and thus might retard or even hinder further crack propagation [17].

2.3.2 Carbides

Carbides, regarded as small (average size 1-2 µm) second-phase particles, are reported in the literature as potential cleavage initiation sites. There are two possible mechanisms that carbides can nucleate cracking: decohesion and breaking [18]. The mechanism that cracks nucleate in the carbides and the effect of this feature on steel fracture behaviour varies, depending on the carbide size, shape, volume fraction and orientation of the elongated carbides in respect to the applied stress.

[11] observed that fine carbides showed a tendency to decohere from the ferrite matrix while coarse carbides tended to break. The carbide size also has an effect on the fracture stress of steel. According to Griffith's theory [19], the larger the particle, the lower its fracture stress and, consequently, the greater the probability of it cracking. Hence, coarse carbides are considered detrimental to the fracture toughness of the steel ([20], [21]).

Regarding the shape, elongated particles are prone to breaking, whilst spherical particles are prone to decohesion [21]. In addition, elongated carbides are more critical than the spherical ones due to their tendency to crack preferentially since they build more stress as a result of the fibre-loading mechanism [21].

[22] noticed that the volume fraction of carbides also played an important role in fracture behaviour of ferritic steels. However, the effect of the carbide volume fraction on fracture toughness is not so straightforward since it depends on other factors such as carbide type, size, distribution and location in the ferritic matrix (along the grain boundaries or in the grain volume). For example, in their study, an increase in fracture toughness until a carbide volume fraction of 7.4 % was observed, achieving the maximum fracture toughness value and a subsequent continuous reduction of fracture toughness to a volume fraction of 19.2 %. The authors attributed this increase of toughness to the grain size reduction caused by the carbides, that were placed along the ferrite grain boundaries, hindering their movement. Additionally, as there was no or almost no carbides in the grain volume (the crack path) they were not directly involved in the fracture formation. However, with the increase in the volume fraction of carbides, an increase in the number of carbide particles in the grain volume participating in the fracture process was observed, leading to the reduction of the fracture toughness of the steel.

Moreover, carbide orientation with respect to the applied stress is considered an important parameter affecting cracking [23]. According to [23], under tension, the more aligned the carbide is to the tensile axis, the greater the amount of microcracks formed.

2.3.3 Inclusions

Inclusions, regarded as larger (average size > 2 µm) second-phase particles, act similarly to carbides as locations for cleavage cracks to nucleate, by either breaking or decohesion mechanisms ([7], [18]).

Regarding the size and distribution, it was observed that larger inclusions as well as inclusion clusters act as weakest links allowing for brittle crack initiation and propagation ([14], [24], [25]). Furthermore, [26] observed that chemical composition of inclusions can also impact the mode of cleavage initiation and fracture toughness. In their study, sulphide inclusions showed higher fracture toughness as compared to oxide and silicate inclusions, probably due to the different thermal expansion coefficients [26]. Additionally, elongated inclusions (primarily sulphides) have been previously related to crack initiation, acting as stress concentration areas and consequently reducing the toughness compared to inclusions of globular shape [27].

2.3.4 M-A Constituents

M-A constituents are recognized as local brittle zones, essentially placed within the coarse grained HAZ and intercritically reheated coarse grained HAZ [28], in ferritic steels showing a strong influence on the deterioration of fracture toughness [8]. Cracks can be initiated in M-A constituent by delamination, breaking and decohesion from the matrix [7].

As previously mentioned, Griffith's theory [19] explains the relationship between the size of a particle/constituent and the fracture stress. Hence, increasing the size of M-A constituent leads to a reduction in its fracture stress. Consequently, there will be a greater probability of a cleavage fracture inside the M-A constituent or at the interface with the matrix ([7], [9], [29]).

M-A constituents can form different morphologies, being more elongated as in the case of the lath-form or in a block-form [9]. As M-A constituent is hard and brittle and, consequently, essentially deforming in an elastic manner, this microstructural feature is prone to stress concentration. This stress concentration is higher in lath-form morphology due to its sharp shape. Therefore, the M-A constituents with lath-form decrease the energy required for crack initiation, thus deteriorating the material toughness.

To summarize, various microstructural parameters play different roles in cleavage process as listed in Table 2.1. Those effects are not isolated; the local stress triggering crack nucleation and propagation is determined by both the overall stress level (which relates to the grain features) and the stress concentration (which relates to second phase particles); the propagation of a particle-size crack into the matrix is an interaction between grains and brittle particles. A further understanding of such phenomena requires the knowledge of micromechanisms of cleavage fracture in steels.

Table 2.1. Microstructural features affecting cleavage process

Microstructure	Parameter	Role
Grain	Size, High-angle boundary	Matrix where crack propagates
Carbide	Size, Shape, Volume fraction	Crack initiation site
Inclusion	Size, Distribution, Type, Shape	Crack initiation site
M-A constituent	Size, Shape	Crack initiation site

2.3 Micro-mechanisms of cleavage fracture in steel

Before the 1980s, it is generally recognized that fracture process is growth controlled: cleavage micro-cracks are slip-induced, progressively nucleated under the influence of plastic strain; cleavage cracks propagate unstably when the local stress exceeds a critical value [30]. In general, cleavage fracture of ferritic steels is the result of successive occurrence of three events (Fig. 2.1):

I: nucleation of the slip-induced crack at a brittle second phase particle (e.g., carbides in steels) or inclusion. Plastic flow is a necessary precursor, which might be by slip or twinning.

II: propagation of the microcrack across the particle/matrix interface under the local stress state.

III: propagation of the grain-sized crack to neighbouring grains across the grain boundary under the local stress state.
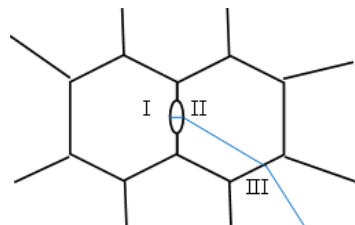
Fig. 2.1 Critical events of cleavage fracture

With increasing of temperature, the step that controlled the cleavage fracture changes from I to II and III. Experiments [31]) on simulated heat-affected zone (HAZ) of bainitic microstructures provided evidence: at low temperature, the critical step corresponded to the nucleation of micro-cracks from M-A particles; when the temperature was increased, the critical step was the propagation of packet-size micro-cracks through grain boundaries. The shift between critical steps is also proven by the observation of [12]. They compared the local stress at fracture and the transition temperature of a Ti-microalloyed steel with various grain sizes and TiN particle sizes. A critical grain size could be determined for a fixed TiN particle size. Below the critical grain size, grain size controlled the cleavage crack propagation, which means the crack propagation among grains is the critical event. Above the critical grain size, particle size controlled the cleavage crack propagation, which indicates that the

critical event is the particle-size crack propagation. These observations strongly suggest that the micromechanisms operating during fracture toughness measurements are not always the same.

Inclusions and second phase particles, as indicated in the previous section, are associated with the fracture initiation. Under plastic flow, dislocations are blocked by an inclusion or a second phase particle, which results in dislocation pile-up. The dislocation pile-up causes concentrated stress to nucleate a microcrack. Particle cracking and particle/matrix interface decohesion are the two common mechanisms of crack nucleation. [32] summarized: if the particle was brittle and deformed elastically during cracking, a one-parameter condition could be motivated for crack nucleation from linear-elastic fracture mechanics arguments (where critical-strain-based model can be transformed into a critical-stress-based model); if the fracture is due to interface decohesion, both the separation energy and interface strength need to be considered, where the local strain in the matrix material around a particle contributed significantly to the interface stress. The complexity of crack nucleation explains why both critical-strain-based models and critical-stress-based models have been used to set the criteria.

Phase boundaries and grain boundaries in ferritic steels offer an important resistance to the propagation of cleavage cracks. The resistance of those boundaries is dominated by the crystallographic misorientations. It was observed in [33] that the effect of the twist misorientation was more significant than that of the tilt misorientation. The critical stress is usually used as a criterion for the crack propagation across the particle/matrix interface or across the grain boundary. The critical stress for a micro-crack to propagate has been related to the Griffith theory based on energy balance. A general critical stress and the largest grain size map is summarized in [34]. The map confirms an approximate relation between σ_f (fracture stress) and $d^{-1/2}$ (root of grain diameter) exists. In addition, it was found in [35] that even when the energy balance (Griffith theory) was first satisfied, the crack propagation could be prevented by crack-tip blunting. Thus, stress triaxiality has also be considered as a criterion to prevent initiated crack nuclei from blunting. With higher (positive) stress triaxiality, the von-Mises stress is lower for the same value of first principal stress, which leads to more constraint to plastic deformation. The stress triaxiality criterion specifies a minimum fracture distance as stress triaxiality is relatively small in the vicinity around the crack tip. The minimum fracture distance resolves the issue that when the maximum stress is higher than the critical stress, theoretically the fracture could be produced at a point very close to the precrack tip, by a vanishingly small applied load.

It should be noticed that intergranular fracture is a competing brittle fracture mechanism to cleavage fracture and can lead to even lower fracture toughness. The appearance of intergranular fracture in the experiments to determine fracture toughness in the lower shelf will result in a larger scatter and influences the identification of parameters in the statistical representation of fracture toughness. Another remark is cleavage fracture will only occur if the critical steps I, II and III are successive in a

continuous manner. If step I has occurred and step II or III is absent, the micro-crack will be blunted and become a void, which is unable to become an unstable crack even if the local stress is increased later.

2.4 Local approach to cleavage fracture in steel

2.4.1 Single-Barrier Models

In [36] the first model based on the concept of local approach to fracture is developed: the RKR model. The occurrence of cleavage fracture in mild steels is modelled as when the critical stress value is achieved over a characteristic distance. The physical meaning of the characteristic distance is vague and relates to the grain size. The RKR model is not a weakest-link model [37], as multiple fracture events are supposed to occur along the crack front before final fracture. The original RKR model does not reflect the size effect of cleavage fracture (the thicker specimen has lower toughness). The output of the RKR model is deterministic and does not estimate the macroscopic scatter in cleavage fracture. The RKR model was then improved [30] by including a size distribution of the brittle particles that nucleate the cleavage. The improved model takes account of a statistical competition between small particles and large particles in the stress field around a stress concentration area.

The initial derivation of the macroscopic scatter in cleavage fracture was performed by the Beremin group [38]. They assume that the material contains a population of micro-defects (particles or grain-sized microcracks) distributed according to a power law $p(a)$. Two parameters are used in $p(a)$: m and σ_u. The parameter m is a shape factor characterizing the dispersion; σ_u is a measure of the "fracture resistance" of the elementary volume. It should be noted that m and σ_u are assumed as theoretically temperature independent. The failure probability of the selected volume is expressed as:

$$P_R = 1 - \exp\left[-\int_{V_p}\left(\frac{\sigma_1}{\sigma_u}\right)^m \frac{dV}{V_0}\right] = 1 - \exp\left[-\left(\frac{\sigma_w}{\sigma_u}\right)^m\right] \qquad \text{2-2-1}$$

where V_p is the plastic volume, V_0 is the elementary volume associated with m and σ_u, σ_w is the Weibull stress defined as:

$$\sigma_w = \left[\sum (\sigma_1^j)^m \frac{V_j}{V_0}\right]^{1/m} \qquad \text{2-2-2}$$

where V_j is the volume of element j.

In the original Beremin model, it is assumed that cleavage fracture cannot occur in the absence of plastic deformation, i.e., Von Mises stress below the yield strength σ_y. For finite crack tip, this means that cleavage only occurs above a K_I when plastic zone is formed ahead of the crack tip. Later, a threshold stress was introduced, and a slightly modified form of the Beremin model was proposed [39], which resolves the problem that a very small K_I leads to a finite failure probability for sharp crack tip.

Observations in various works showed that the number of microcracks nucleated from carbides increased with plastic strain. The original Beremin model has been modified in order to include the effect of plastic strain on the nucleation of microcracks ([40], [41], [42]) and the deactivation of these microcracks if they do not propagate immediately [43].

Another single barrier model was proposed in 1984: the WST model assumes that the primary cleavage initiators are brittle second phase particles like carbides [5]. However, the shape and origin of the initiator distribution is not important in the case of a ''sharp'' crack. The 1984 version of the WST model arrives at a similar result as the Beremin model. The difference is that WST model assumes an exponential law of *p(a)* and assumes that the surface energy to propagate a crack is temperature dependent. New developments of the WST model [44] are connected to a general statistical model and modified to account for plastic strain.

Fig. 2.2 shows the probability tree of the improved WST model. *Pr*{I} stands for the cumulative probability distribution for a single crack initiator (carbide) to be critical. *Pr*{I} is a complex function of the initiator size, distribution, stress, strain, grain size, temperature, stress and strain rate, etc. The cleavage fracture initiation is affected by the void formation, as the critical steps mentioned in Fig. 2.1 must be continuous. If a particle is broken but is not capable of initiating cleavage fracture in the matrix, the particle sized microcrack will blunt and a void will form. The void is no longer a brittle particle to be considered as an initiator to cleavage fracture. The probability for cleavage fracture to initiate is a conditional probability *Pr*{I/O}. Another conditional event of the cleavage fracture process is of the probability for propagation *Pr*{P/I}. An initiated cleavage crack must be able to propagate through the matrix.
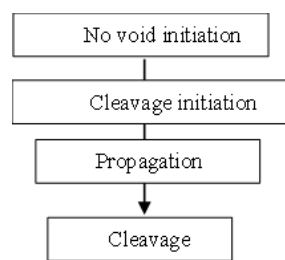

Fig. 2.2. Probability tree of WST model

Although multiple conditional events are recognized in the developing of WST model, they are not separately reflected in the final expression. For a constant temperature, the final expression of WST model can be simply written as:

$$P_f = 1 - \exp\left\{-\frac{B}{B_0}\left(\frac{K_I}{K_0}\right)^4\right\}$$

<div align="right">2-2-3</div>

2

where B is the thickness, and B_0 and K_0 are interrelated normalization parameters. When a conditional propagation criterion is included in the WST model, the term K_I will change into (K_I-K_{min}) to include a threshold parameter K_{min}, which refers to the steepest possible stress distribution enabling propagation.

The Beremin model and the WST model discussed above are the two earliest and most widely used single barrier models. In addition, other single barrier models have been developed based on similar statistical assumptions. For example, [45] proposed a model using nonlocal stress measurement with a material related length scale. A dependence on effective plastic strain is incorporated in the model, where the number of microcracks eligible to take part in the cleavage process scales with the effective plastic strain. The model contains three primary material parameters: a fracture toughness scale parameter, a threshold stress, and a material length.

The single barrier models are essentially based on the description of the propagation of an existing critical defect belonging to a single population. However, evidence indicates that the assumption may be oversimplified and lead to intrinsic contradictions. For example, when the Beremin model is applied over a wide range of temperatures, the normalizing stress σ_u is found as an increasing function of temperature [46]. This observation might reflect that there are different critical steps when the temperature range is wide. To overcome such situation, multiple-barrier models would be more satisfactory.

2.4.2 Multiple-Barrier Models

Multiple-barrier models are also based on the weakest link theory. They are distinct from single-barrier models by considering the cleavage fracture as a conditional event that is controlled by more than one barrier. The nature of these barriers depends on temperature, and the controlling event shifts between the critical steps as temperature increases. The application of these models requires the knowledge of the nucleating particle size distribution, the grain (packet) size distribution and the knowledge of local criteria to define the critical events.

The three critical steps I-III introduced in Fig. 2.1 has been widely adopted in multiple-barrier models. However, the local criteria of critical events have been treated differently. The local fracture toughness is used in [47] as a measurement of boundary crossing in steps II and III. The probability of crack nucleation is assumed as a function of particle size, grain size, local stress and local strain. A simplified expression of the nucleation probability is given as:

$$\begin{cases} p(c \leq \overline{c}/\alpha) = c/\overline{c} \\ p(c > \overline{c}/\alpha) = 1 \end{cases}$$

2-2-4

where $\overline{c}$ is the mean particle size and α is a factor depending on the local plastic strain, the grain size and the temperature.

The critical local stress to cross a particle/grain or grain/grain boundary is related to the particle or grain size by the local fracture toughness. A critical size of a particle or grain is calculated for a certain local stress level:

$$c_\sigma = \left(\frac{\beta K_{Ia}^{pm}}{\sigma_I}\right)^2 \text{ or } D_\sigma = \left(\frac{\beta K_{Ia}^{mm}}{\sigma_I}\right)^2 \qquad \text{2-2-5}$$

where c_σ and D_σ are the critical size under stress level σ, σ_I is the first principal stress, β is a geometrical factor, K_{Ia}^{pm} and K_{Ia}^{mm} are local toughness of the particle/matrix boundary and the matrix/matrix boundary.

This Griffith-like expression is similar to the expressions in the single-barrier models developed earlier. The final cleavage probability is calculated as a multiple of the probability to nucleate a crack inside the particle, to propagate the crack across particle/matrix interface and to propagate the crack across grain boundary. To reflect the volume effect, the cumulated failure probability of a specimen is an integration over the volume:

$$\phi = 1 - \exp\left\{-\int_V [N_V^g F_g(c^* \leq c \leq D^*) + N_V^c F_c(c \geq D^*)] dV\right\}. \qquad \text{2-2-6}$$

In this expression, N_V^g and N_V^c are the amount of potential cracking grains and particles per unit volume. $F_g(c^* \leq c \leq D^*)$ is the probability for the crack of size c to propagate across the grain boundary:

$$F_g(c^* \leq c \leq D^*) = \int_{D^*}^{\infty} \left\{1 - \exp\left[-N_V^c \frac{\pi D^3}{6} F_c(c^* \leq c \leq D^*)\right]\right\} m(D) f_g(D) dD \qquad \text{2-2-7}$$

and $F_c(c^* \leq c \leq D^*)$ is the probability for a microcrack of size c to nucleate and to propagate across the particle/matrix interface:

$$F_c(c^* \leq c \leq D^*) = \int_{c^*}^{D^*} p(c)\, m(c) f_c(c) dc. \qquad \text{2-2-8}$$

The critical local stress criteria have been transformed to exceeding of the critical size c^* or D^*. Parameters $m(D)$ and $m(c)$ are correction factors related to the random position of the crack in particles or grains. The parameters $f_g(D)$ and $f_c(c)$ are the size distribution functions of grain and particle.

This model is further modified in [31]. They used the same measurement of boundary crossing and fitted the value of K_{Ia}^{pm} and K_{Ia}^{mm} using experimental results. The expression of crack nucleation in particles is defined with a fitted cleavage fracture stress σ_{M-A}^c. The probability for a brittle particle to fracture is expressed by estimating the local stress inside brittle particle σ_{M-A}:

$$p(c) = \begin{cases} 1, \text{if } \sigma_{M-A} > \sigma_{M-A}^c \\ 0, \text{if } \sigma_{M-A} \leq \sigma_{M-A}^c \end{cases}. \qquad \text{2-2-9}$$

There are other two modifications: the probability of a particle size exceeding the grain size is eliminated from the final cleavage probability; and the correction factor *m* is abandoned.

The criteria used by Martín-Meizoso and Lambert-Perlade are not universally adopted, especially for the crack nucleation step. Some researchers ([48-51]) regarded plastic strain as the criterion to define crack nucleation. Stress triaxiality is also proposed as an additional criterion to prevent the crack from blunting [48]. Combined expressions of stress and stain are also proposed by [21], [52] and [53] to define the crack nucleation.

The criterion of crack propagation is always related with a critical local stress. A Hall-Petch relation between the critical local stress (σ^c) and the size (d) of grain or particle has been observed (e.g. [54]):

$$\sigma^c \propto d^{-1/2}.$$
<div align="right">2-2-10</div>

Most of the researchers use similar relations to build a distribution of critical local stress from the grain (or particle) size distribution over the volume, and relate the scatter of fracture toughness with such a distribution. However, [7] argued that the scatter of fracture toughness comes from the random location of the brittle particle, and the critical local stress (for the propagation of a second-phase particle sized crack) can be assumed as a constant value over the entire volume. This argument results in a different treatment: they assume that the probability density of failure is proportional to the active zone (where the criteria of critical steps are satisfied at an applied load), and the identification of active zone is influenced by microstructural features. The problem of this treatment is that the proportion between the probability density of failure and the active zone size is implicit and has to be determined by macroscopic experiments.

In general, multiple barrier models have stronger links to the micromechanisms of cleavage fracture and to the microstructural features of materials than the single barrier models. However, the different parameters constituting the multiple barrier models are difficult to determine.

2.5 Discussion

Table 2.2 summarizes the representative, statistical models of the local approach to cleavage fracture. The listed models provide a theoretical foundation for the statistical modelling of cleavage fracture based on local criteria. Most of the models in Table 2.2 are based on weakest link theory. However, some researchers like [55] argued that the fracture of a single domain of the aggregate could be insufficient for causing the whole aggregate fracture, particularly if the broken link is a single packet among ten others within a same primary austenite grain. They introduced the probability that I packets and only I be fractured as p_I^{pac} and the probability of grain *j* to fracture as

$$p_j^{gr} = \sum p_I^{pac} P_{I/gr}.$$
<div align="right">2-2-11</div>

The probability that the fracture of I packets leads to the fracture of their primary grain j has been predefined as: $P_{1/gr} = 0$, $P_{2/gr} = 0.5$ and $P_{I/gr} = 1$, for I ≥ 3.

It should be noticed that the boundary between single-barrier models and multiple-barrier models is not rigorous. If a prejudgment is included to determine the primary conditional event and simplify the less important conditional event as a threshold value or a predefined factor, a multiple barrier model is reduced to a single-barrier model. The single-barrier models are generally simplified approaches to take account the total effect of the barriers. More recent versions of some single-barrier models further involve the modelling of more than one barrier. For example, [56] and [57] considered the probability of crack nucleation by including the plastic strain in the expression of Weibull stress.

Table 2.2. Summary of representative models

Proposed by	Main characteristics	Definition of failure
Beremin model and its developments		
Beremin 1983	Randomness comes from distribution of microcrack length	critical stress for propagation
Gao 1998 & Anderson 1994	Account for the minimal stress required to break the boundary	critical stress for propagation (with threshold of stress)
Bernauer 1999	Account for preceding void formation.	critical stress for propagation
Gao 2005	Include the effect of plastic strain and stress triaxiality on microcrack	critical stress for propagation (with threshold of stress)
Tanguy 2005	Observed a temperature dependence on σ_u	critical stress for propagation (with threshold of plastic strain)
Boåsen 2019	Use effective stress measure associated with a material related length scale	critical stress for propagation with strain-based factor to correct fraction of fractured particles
Ruggieri 2020	Incorporate plastic strain effects	critical stress for propagation with strain-based factor to correct fraction of fractured particles
Multiple-barrier models		
Chen 1990, 2014	Randomness comes from distribution of the location of weak particles	two barriers: crack initiation (plastic strain, stress triaxiality), crack propagation (stress at P/M or M/M boundary)
Martin-Meizoso 1993 & Lambert-Perlade 2004	Randomness comes from distribution of particle size and grain size	three barriers: crack initiation (stress), propagation through P/P and P/M boundary (all defined by stress)
Bordet 2005	Randomness comes from distribution of microcrack length	two barriers: crack initiation (plastic strain), crack propagation (with a threshold stress)
Mathieu 2010	Randomness comes from distribution of particle size and location	two barriers: crack initiation (plastic strain), crack propagation (stress at P/M boundary)
N'Guyen 2012	Randomness comes from distribution of particle size	two barriers: critical stress for crack propagation, predefined conditional

2

		probability for crack pass P/M boundaries
Scibetta 2016	Account for re-initiation of micro-cracks	four barriers: crack initiation (stress, plastic strain), propagation through P/P and P/M boundary (all defined by stress), crack re-initiation (stress, plastic strain)
Shibanuma 2016, 2018	Use Monte Carlo method to model the randomness of particle and grain distributions	three barriers: crack initiation (strain-based probability), propagation through P/M and M/M boundary (defined by stress)
Yang 2021	Co-operate ductile fracture and cleavage mechanisms in the transition region with a continuum approach to estimate the effective surface energy	two barriers: propagation through P/M and M/M boundary (defined by stress)
Kunigita 2020	Use Monte Carlo method to model the randomness of particle distributions	two barriers: crack initiation (strain-based probability), crack propagation (stress at P/M boundary)
Chen 2020	Couple with the temperature dependent constitutive relationship and the competition between the cleavage and ductile void failure	two barriers: crack initiation (stress, plastic strain), crack propagation (with a threshold stress)
Other single-barrier models		
Lin 1985	Randomness comes from distribution of particle size;	critical stress for propagation
Wallin 1984, 2008	Randomness comes from distribution of particle size; Includes the effect of plastic strain and the formation of void	critical stress for propagation
Kroon 2002	Randomness comes from distribution of microcrack length; Ductile crack processing; Consider load history	nonlocal measure of stress (include length scale and threshold) and effective plastic strain

* P/M: Particle/Matrix   P/M: Particle/Matrix

The advantage of single-barrier models is that they offer simple expressions for application. Macroscopically, the WST model can be expressed in the standard master curve format. The master curve approach has been standardized in [1] to guide the assessment of fracture toughness of steel specimens. Similarly, the Beremin model is widely utilized in macroscopic assessments and has been included in engineering platforms [58]. However, identification of the Beremin parameters and master curve parameters have to be based on statistical fitting of macroscopic experimental data. The fitted parameters would in return be used to predict the fracture toughness under a certain failure probability. It leads to a paradox: although the model parameters are assumed to only depend on material, they are unable to be determined only by microstructural measurements. Recently, microscopic simulations are used to explore the link between the microstructures and the parameters of single-barrier models; for example, [33] estimated the relationship between Beremin parameters and ferrite grain size. The challenge for further exploration is that it is difficult to control one microstructural feature in real macroscopic experiments where the single-barrier model parameters are identified.

In comparison, with the help of Digital Image Correlation (DIC) and Scanning Electron Microscopy (SEM) technique, microscopic experiments can directly provide observation and measurement for multiple-barrier models. The identification and determination of the "micromechanical" parameters require a hybrid methodology of combined testing and numerical simulation. With SEM, the location of crack initiation can be identified [59]. With DIC, the local strain field near the micro-crack can be measured [60]. The measured local strain field can be used to validate or correct the result of a finite element analysis which is aimed at identifying the local criteria of critical events. Therefore, the multiple-barrier models do not need all parameters to be fitted from the macroscopic experimental results, which allows a relationship between model parameters and several microstructural features to be built. For example, [61] use the effective surface energy for microcrack propagation across grain boundary that were experimentally measured by [62]. The effective surface energy for microcrack propagation across grain boundary and particle/matrix interface is estimated from experimentally measured cleavage facets in [61].

One difficulty of the multi-barrier models is that those models are unable to give an explicit, simple expression as by the single-barrier models. However, as computational power has developed, the explicit, simple expression may not be necessary for calculation. For example, [63] developed a framework that randomly generates distributions of brittle particles and ferrite grains within a volume to simulate the three-step cleavage fracture and estimate the failure probability. They used this framework to explore the influence of virtual microstructures on the calculated macroscopic fracture toughness.

2.6 Conclusion

The microstructures of ferritic steels have a complex multiparametric nature which leads to large scatter in macroscopic toughness of cleavage fracture. This chapter reviews the main perspectives on micromechanisms of cleavage fracture in steels. Various local approach models for cleavage fracture are discussed and compared. Although those models are all based on local criteria, their link to the micromechanisms and to the microstructures are not the same. In general, multiple-barrier models can better catch the various critical steps in a wide temperature range than the single-barrier models. The parameters used in multiple-barrier models are more suitable to be measured or validated with microscopic experiments. Recent development of the local approach attempted to utilize multiple-barrier models to relate the microstructural behaviour to the continuum-level properties. Those efforts have shown great feasibility and revealed the potential of the local approach for cleavage fracture. However, they have not managed to build an experiment-based relation between microstructures, micromechnisms of cleavage fracture and macroscopic fracture toughness. The knowledge gap in modelling cleavage fracture still exists.

If current relations could be down-selected and made more empirically grounded on microstructures, then the resulting model could provide a bridge from the material microstructural models to the structural performance of a component. Therefore, providing a rigorous relationship between the microstructural models and the local approach fracture models will serve as a link between material process information and structural performance. This link, which is currently missing, will provide a powerful tool for material and weld designers to perform trade-offs and optimizations that would otherwise require extensive trial-and-error experimentation. Furthermore, a deep understanding of the statistical distribution of microstructural features and their link to the failure criteria can be applied to a wider range of materials experiencing brittle fracture

2

References

[1] EN 1011, CEN (2009). Welding – Recommendations for welding of metallic materials.

[2] Anderson, T. L. (2005). Fracture Mechanics: Fundamentals and Applications, Third Edition. CRC Press.

[3] Pineau, A., & Tanguy, B. (2010). Advances in cleavage fracture modelling in steels: Micromechanical, numerical and multiscale aspects. In Comptes Rendus Physique, Vol. 11, Issues 3–4, 316–325.

[4] Gao, X., & Dodds, R. H. (2000). Constraint effects on the ductile-to-brittle transition temperature of ferritic steels: a Weibull stress model. International Journal of Fracture, 102(1), 43–69.

[5] Wallin, K. (1984). The Scatter in KIC Results. Engineering Fracture Mechanics, 19(6), 1085–1093.

[6] Curry, D. A., & Knott, J. F. (1978). Effects of microstructure on cleavage fracture stress in steel. Metal Science, 12(11), 511–514.

[7] Chen, J. H., & Cao, R. (2015). Micromechanism of Cleavage Fracture of Metals. Elsevier.

[8] Li, X., Ma, X., Subramanian, S. V., Shang, C., & Misra, R. D. K. (2014). Influence of prior austenite grain size on martensite-austenite constituent and toughness in the heat affected zone of 700MPa high strength linepipe steel. Materials Science and Engineering A, 616, 141–147.

[9] Wang, Z., Shi, M., Tang, S., & Wang, G. (2017). Effect of heat input and M-A constituent on microstructure evolution and mechanical properties of heat affected zone in low carbon steel. Journal Wuhan University of Technology, Materials Science Edition, 32(5), 1163–1170.

[10] Zhou, M. W., & Yu, H. (2012). Effects of precipitates and inclusions on the fracture toughness of hot rolling X70 pipeline steel plates. International Journal of Minerals, Metallurgy and Materials, 19(9), 805–811.

[11] Guo, F., Wang, X., Liu, W., et al. (2018). The Influence of Centerline Segregation on the Mechanical Performance and Microstructure of X70 Pipeline Steel. Steel Research International, 89(12), 1800407.

[12] Ray, A., Sivaprasad, S., & Chakrabarti, D. (2012). A Critical Grain Size Concept to Predict the Impact Transition Temperature of Ti-Microalloyed Steels. International Journal of Fracture, 173(2), 215–222.

2

[13] Cao, Z., Bao, Y., Xia, Z., Luo, D., Guo, A., & Wu, K. (2010). Toughening mechanisms of a high-strength acicular ferrite steel heavy plate. International Journal of Minerals, Metallurgy, and Materials, 17(5), 567–572.

[14] Popovich V.A., Richardson I.M. (2015). Fracture Toughness of Welded Thick Section High Strength Steels and Influencing Factors. The Minerals, Metals & Materials Society (eds) TMS 2015 144th Annual Meeting & Exhibition. 1031-1038.

[15] Yang, Z., Liu, Z., He, X., Qiao, S., & Xie, C. (2018). Effect of microstructure on the impact toughness and temper embrittlement of SA508Gr.4N steel for advanced pressure vessel materials. Scientific Reports, 8(1), 207.

[16] Armstrong, R. W. (2015). Material grain size and crack size influences on cleavage fracturing. Philosophical Transactions of the Royal Society A: Mathematical, Physical and Engineering Sciences, 373(2038), 20140474.

[17] Liu, H., Zhang, H., & Li, J. (2018). Thickness Dependence of Toughness in Ultra-Heavy Low-Alloyed Steel Plate after Quenching and Tempering. Metals, 8(8), 628.

[18] Chen, J. H., Li, G., Cao, R., & Fang, X. Y. (2010). Micromechanism of cleavage fracture at the lower shelf transition temperatures of a C–Mn steel. Materials Science and Engineering: A, 527(18–19), 5044–5054.

[19] Griffith, A. A. (1921). The Phenomena of Rupture and Flow in Solids. Philosophical Transactions of the Royal Society A: Mathematical, Physical and Engineering Sciences, 221, 163–198.

[20] Lee, S., Kim, S., Hwang, B., Lee, B. S., & Lee, C. G. (2002). Effect of carbide distribution on the fracture toughness in the transition temperature region of an SA 508 steel. Acta Materialia, 50(19), 4755–4762.

[21] Bordet, S. R., Karstensen, A. D., Knowles, D. M., & Wiesner, C. S. (2005). A new statistical local criterion for cleavage fracture in steel. Part II: Application to an offshore structural steel. Engineering Fracture Mechanics, 72(3), 453–474.

[22] Pacyna, J., & Witek, L. (1988). The effect of carbides on fracture toughness of steels of ferritic matrix. Steel Research, 59, 68–74.

[23] Lindley, T. ., Oates, G., & Richards, C. . (1970). A critical of carbide cracking mechanisms in ferride/carbide aggregates. Acta Metallurgica, 18(11), 1127–1136.

2

[24] Ghosh, A., Ray, A., Chakrabarti, D., & Davis, C. L. (2013). Cleavage initiation in steel: Competition between large grains and large particles. Materials Science and Engineering A, 561, 126–135.

[25] Pallaspuro, S. (2018). On the factors affecting the ductile-brittle transition in as-quenched fully and partially martensitic low-carbon steels. PhD thesis. University of Oulu

[26] Miao, P., & Knott, J. F. (2016). Effects of Inclusions and Their Surface Chemistry on Cleavage Fracture in a C-Mn Steel Weld Metal. HSLA Steels 2015, Microalloying 2015 & Offshore Engineering Steels 2015, 1149–1161.

[27] Ray, A., Paul, S. K., & Jha, S. (1995). Effect of Inclusions and Microstructural Characteristics on the Mechanical Properties and Fracture Behavior of a High- Strength Low- Alloy Steel. Journal of Materials Engineering and Performance, 4(6), 679–688.

[28] Mohseni, P., Solberg, J. K., Karlsen, M., Akselsen, O. M., & Østby, E. (2012). Investigation of mechanism of cleavage fracture initiation in intercritically coarse grained heat affected zone of HSLA steel. Materials Science and Technology, 28(11), 1261–1268.

[29] Jia, T., Zhou, Y., Jia, X., & Wang, Z. (2017). Effects of Microstructure on CVN Impact Toughness in Thermomechanically Processed High Strength Microalloyed Steel. Metallurgical and Materials Transactions A: Physical Metallurgy and Materials Science, 48(2), 685–696.

[30] Lin, T., Evans, A. G., & Ritchie, R. O. (1986). A Statistical Model of Brittle Fracture by Transgranular Cleavage. Mrch. Phys. Solids, 34(5), 477–497.

[31] Lambert-Perlade, A., Gourgues, A. F., Besson, J., Sturel, T., & Pineau, A. (2004). Mechanisms and modeling of cleavage fracture in simulated heat-affected zone microstructures of a high-strength low alloy steel. Metallurgical and Materials Transactions A: Physical Metallurgy and Materials Science, 35(13), 1039–1053.

[32] Pineau, A., Benzerga, A. A., & Pardoen, T. (2016). Failure of metals I: Brittle and ductile fracture. Acta Materialia, 107, 424–483.

[33] Qiao, Y. (2003). Modeling of resistance curve of high-angle grain boundary in Fe-3 wt.% Si alloy. Materials Science and Engineering A, 361(1–2), 350–357.

[34] Miyata, T., Yang, R. C., Otsuka, A., Haze, T., & Ahira, S. (1989). Cleavage fracture of steels with fine grained ferrite, coarse grained bainitic and martensitic. Advances in fracture research Proceeding of the seventh international conference of fracture. 2563-2571.

2

2

[35] Curry, D. A. (1980). Cleavage micromechanisms of crack extension in steels. Metal Science, 14(8–9), 319–326.

[36] Ritchie, R. O., Knott, J. F., & Rice, J. R. (1973). On the relationship between critical tensile stress and fracture toughness in mild steel. Journal of the Mechanics and Physics of Solids, 21(6), 395–410.

[37] Weibull, W. (1951). A Statistical Distribution Function of Wide Applicability. Journal of Applied Mechanicsechanics, 18, 293–297.

[38] Beremin, F. M., Pineau, A., Mudry, F., Devaux, J. C., D'Escatha, Y., & Ledermann, P. (1983). A local criterion for cleavage fracture of a nuclear pressure vessel steel. Metallurgical Transactions A, 14(11), 2277–2287.

[39] Gao, X., Ruggieri, C., & Dodds, R. H. (1998). Calibration of Weibull stress parameters using fracture toughness data. International Journal of Fracture, 92(2), 175–200.

[40] Gao, X., Zhang, G., & Srivatsan, T. S. (2005). Prediction of cleavage fracture in ferritic steels: A modified Weibull stress model. Materials Science and Engineering A, 394(1–2), 210–219.

[41] Boåsen, M., Stec, M., Efsing, P., & Faleskog, J. (2019). A generalized probabilistic model for cleavage fracture with a length scale – Influence of stress state and application to surface cracked experiments. Engineering Fracture Mechanics, 214(February), 590–608.

[42] Ruggieri, C. (2020). A modified local approach including plastic strain effects to predict cleavage fracture toughness from subsize precracked Charpy specimens. Theoretical and Applied Fracture Mechanics, 105(June 2019), 102421.

[43] Bernauer, G., Brocks, W., & Schmitt, W. (1999). Modifications of the Beremin model for cleavage fracture in the transition region of a ferritic steel. Engineering Fracture Mechanics, 64, 305–325.

[44] Wallin, K., & Laukkanen, A. (2008). New developments of the Wallin, Saario, Törrönen cleavage fracture model. Engineering Fracture Mechanics, 75(11), 3367–3377.

[45] Kroon, M., & Faleskog, J. (2002). A probabilistic model for cleavage fracture with a length scale-influence of material parameters and constraint. International Journal of Fracture, 118(2), 99–118.

[46] Tanguy, B., Besson, J., Piques, R., & Pineau, A. (2005). Ductile to brittle transition of an A508 steel characterized by Charpy impact test. Part II: Modeling of the Charpy transition curve. Engineering Fracture Mechanics, 72(3), 413–434.

2

[47] Martín-Meizoso, A., Ocaña-Arizcorreta, I., Gil-Sevillano, J., & Fuentes-Pérez, M. (1994). Modelling cleavage fracture of bainitic steels. Acta Metallurgica Et Materialia, 42(6), 2057–2068.

[48] Chen, J. H., Wang, G. Z., & Wang, H. J. (1996). A Statistical Model for Cleavage Fracture of Low Alloy Steel. Acta Metallurgica, 44(10), 3979–3989.

[49] Mathieu, J. P., Inal, K., Berveiller, S., & Diard, O. (2010). A micromechanical interpretation of the temperature dependence of Beremin model parameters for french RPV steel. Journal of Nuclear Materials, 406(1), 97–112.

[50] Shibanuma, K., Aihara, S., & Suzuki, K. (2016). Prediction model on cleavage fracture initiation in steels having ferrite-cementite microstructures - Part I: Model presentation. Engineering Fracture Mechanics, 151, 181–202.

[51] Kunigita, M., Aihara, S., Kawabata, T., Kasuya, T., Okazaki, Y., & Inomoto, M. (2020). Prediction of Charpy impact toughness of steel weld heat-affected zones by combined micromechanics and stochastic fracture model – Part I: Model presentation. Engineering Fracture Mechanics, 230, 106965.

[52] Scibetta, M. (2016). A cleavage fracture framework: New perspectives in cleavage modeling of ferritic steels. Engineering Fracture Mechanics, 160, 147–169.

[53] Chen, L., Liu, W., Yu, L., Cheng, Y., Ren, K., Sui, H., Yi, X., & Duan, H. (2020). Probabilistic and constitutive models for ductile-to-brittle transition in steels: A competition between cleavage and ductile fracture. Journal of the Mechanics and Physics of Solids, 135.

[54] Petch, N. J. (1953). The cleavage strength of polycrystals. J. Iron Steel Inst., 174, 25–28.

[55] Di Schino, A., & Guarnaschelli, C. (2010). Microstructure and Cleavage Resistance of High Strength Steels. Materials Science Forum, 638–642, 3188–3193.

[56] N'Guyen, C. N., Barbe, F., Osipov, N., Cailletaud, G., Marini, B., & Petry, C. (2012). Micromechanical local approach to brittle failure in bainite high resolution polycrystals: A short presentation. Computational Materials Science, 64, 62–65.

[57] Hohe, J., Hardenacke, V., Luckow, S., & Siegele, D. (2010). An enhanced probabilistic model for cleavage fracture assessment accounting for local constraint effects. Engineering Fracture Mechanics, 77(18), 3573–3591.

[58] Bugat, S., Zeghadi, A., & Adjanor, G. (2010). A not-so-short description of the PERFECT platform. Journal of Nuclear Materials, 406(1), 166–174.

[59] Mckenzie, F. (2014). Assessment of Local Cleavage Initiation Conditions and Fracture Surface Topography. University of Manchester.

[60] Diehl, M. (2016). High-Resolution Crystal Plasticity Simulations. PhD Thesis. RWTH Aachen.

[61] Li, Y., Pallaspuro, S., Ren, X., He, J., Kömi, J., & Zhang, Z. (2021). A multi-barrier model assisted CAFE method for predicting ductile-to-brittle transition with application to a low-car bon. Mechanics of Materials 153, 103669.

[62] Kawata, I., Nakai, H., & Aihara, S. (2018). Experimental evaluation of effective surface energy for cleavage microcrack propagation across grain boundary in steels. Acta Materialia, 150, 40–52.

[63] Shibanuma, K., Nemoto, Y., Hiraide, T., Suzuki, K., Sadamatsu, S., Adachi, Y., & Aihara, S. (2018). A strategy to predict the fracture toughness of steels with a banded ferrite–pearlite structure based on the micromechanics of brittle fracture initiation. Acta Materialia, 144, 386–399.

2

3

Relating matrix stress to local stress on a hard microstructural inclusion for understanding cleavage fracture in high strength steel

Abstract

Macroscale cleavage fracture toughness of high strength steels is strongly related to the fracture of hard microstructural inclusions. Therefore, an accurate determination of the local stress on these inclusions based on the matrix stress is necessary for the statistical modelling of macroscale cleavage fracture. This paper presents analytical equations to quantitatively estimate the stress of the microstructural inclusions from the far-field stress of the matrix. The analytical equations account for the inclusion shape, the inclusion orientation, the far-field stress state and matrix material properties. Finite element modelling of a representative volume element containing a hard inclusion shows that the equations provide an accurate representation of the local stress state. The equations are implemented into a multi-barrier model and compared with CTOD experiments with two different levels of constraint.
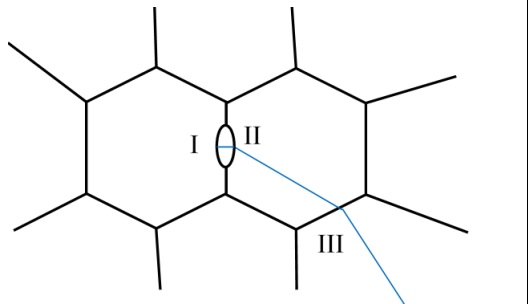
3.1 Introduction

Mechanical integrity assessment of steel structures frequently requires knowledge of their resistance to catastrophic failure by fast, unstable crack growth, expressed as fracture toughness. Ferritic steels exhibit a transition from ductile fracture modes at higher temperatures to brittle fracture at lower temperatures. Toughness at lower temperatures and the transition temperature region are related to transgranular quasi-cleavage fracture, which will be called cleavage in this paper. Many material

requirements, for example Charpy test results, are related to the prevention of cleavage. The need for more accurate cleavage modelling is particularly acute for a new generation of high- and very high-strength steels (yield strength of 500 to 1000 MPa) because they generally have lower toughness, and therefore, a lower safety margin. Furthermore, these classes of steels obtain their favorable properties through their complex, multi-phase microstructures, which complicates microstructural modelling of cleavage-driven failure.

As a highly localized phenomenon, cleavage fracture exhibits strong sensitivity to material characteristics at the microstructural level, dependent on material and structure fabrication, and it is coupled with a constraint effect originating from the macroscopic stress state. It is generally accepted that the micromechanism of cleavage fracture can be described by three critical events: particle fracture, propagation of a particle-size crack and the propagation of a grain-size crack ([1-6]). A summary of the models describing micromechanisms of cleavage fracture can be found in [7]. Table 3.1 shows a schematic representation of these three critical events and the corresponding parameters to define cleavage criteria. As the first in the chain of events that leads to cleavage, fracture of the hard particle requires special attention.

Table 3.1. Micromechanisms of cleavage fracture (adopted from [20])

The blue line refers to a crack; the ellipse refers to a hard particle; the hexagons refer to grains.

Event	Criteria
I Crack initiation in a particle	$\sigma_H > \sigma_H^c$
II Crack propagation across particle/grain interface	$\sigma_{n,II} > \sigma_{n,II}^c = \dfrac{K_{Ia}^{hm}}{\sqrt{d}}$
III Crack propagation across grain boundary	$\sigma_{n,III} > \sigma_{n,III}^c = \dfrac{K_{Ia}^{mm}}{\sqrt{D_g}}$

σ_H is the first principal stress on the hard particle; σ_n is the maximum normal stress on the cleavage planes of the grain.
K_{Ia}^{hm} and K_{Ia}^{mm} are local crack arrest parameters on the particle/grain interface and the grain boundary, respectively.
d, D_g represent the size of crack, which is assumed to be correlated to the hard particle size, and the grain size, respectively.
Superscript c represents a critical value.
Subscripts II and III refer to the event number.

Second-phase particles are particles which do not belong to the matrix phases. They are present because of the alloying elements that are added for hardenability, yield strength, and other properties. Carbides, brittle inclusions, and M-A constituent are examples of second phase particles that are widely reported as being detrimental for cleavage fracture in steels ([8-11]). Although steels also have soft inclusions like MnS, they mostly affect the ductile failure mode and are not the focus in this paper. It

has been observed that larger inclusions and inclusion clusters act as weakest features in the microstructure, allowing brittle crack initiation and propagation ([12-15]). The probability that cracks initiate in a given particle depends on the particle size, shape, volume fraction and orientation of the elongated particles with respect to the applied stress ([15-19]). Therefore, it is important to be able to estimate the local stresses on hard inclusions based on the global loading in order to be able to capture the first stage of cleavage fracture, especially in high-strength steels.

Studies on the stress distributions within or around inclusions have been performed extensively ([21-27]). These works contributed to a good understanding of the stress distribution within or around a hard inclusion embedded in an elastic-plastic matrix. It is found that there is a critical aspect ratio at which interface debonding changes to particle fracture, and the remote stress triaxiality has a significant effect on this transition [25].

However, methods that can directly determine the local stress on a hard inclusion from the remote stress still need development. For linear elastic problems, the Eshelby solution [28] is available for the calculation of the stress on a spheroidal inclusion. For nonlinear problems, the classic Eshelby solution has been modified to incremental approaches with the mean-field (MF) homogenization method making use of equivalent tangent operators (e.g. [29], [30]). Corresponding validations [31] showed that the MF method can give accurate predictions of the effective properties of a composite at continuum level, but this does not guarantee the same accuracy at the microstructural phase level. The accuracy of the MF method at the phase level (especially for the inclusions), or other methods using Eshelby tensors, relies on the assumptions of a homogeneous stress inside the inclusion and a homogeneous equivalent tangent operator of the matrix. Violation of the basic assumptions leads to inaccuracy or even failure of the Eshelby tensor based methods. To improve the average stress calculation of individual phases, [32] proposed including fitting parameters for the MF method. Because this modified method remains heuristic and is not predictive *a priori* for other composite materials, [33] presented an extended MF method which is fully coupled with a nonlinear Finite Element Analysis (FEA) of the inclusion problem to avoid the use of Eshelby tensors. Thus, the calculation of the inclusion stress has to be performed with numerical simulations (e.g. FEA).

Determination of the inclusion stress using FEA can be computationally costly because the microstructures (both matrix and inclusions) of metals can vary widely. The material may contain hard inclusions that have various shapes, orientations and material properties. Under different loading patterns, the constraint effect may also vary locally and lead to various stress states. [20], [34], and [35] developed empirical equations to relate the far-field stress to the local stress on a hard inclusion for a specific material. A more detailed summary of the available empirical equations will be given in the Discussion part of the present paper. An empirical equation that can account for multiple parameters

and can be used for a general case will require extensive simulations and suffer from an ambiguous fitting process. Thus, this paper aims to propose an analytical solution that can be used for the calculation of local stress on a hard inclusion based on the far-field stress on the matrix.

3.2 Development of analytical solution of the local stress on inclusions

For elastic problems, the Eshelby solution ([28]) is available for the calculation of the stress on a spheroidal inclusion. The detailed calculation of the Eshelby solution involves determination of the Eshelby tensor from inclusion geometry and the formulation of equilibrium equations, which can be found in [36]. However, the Eshelby solution is not valid during plastic deformation for the dilute inclusion problem. A simplified analytical equation is established in this paper to quantitatively determine the stress on the inclusion from the far-field stress on the macroscale. The geometric representation of this problem is illustrated in Fig 3. 1 as an elastic hard inclusion embedded in an infinite volume of elastic-plastic matrix. In this paper, the inclusion is assumed to be a spheroid characterized by the principal semi-axes ($R_1{\neq}R_2{=}R_3$). The remote load is modelled as two principal stresses σ_1 and σ_2, which are normal to R_3. The angle between inclusion's principal semi-axis R_1 and the remote first principal stress σ_1 is noted as θ. For the third principal direction, the remote deformation is considered to be zero, which corresponds to a plane strain condition on macroscopic scale for the matrix.

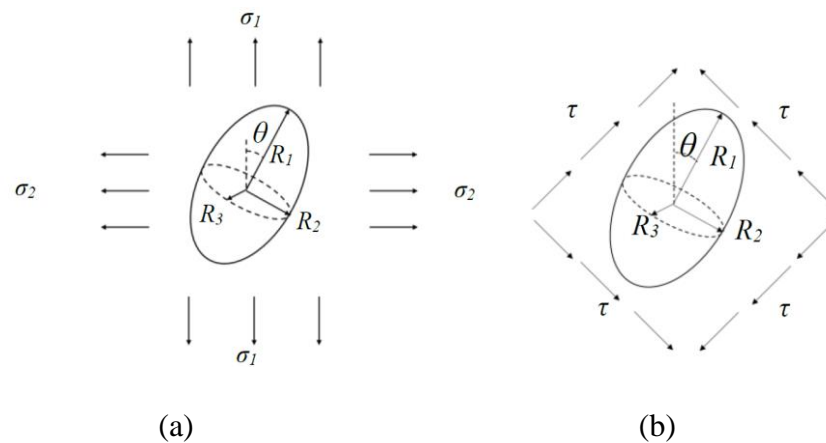(a)   (b)

Fig 3.1 A schematic representation of a microstructural inclusion embedded in an infinite matrix under (a) general remote load (b) remote deviatoric (pure shear) stress

3.2.1 Key assumptions

The following five assumptions are used in the derivation of the analytical solution:

(1) There is perfect cohesion between the inclusion and the matrix.

(2) The matrix has low-hardening behaviour after yielding.

(3) The average first principal stress over the mid-section of the inclusion is the representative stress ($\sigma_{1,inclu}$).

(4) If $\sigma_{1,matrix}$ is the remote first principal stress of the matrix, then the stress difference ($\sigma_{1,inclu} - \sigma_{1,matrix}$) is only related to the deviatoric part of the remote stress field (the maximum shear stress) when remote plastic deformation is pronounced. The derivation of the analytical solution is based on a formulation with remote shear stress, while the hydrostatic pressure of the remote stress field is not considered. This assumption is further validated with FEA in Section 3.

(5) The tensile stress induced by shear deformation vanishes in the matrix close to the inclusion, and the entire reduced stress is taken by the inclusion. This assumption is further illustrated in Section 3.2.2 and validated with FEA in Section 3.3.

Assumption (1) comes from the observation that cleavage fracture is mostly transgranular failure initiated rather by particle cracking than by boundary decohesion. Assumption (2) corresponds to a characteristic of high strength steels. For example, [37] reported on the plasticity properties of hundreds of structural steels. Almost all of the steels with a yield strength greater than 500 MPa had an ultimate strength that is less than 25% greater than the yield strength. Assumption (3) is due to the fact that the maximum tensile stress within the inclusion is largely influenced by the imperfect morphology which cannot to be reflected by analytical derivation, and the average tensile stress over the mid-section can reflect the driving force to break an inclusion. Assumption (4) is based on the argument that the stress difference caused by hydrostatic pressure is due to the compatible deformation under volume change, and when the matrix remains elastic, extra uniform strain is generated inside the inclusion to satisfy the compatibility of deformation. However, when the matrix enters the plastic stage, large deviatoric deformation can be generated in the matrix near the inclusion allowing the condition of compatible deformation to be satisfied. The extra strain inside the inclusion will no longer remain uniform, and the influence of hydrostatic pressure is negligible. Assumption (5) is due to the effect that the inclusion gives extra constraint to the nearby matrix and the matrix cannot deform freely along the slip plane. As a consequence, larger shear stress is generated along the inclusion/matrix interface rather than along the remote shear direction. The tensile stress associated with the shear deformation is also redistributed from the matrix to the inclusion.

3.2.2 Two-dimensional analysis

The analytical expression of the inclusion problem is first formulated in 2D based on a plane-strain condition by Fig 3. 2. When only considering the remote deviatoric stress, the general case will reduce to Fig 3. 1 (b), where $\tau = \sigma_1 = -\sigma_2$. In Fig 3. 2, the principal stress coordinate system is used, where the y axis is parallel to the remote maximum principal stress and the x axis is parallel to the remote

minimum principal stress. The inclusion outline is visualized by the solid lines in Fig 3. 2 and is defined as an ellipse by:

$$\left(\frac{\cos(\theta)x - \sin(\theta)y}{1}\right)^2 + \left(\frac{\cos(\theta)y + \sin(\theta)x}{R_1/R_2}\right)^2 = 1. \qquad \text{3-2-1}$$
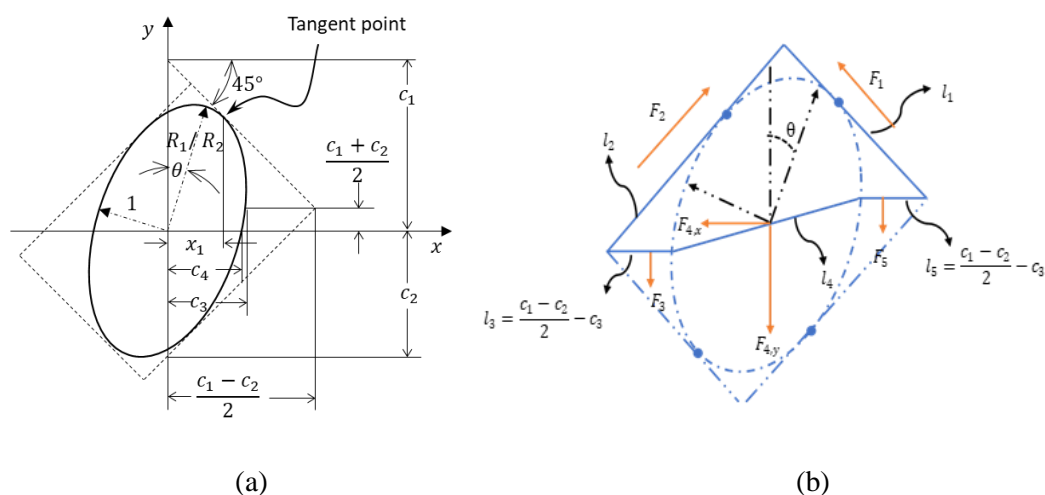

(a)   (b)

Fig 3. 2 (a) Parameters for the analytical expression of an inclusion in a 2D coordinate (b) Free body diagram of half the inclusion and the matrix in its vicinity

In eq. 3-2-1, x and y are lengths normalized by the minor axis of the ellipse and are dimensionless. There are four planes parallel to the remote principal shear directions, which are visualized by the dashed lines in Fig 3. 2 (a), forming a rectangle around the inclusion. According to slip-line theory, only the matrix between the inclusion and the rectangle is assumed to be influenced by the presence of the inclusion, and the shear field outside the rectangle will be uniform. The parameters c_1, c_2, c_3, and c_4 shown in Fig 3. 2 can be found from geometry.

Fig 3. 2 (b) shows the free body diagram of half the inclusion and the matrix in its vicinity. The outline of the isolated body is visualized by the solid lines. There are five straight boundaries of this free body noted as l_1 to l_5. The forces acting on these boundaries are noted as F_1 to F_5 respectively. When the inclusion has the same material properties as the matrix, the isolated body behaves like a homogeneous matrix material. Boundaries l_1 and l_2 are parallel to the remote principal shear directions and thus F_1 and F_2 are pure shear forces. Boundaries l_3 and l_5 are normal to the remote first principal stress and thus F_3 and F_5 are parallel to the y axis.

The force equilibrium in the y direction is:

$$F_1\cos 45° + F_2\cos 45° = F_3 + F_{4,y} + F_5, \qquad \text{3-2-2}$$

where $F_1 = \tau l_1$, $F_2 = \tau l_2$ and $F_3 = F_5 = \tau l_3$.

When the inclusion is of a much stronger material than the matrix (e.g., the inclusion remains in elastic stage when the matrix is yielding), there is an extra constraint for plastic deformation of the matrix in the vicinity. The shear stress along the inclusion/matrix interface is generally increased. In order to maintain force equilibrium, the normal stress at the horizontal boundaries l_3 and l_5 is reduced. Consequently, the matrix in the vicinity of the inclusion has a much smaller stress in the principal direction, and the reduced stress is taken by the inclusion. The force $F_{4,y}$ is further decomposed into the force that it would otherwise have in a homogenous system, $F_{4h,y}$ and the added force that it has because it takes stresses from the unstressed surroundings, $F_{4\Delta,y}$.

$$F_{4,y} = F_{4h,y} + F_{4\Delta,y} \qquad \text{3-2-3}$$

The forces F_3 and F_5 are assumed to become zero and will lead to the following force equilibrium in the y direction:

$$F_1 \cos 45° + F_2 \cos 45° = F_{4h,y} + F_{4\Delta,y} \; . \qquad \text{3-2-4}$$

The extra force taken in the y-direction by the inclusion can be calculated as $F_{4\Delta,y} = 2\tau \left(\frac{c_1 - c_2}{2} - c_3 \right)$. If this force is averaged at the inclusion mid-section normal to the y direction, the averaged extra stress is:

$$\sigma_{1,inclu} - \sigma_{1,matrix} = \frac{\Delta F_{4,y}}{2c_4} = \tau \frac{(c_1 - c_2)/2 - c_3}{c_4} = \frac{\sigma_{eq,matrix}}{\sqrt{3}} \frac{(c_1 - c_2)/2 - c_3}{c_4} \; . \qquad \text{3-2-5}$$

3.2.3 Formulation

As result of the 2D analysis, the representative stress of the inclusion ($\sigma_{1,inclu}$) can be calculated with:

$$\sigma_{1,inclu} = \sigma_{1,matrix} + f\left(\frac{R_1}{R_2}, \theta \right) \sigma_{eq,matrix}, \qquad \text{3-2-6}$$

where $\sigma_{1,matrix}$ is the first principal stress on the far field, and $\sigma_{eq,matrix}$ is the remote Von-Mises stress of the matrix; $f\left(\frac{R_1}{R_2}, \theta \right)$ is given as:

$$f\left(\frac{R_1}{R_2}, \frac{R_3}{R_2}, \theta \right) = \left(\frac{(c_1 - c_2)/2 - c_3}{c_4} \right)/\sqrt{3}, \qquad \text{3-2-7}$$

where c_1, c_2, c_3 and c_4 can be determined with eqs. 3-2-8 to 3-2-16.

$$c_1 = x_1 + \frac{px_1 + \sqrt{qx_1^2 + 4h}}{2h} \qquad \text{3-2-8}$$

$$c_2 = -x_2 + \frac{px_2 - \sqrt{qx_2^2 + 4h}}{2h} \qquad \text{3-2-9}$$

$$c_3 = \frac{ph(c_1+c_1)+\sqrt{qh^2(c_1+c_2)^2+4(p^2-q)h}}{p^2-q} \qquad \text{3-2-10}$$

$$c_4 = \sqrt{1/\left[\left(\frac{\cos\theta}{1}\right)^2+\left(\frac{\sin\theta}{R_1/R_2}\right)^2\right]} \qquad \text{3-2-11}$$

$$x_1 = \sqrt{\frac{16h^3+4hp^2+16ph^2}{q^2-(4h^2+p^2+4ph)q}} \qquad \text{3-2-12}$$

$$x_2 = \sqrt{\frac{16h^3+4hp^2-16ph^2}{q^2-(4h^2+p^2-4ph)q}} \qquad \text{3-2-13}$$

$$h = \sin^2\theta + \frac{\cos^2\theta}{(R_1/R_2)^2} \qquad \text{3-2-14}$$

$$p = 2\cos\theta\sin\theta\left(1-\frac{1}{(R_1/R_2)^2}\right) \qquad \text{3-2-15}$$

$$q = 4\cos^2\theta\sin^2\theta\left(\frac{1}{(R_1/R_2)^2}-1\right)^2 - 4\left(\sin^2\theta+\frac{\cos^2\theta}{(R_1/R_2)^2}\right)\left(\cos^2\theta+\frac{\sin^2\theta}{(R_1/R_2)^2}\right) \qquad \text{3-2-16}$$

The above equations are based on a 2D formulation, assuming the 3-D spheroidal inclusion to have a symmetric geometry. In that case, the result remains even if the local shear direction deviates from remote shear direction. When the symmetric axis of the inclusion lies parallel to the remote first principal stress, the above assumption is satisfied, and the derivation does not require correction. When the symmetric axis of the inclusion has an angle to the remote first principal stress, the 2D geometric characterization of the inclusion may differ along the third direction (when the 2D derivation is at the xy plane, the third direction perpendicular to the xy plane is denoted by z axis), and a correction term should be applied. The correction term is heuristically assumed to be proportional to the geometry asymmetry with shear stress as a weight factor:

$$\frac{(\sigma_{1,inclu}-\sigma_{1,matrix})_{corrected}}{(\sigma_{1,inclu}-\sigma_{1,matrix})_{xy}} = \left(1-\frac{\tau_{yz,max}}{\tau_{xy,max}}\right)+\frac{\tau_{yz,max}}{\tau_{xy,max}}\times\frac{\left(\frac{(c_1-c_2)/2-c_3}{c_4}\right)_{yz}}{\left(\frac{(c_1-c_2)/2-c_3}{c_4}\right)_{xy}}, \qquad \text{3-2-17(a)}$$

where $\tau_{yz,max}$ and $\tau_{xy,max}$ are the maximum shear stresses in yz plane and in xy plane respectively, $\left(\frac{(c_1-c_2)/2-c_3}{c_4}\right)_{yz}$ and $\left(\frac{(c_1-c_2)/2-c_3}{c_4}\right)_{xy}$ are geometry calculations based on yz plane and xy plane respectively. For plane strain condition, the correction term is approximated as a function of c_4:

$$\frac{(\sigma_{1,inclu}-\sigma_{1,matrix})_{corrected}}{(\sigma_{1,inclu}-\sigma_{1,matrix})_{xy}} = 0.3 + 0.7\times c_4, \qquad \text{3-2-17(b)}$$

If the matrix is in the elastic stage, the inclusion stress can be calculated by analytical equations following Eshelby's solution. The effects of remote stress triaxiality and inclusion modulus can be included. If the matrix has developed significant plasticity, the inclusion stress is only related to the

shear components in the remote loading condition as stated in assumption (4). In such a situation, the effects of remote stress triaxiality and inclusion modulus can be neglected, and the inclusion stress is calculated by the present analytical equations involving the inclusion geometry, orientation and the remote matrix stress. When the matrix starts to yield but has not reached a threshold plastic strain ($\varepsilon_{p,th}$), the inclusion stress is calculated by a linear interpolation with respect to plastic strain from the stress calculated by Eshelby's solution in the elastic range to the stress calculated by eqs. 3-2-6 to 3-2-17 when the plastic strain is equal to $\varepsilon_{p,th}$. The exact value of $\varepsilon_{p,th}$ to define the transition can be regarded as the plastic strain at which the strain hardening rate $d\sigma/d\varepsilon_p$ of the steel is less than 0.5% of the Young's modulus.

3.3 Validation with numerical simulations

In order to validate the analytical solution (eqs. 3-2-6 to 3-2-17) that predicts the representative stress on a hard inclusion, numerical simulations with nonlinear FEA are performed. The FEA model is first described. After that, the assumption of the shear regions formed around the inclusion is validated. The effect of the remote stress triaxiality, the remote plastic strain, and the Young's modulus of the inclusion are evaluated. Comparison between analytical solution and numerical simulations is presented on the geometry of the inclusion with first the aspect ratio (ratio of major to minor axis) and thereafter the orientation. Finally, the effect of the stress-strain curve of the matrix is considered.

3.3.1 Description of FEA model

The FEA solutions are performed with Abaqus 2017 for an elastic hard inclusion embedded in an elastic-plastic matrix. The stress-strain relationship of the steel is characterized by Ludwik's law [38], which is defined with the flow stress (σ) and the effective plastic strain (ε_p) as:

$$\sigma = \sigma_y + K\varepsilon_p^{n_L}. \tag{3-3-1}$$

where K and n_L are material parameters. For the reference study, σ_y is 690 MPa, K is 234 MPa, and n_L is 0.17, which are determined from a tensile test of S690 QL steel at room temperature. The inclusion is a linearly elastic material with a Young's modulus of 300 GPa and a Poisson's ratio of 0.3. According to several authors (e.g. [39], [40], [41]), typical hard inclusion moduli vary from 250 GPa to 380 GPa. A sensitivity study is performed for various aspect ratios of the spheroidal inclusion (R_1/R_2), stress triaxiality of the remote load (η), angle between inclusion's major axis and remote principal stress (θ), and material properties of the inclusion and the matrix.
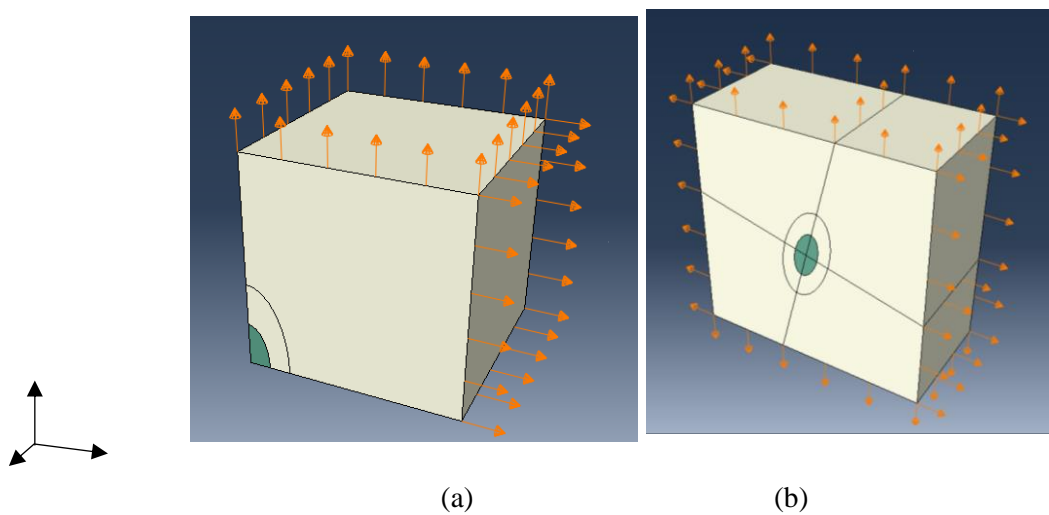
(a)   (b)

Fig 3. 3 3D model of an inclusion (in colour green) embedded in a cubic volume matrix (a) $\theta = 0\degree$ one eighth of the cube (b) $\theta > 0\degree$ half the cube

For the case where $\theta = 0\degree$, one eighth of the entire 40 μm × 40 μm × 40 μm cubic volume is modelled with the use of symmetry as shown in Fig 3. 3 (a). The longer axis of the inclusion is 4 μm, resulting in a volume fraction of inclusions of approximately 0.04% and a length fraction of 10%. The boundary conditions of the inclusion problem are referred as the far-field state, which represents the plastic strain and stress triaxiality on a macroscopic level. The boundary conditions of the cubic volume correspond to a plane-strain condition on the macroscopic scale. Normal traction is applied uniformly in two principal directions (axis 1 and 2), and normal displacement is constrained to zero in the third principal direction (axis 3). Displacement control is used to apply deformation at the boundary surfaces to generate a final plastic strain of approximately 0.05. The displacement along axis 1 (u_1) is the major tensile traction and the displacement along axis 2 (u_2) is set as a ratio to u_1 to generate a constant stress triaxiality. The C3D20R (20-node hexahedron with reduced integration) element is used to mesh both the inclusion and the matrix. The average element of the inclusion has a length of 0.01 μm. The average element of the matrix has a length of 1 μm. The matrix in the vicinity of the inclusion has a linearly biased mesh to transition to a larger element size. For the case where $\theta > 0\degree$ (Fig 3. 3 (b)), half of the entire cubic volume is modelled with the use of symmetry. The size of the inclusion, cubic volume, element density and the loading conditions are the same as for $\theta = 0\degree$.

The full Newton-Raphson algorithm is used to solve the geometric and material nonlinearity. The representative inclusion stress is defined as the average tensile stress acting on the mid-section of the inclusion. The mid-section lays normal to the tensile loading direction (axis 1 in Fig 3.3), through the centroid, and separates the inclusion into two anti-symmetrical parts. The average stress is computed as the normal component of the total force acting on the mid-section divided by the area of the mid-section. The total force accounts for both tensile and compressive components, while since the remote load long

axis 1 is in tension the average stress on mid-section would also be in tension. A convergence study on element size has been conducted. Re-running the same model with twice the inclusion size was checked, yielding the same results. The check of element size and inclusion size is not included in the manuscript for brevity.
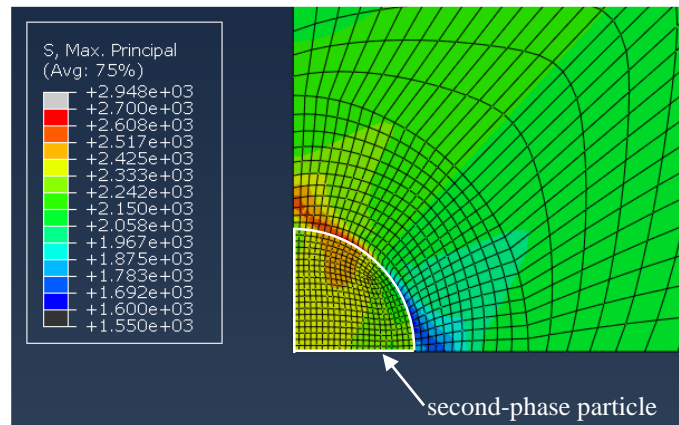
3.3.2 Validation of shear plane hypothesis

Fig 3. 4 Distribution of first principal stress around the inclusion (stress is given in MPa)

Fig 3. 4 shows the distribution of first principal stress near the inclusion for the case of a spherical inclusion ($R_1=R_2$), under $\eta=2$. It confirms the assumption that a shear plane is formed at the inclusion/matrix interface, following the principal shear direction. Between the shear plane and the inclusion, the matrix undergoes significant stress variation. The principal stress directions in the vicinity of the inclusion have been distorted due to the constraint of the inclusion. Consequently, the first principal stress inside the inclusion is higher than the remote first principal stress.

3.3.3 Validation of assumption on plastic strain and stress triaxiality

The stress is computed using the solution for shear only. The remote pressure does not play a role when matrix deformed plastically. Fig 3. 5 shows the inclusion stress under various stress triaxiality values, which supports the assumption. Although the stress depends on the stress triaxiality in the elastic and the early yielding stage, the dependence vanishes when a certain level of plastic deformation has been developed in the matrix. It is observed that the influence of the hydrostatic pressure on the stress difference between inclusion and matrix is decreasing if the remote plastic strain is greater than 0.01 and fully vanishes if remote plastic strain is greater than 0.03. It should be mentioned that it is straightforward to notice this phenomenon when the stress is plotted with the absolute difference between inclusion stress and matrix stress, as in Fig 3. 5 (a). If the stress is plotted as a normalized value (as in Fig 3. 5 (b)), it can be compared with the results in the literature ([23], [24], [42]) but does not show the above conclusion.
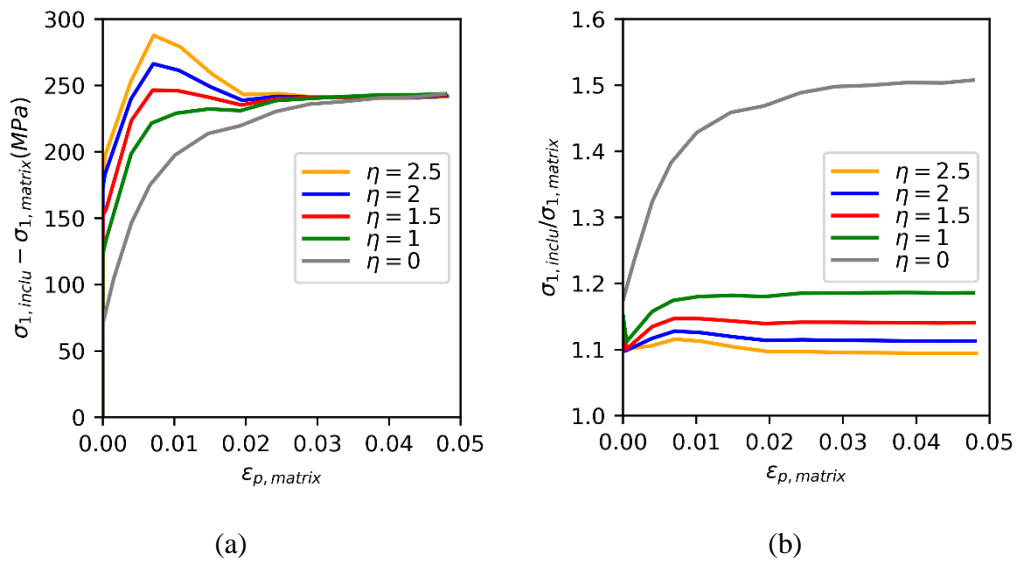
(a)   (b)

Fig 3. 5 Stress of the inclusion vs remote plastic strain under various stress triaxialities (η)

(a) plotted as absolute difference (b) plotted as normalized value

3.3.4 Effect of inclusion elastic modulus

A similar effect is observed in the sensitivity study of the inclusion modulus. Fig 3. 6 shows that the influence of the inclusion modulus is decreasing with increasing remote plastic strain and fully vanishes for remote plastic strain greater than 0.02. If the matrix has developed significant plasticity, the effects of inclusion modulus can be neglected, as stated in the development of the analytical solution.
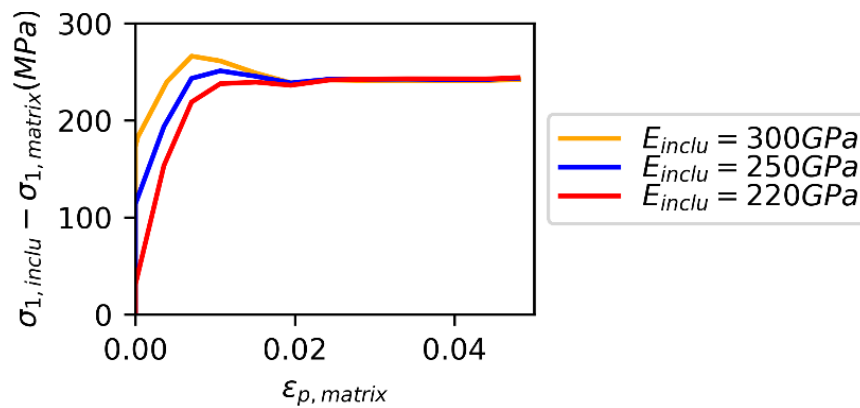

Fig 3. 6 Stress difference vs plastic strain for various inclusion moduli ($R_1/R_2=1$)

3.3.5 Effect of inclusion shape

To assess the influence of the shape of the inclusion, the aspect ratio was first varied parametrically while the stress triaxiality was held constant at $\eta=2$. Based on the matrix elasto-plastic properties, $\varepsilon_{p,th}$ in the analytical solution is determined as 0.02. Fig 3. 7 shows the results of this study. It is observed

that the inclusion stress is higher for larger values of R_1/R_2. This effect occurs for all levels of remote plastic strain.
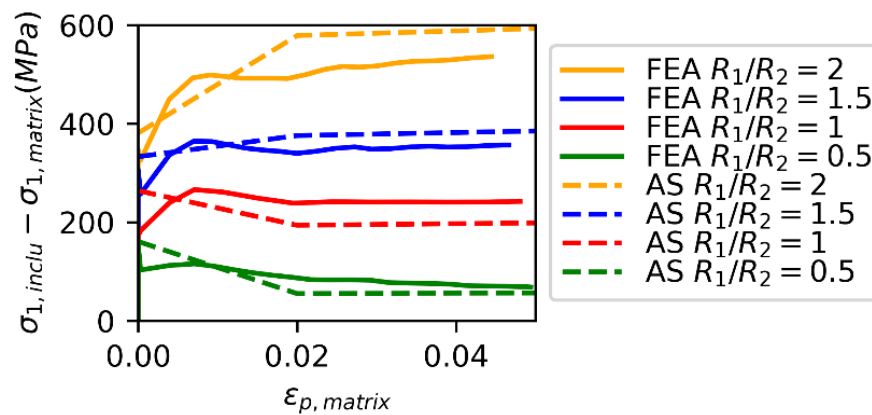

Fig 3. 7 Stress difference vs plastic strain for various aspect ratios (θ=0°)

Next, the effect of orientation was assessed. Fig 3. 8 shows an inclusion of R_1/R_2=2 under the same remote loading condition, but the major axis (R_1) has an angle (θ) with the direction of the remote first principal stress. It is observed that as θ increases, the stress at an elongated inclusion is reduced. This effect exists for all levels of remote plastic strain. By comparing the curve θ=90° in Fig 3. 8 with the curve R_1/R_2=0.5 in Fig 3. 7, it can be noticed that the stress is less pronounced for the inclusion of R_1=0.5R_2=0.5R_3. This indicates that the effect of inclusion geometry is related to its three-dimensional morphology, even if the remote loading condition is plane strain.
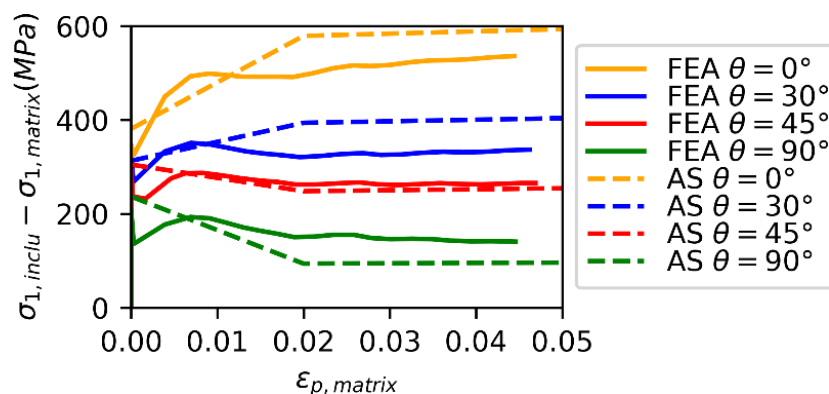

Fig 3. 8 Stress difference vs plastic strain for various inclusion orientations (R_1/R_2=2)

3.3.6 Effect of the shape of the stress-strain curve

The analytical solution has been compared with FEA models of various matrix properties other than the reference study. The yield strength and Ludwik's parameters K and n_L, given in eq. 3-3-1, have been varied to determine the influence. Fig 3. 9 (a) shows the stress-strain curves of steels A-D. Fig 3. 9 (b) shows the parameters to define steels A-D. Steels A-D are all high strength steels with $\sigma_y \geq$ 690 MPa and relatively low-hardening behaviour. The varied parameter values are hypothetical, while

the resulting curves can be compared with stress-strain curves for commonly used high strength steels, for example as reported by [43]. The analysis is performed with an arbitrary case $R_1/R_2=2$ and $\theta= 45°$. According to Fig 3. 9(c), the analytical solution shows good performance independently of yield strength and n_L values. However, for a higher K value (pronounced hardening in the early yielding stage), the analytical solution is seen to give a less accurate prediction of the stress. This phenomenon can be explained by its violation of the assumption of the low-hardening condition. Thus, the analytical solution should be used carefully on materials that have pronounced hardening behavior. In addition, there is difference in the shape of the curves between the FEA and the analytical solution prior to $\varepsilon_{p,th}$, e.g., the FEA result increases and then decreases, whereas the analytical solution only decreases until to $\varepsilon_{p,th}$. This difference is due to the linear interpolation of Eshelby's solution in the elastic range and the proposed analytical solution at $\varepsilon_{p,th}$. Since hardening is not included in the linear interpolation, this difference is more pronounced for material with higher K and higher n_L values.

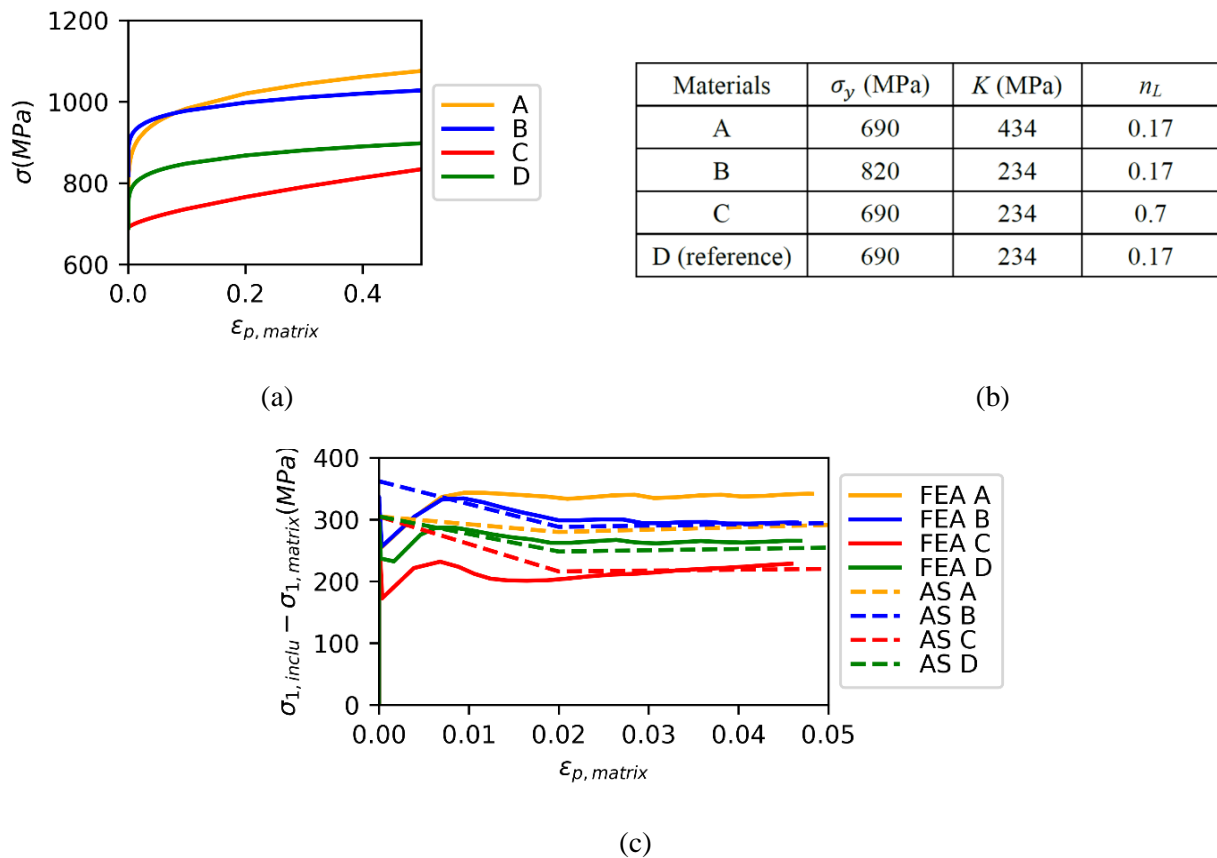| Materials	σ_y (MPa)	K (MPa)	n_L
A	690	434	0.17
B	820	234	0.17
C	690	234	0.7
D (reference)	690	234	0.17

(a)

(b)

(c)

Fig 3. 9 (a) Hardening behaviour for various matrix materials (b) Material parameters of steels A-D (c) Stress difference vs plastic strain for steels A-D

3.3.7 Summary of validation studies

The analytical model has been systematically compared with FEA to assess the underlying assumptions and accuracy over a range of parameters. It was first demonstrated that shear regions

around the inclusion do form as a tangent to the hard inclusion, with a 45° angle relative to the first principal stress. It was shown in Fig 3. 5-6 that the fully plastic solution is independent of stress triaxiality and the Young's modulus of the inclusion. It was shown in Fig 3. 7-9 that the analytical model was able to accommodate the shape (aspect ratio and orientation) of the inclusion and various stress-strain curves. Materials that show a high level of hardening show less correlation with the analytical solution. This is to be expected based on the assumptions used in developing the solution and based on the observations that high-strength steels (the focus of this study) tend to have low hardening rate.

The analytical model is able to capture important input parameters within approximately 25% when full plasticity is developed. The Eshelby solution remains a good method of assessing linear-elastic conclusions. We present and validate a solution for fully plastic behavior. We have shown that linear interpolation between the elastic condition and the fully plastic behavior can provide an acceptable accuracy. In the validations, $\varepsilon_{p,th}$ is set as 0.02, where the strain hardening rate $d\sigma/d\varepsilon_p$ of the steel is less than 0.5% of the Young's modulus. The linear interpolation and criterion to define $\varepsilon_{p,th}$ is demonstrated and validated in Fig 3. 7, 8, and 9. The method is developed and validated for plane strain conditions, but the assumptions and deviations are maintained for plane stress conditions.

3.4 Application to cleavage fracture modelling

The developed solution has been applied on fracture test data to demonstrate the relevance for cleavage fracture modelling. The data sets include specimens taken from the top quarter section and middle section of the S690 QL steel plate. All specimens are fractured at -100℃ and have a brittle fracture mode.

3.4.1 Description of the materials and mechanical tests

A commercially available 80 mm thick quenched and tempered S690 high strength steel plate is used in this paper for illustration and validation. Materials are extracted from the top quarter section and the middle section of plate. The materials have been previously characterized in [15]. The chemical composition of the steel plate is shown in Table 3.2.

Table 3.2. Chemical composition of S690QL

wt (%)	Fe	C	Si	Al	Mo	Other
Top	Bal.	0.17 ± 0.001	0.29 ± 0.022	0.07 ± 0.005	0.30 ± 0.007	Mn, Ni, Cr, Nb

The microstructure of the plate varies through the thickness from a fully tempered martensitic structure in the regions close to the surfaces to a mixed tempered martensitic-bainitic structure in the central section of the plate. Spherical inclusions and second-phase particles ranging from 1 to 5 µm

were observed through the full thickness, including oxides and nitrides of rather complex chemical composition such as (Mg,Ti)(O,N), (Mg,Al,Ca)(O,N) and (Mg,Al,Ca,Ti)(O,N). In the middle position, in addition to the spherical inclusions, cubic and elongated inclusions with dimensions ranging from 1 to 11 µm were observed. Niobium-rich carbides and nitrides such as (Ti,Nb)(N), (Ti,Nb)(C), Nb(C), and (Nb,Ti)(C,N) are present in the middle position. Fig 3. 10 shows representative morphology of the inclusions observed in the S690QL steel plate at top quarter section and middle section.
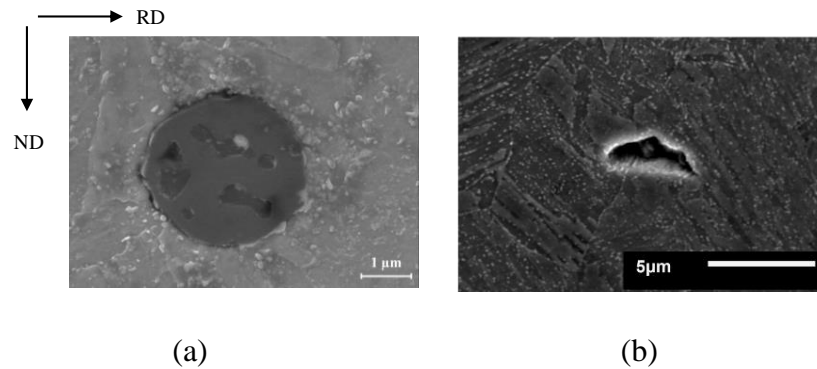

(a)   (b)

Fig 3. 10 SEM micrograph of inclusions in the S690QL steel plate (RD is the rolling direction and ND is the normal direction) (a) a (Mg,Al,Ca)(O,N) inclusion (b) a Nb enriched inclusion

Prior austenite grains (PAG) at three locations in each section were reconstructed based on EBSD data and ARPGE software. Fig 3. 11 shows the statistical distribution of grain size in each section, with the Least Square fitting. It is apparent that the middle section specimens have larger average grain size and a greater portion of extremely large grains (major axis larger than 50 µm).
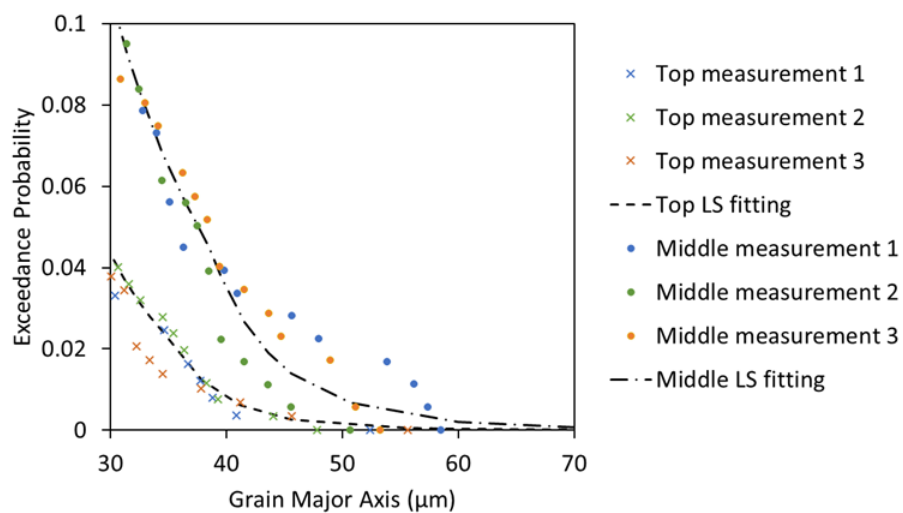

Fig 3. 11. Statistical distribution of grain size at top quarter and middle section

The parameters of Ludwik's law are determined for top quarter and middle section by tensile tests at -100 °C. The values of the parameters are summarized in Table 3.3.

Table 3.3 Material parameters of S690 QT steel determined by tensile test at -100 °C

Parameters	Top section	Middle section
Young's modulus (GPa)	219	236
Yield stress (MPa)	961	888
Hardening parameter: K (MPa)	521	593
Hardening exponent: n_L	0.42	0.66

Fracture toughness tests were performed according to ISO 12135 [44] at -100 °C using sub-sized Single Edge Notched Bending (SENB) specimens, with three geometries (a_0/W equal to 0.5, 0.25 and 0.1). For top quarter section specimens, geometries of a_0/W =0.5 and a_0/W =0.25 are considered as high and low constraint conditions, respectively. For middle section specimen, geometries of a_0/W =0.5 and a_0/W =0.1 are considered as high and low constraint conditions, respectively. The geometry of the SENB specimens is specified in Fig 3.12 and Table 3.4. Fractographic examinations reveal that the microstructural hard inclusions play an important role in the cleavage fracture process [15].
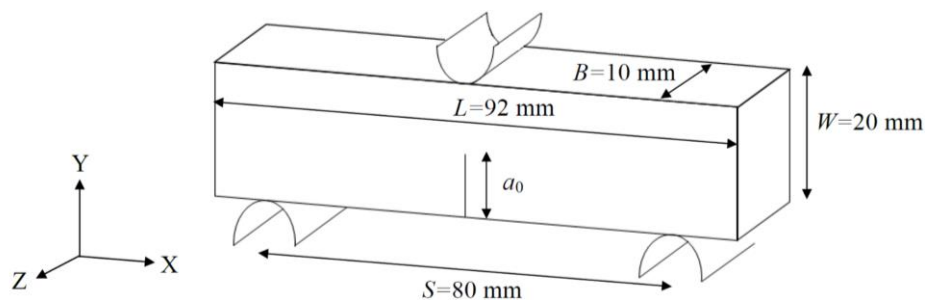

Fig 3. 12 Geometry information of the SENB specimen (Z direction coincides to ND of the plate)

Table 3.4 Geometric information of the initial crack length

Constraint ID	Position in material	Number of samples per material	Crack length, a_0 (notch length + prefatigued crack length) [mm]
1	Top quarter section Middle section	14	10 mm (8.6 mm + 1.4 mm)
2	Top quarter section	18	5 mm (3.6 mm + 1.4 mm)
3	Middle section	13	2 mm (0.6 mm + 1.4 mm)

3.4.2 Statistical modelling of cleavage fracture

In this paper, the modelling of cleavage fracture considers crack nucleation in hard particles and crack propagation through grain boundaries. Observation of the fracture surface reveals that the tested specimens are fractured by crack initiated from oxides and Nb inclusions. The inclusions are relatively large compared to commonly observed hard particles, like carbides, and the cracks initiated by the large inclusions can easily propagate through the inclusion/grain interface. Thus, the dominant barrier of

crack propagation is assumed to be the grain boundary instead of the inclusion/grain interface. The modelling approach is adapted from a double-barrier model proposed by [20], assuming the initiated microcrack to be always large enough to propagate through the inclusion/grain interface.

In the model, FEA of a macroscopic specimen gives the result of stress/strain distribution under a certain global load level (represented as a CTOD). The process zone (PZ) is taken to be the plastic zone. Cleavage probability of each element within the process zone is calculated based on its stress and strain condition. By accounting for the cleavage probability of all elements over the process zone, the total failure probability of the specimen can be calculated.

Prior to the cleavage modelling, the stress concentration factor of inclusion, f_α, is calculated using the developed analytical solution based on the material properties and inclusion geometry. The cleavage probability of a single potential cracking nucleus in element j under load level i, $P_{f,ij}$, is calculated based on the following steps:

(1) Calculate the inclusion stress $\sigma_{1,inclu}$ from eq. 3-2-6 and check if the inclusion stress exceeds the critical value σ_H^C. A micro-crack is initiated in the inclusions if $\sigma_{1,inclu} > \sigma_H^C$, and $P_{f,ij}$ would be calculated by steps (2) – (3). Otherwise, it is assumed that no micro-crack is initiated and $P_{f,ij} = 0$.

(2) If the inclusion stress exceeds the critical value to nucleate a crack, a minimum grain size D_c is calculated by Griffith-like criteria as for the first principal stress within the grain ($\sigma_{1,matrix}$) to propagate the crack across the grain boundary, by

$$D_c = (K_{Ia}^{mm}/\sigma_{1,matrix})^2. \qquad 3\text{-}4\text{-}1$$

where K_{Ia}^{mm} is the crack arrest parameter of grain boundary.

(3) A cleavage probability $P_{f,ij}$ is calculated for the possibility that a grain has the major axis greater than D_c. $P_{f,ij}$ can be calculated by

$$P_{f,ij} = \int_{D_c}^{+\infty} f_g(D)\, dD = \frac{\alpha}{D_c^\beta} \qquad 3\text{-}4\text{-}2$$

where $f_g(D)$ is the distribution density function of the grain major axis. In this paper, $\int_{D_c}^{+\infty} f_g(D)\, dD$ is measured from microscopy and fitted as a power-law function with parameters α and β.

The total fracture probability $P_{f,i}$ at load step i is then updated based on the weakest-link mechanism. $P_{f,i}$ is calculated from a Weibull-like formulation that accounts for the total cleavage probability of all potential cracking nuclei within the process zone (PZ):

$$P_{f,i} = 1 - \exp(-\int_{PZ} N P_{f,ij}\, dV) \qquad 3\text{-}4\text{-}3$$

where *N* is the average number of potential cracking nuclei (inclusion) per unit volume.

After looping over all elements, the calculation will be performed for the next load step until all the load steps are evaluated. When the computation is finished, the output is the fracture probability of each load step, in terms of CTOD value.

3.4.3 Finite element modelling of the fracture test

SENB specimens with the geometry specified in Table 3.4 are modelled in Abaqus 2017. In total, four analyses are performed to consider the variety of initial crack length and material properties. For each analysis, a quarter of the specimen ($L/2 \times B/2 \times W$) is modelled as a 3D deformable solid by using symmetry. The support and load roller are modelled as analytical rigid surfaces. The contact surface between rollers and the specimen is frictionless. Fig 3. 13 (a) shows the 3D model of a quarter of the specimen and two rollers. Fig 3. 13 (b) shows the mesh near the crack tip. The initial prefatigued crack tip is modeled as a finite notch that is 0.005 mm in radius. According to [45], this finite notch is small enough to model the near-crack-tip-field for the CTOD value considered in this study. C3D20R element is used for the mesh. The smallest element near the crack tip has a length of 0.001 mm. Displacement control is used to apply a total deflection of 1 mm. A full Newton-Raphson algorithm is used to solve the geometric and material nonlinearity. The material parameters of the top quarter section and the middle section are taken as the values in Table 3.3.
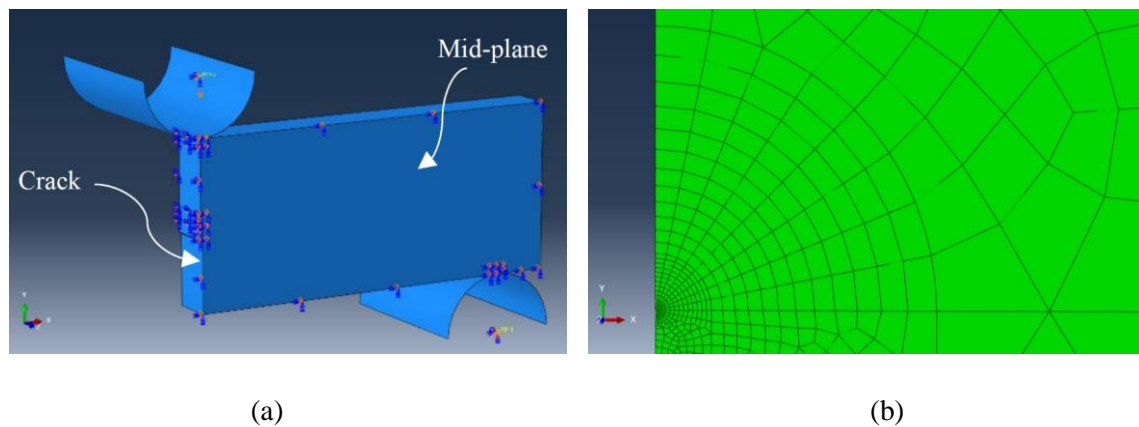

(a)   (b)

Fig 3. 13 (a) 3D model of the three-point-bending test (b) mesh near the crack tip

3.4.4 Cleavage fracture modelling assuming spherical inclusions

The inclusions of both the top quarter section and the middle section are assumed to be spherical for the purposes of calculating f_α. The material parameters of the matrix are taken as in Table 3.3. The remaining input parameters are listed in Table 3.5.

Table 3.5 Value of the input parameters for the cleavage model

Parameters	Values for Top	Values for Middle
Elementary volume V_0 (mm^3)	0.001	0.001
Grain size (major axis) distribution (D in μm)	$P(\text{greater than D})$ $= \dfrac{1.24 \times 10^{11}}{D^{8.24}}$	$P(\text{greater than D})$ $= \dfrac{4.80 \times 10^{9}}{D^{6.95}}$
Number of inclusions per V_0	44	51
Young's modulus of inclusions (GPa)	300	300

3

There are two major differences in the microstructures between the top quarter specimens and the middle section specimens: the grain size distribution and the existence of the elongated inclusions. With the assumption that the grain boundary is the barrier to arrest micro-cracks, the inverse modelling will result in two fitted parameters K_{Ia}^{mm} (crack arrest parameter of grain boundary) and σ_H^C (critical stress of hard inclusion). Determination of these two parameters uses two constraint conditions. The fitted parameter values are listed in Table 3.6.

Table 3.6 Parameter values from inverse modelling

Parameters	Values for Top	Values for Middle
Crack arrest parameter of grain boundary (MPa$\sqrt{\text{m}}$)	25.0	23.2
Critical stress for hard inclusion (MPa)	2000	1200

The fitting on the top quarter specimens and middle quarter specimens results in similar values of K_{Ia}^{mm} but significantly different values of σ_H^C, which corresponds to the microstructural observation that there are similar grain boundaries but distinct inclusions through the thickness. The inclusions in the middle section are computed to have lower strength, which means they are more prone to fracture. Fig 3. 14 shows the resulting P_f-CTOD curves from the modelling in comparison with experimental data. The failure probability, P_f, of a specimen fractured in experiment, was calculated as a rank probability:

$$P_f = \frac{i - 0.3}{N + 0.4} \qquad\qquad 3\text{-}4\text{-}4$$

where i is the rank number in terms of CTOD and N is the total number of experiments.
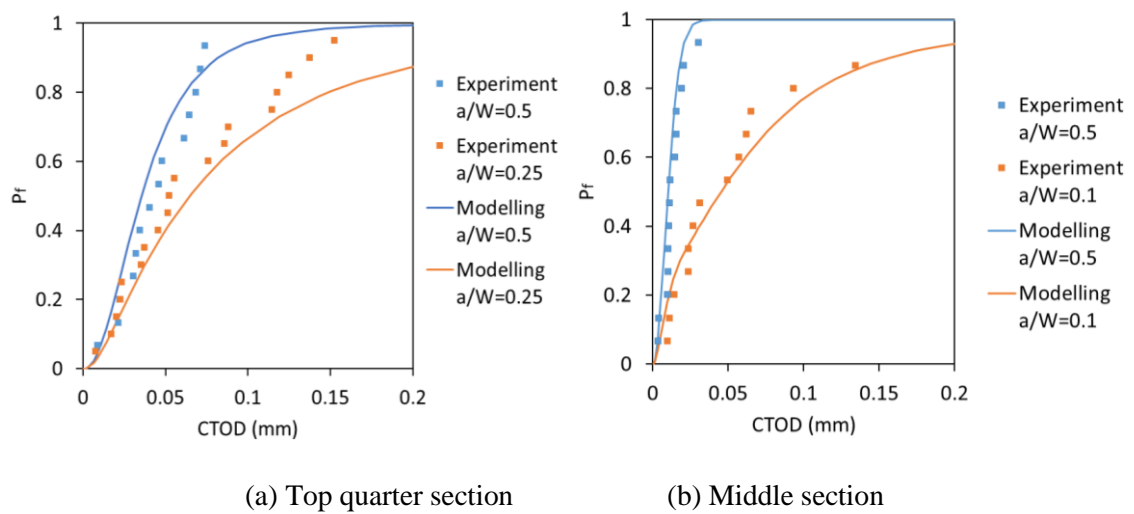
(a) Top quarter section   (b) Middle section

Fig 3. 14. P_f-CTOD curve of top quarter section in comparison with experimental data (dots are the experimental data and curves are the model predictions)

3.4.5 Fracture modelling considering the inclusion geometry

The above modelling of cleavage fracture with the assumption of spherical inclusions shows that the inclusions in the middle section are computed to have lower strength. One of the potential causes of the lower inclusion strength in the middle section can be related to the elongated inclusion shape. In order to explain the variety of inclusion strength determined in the cleavage fracture modelling, the developed analytical solution is used to calculate inclusion stress with (a) oblate and (b) prolate as shown in Fig 3. 15.
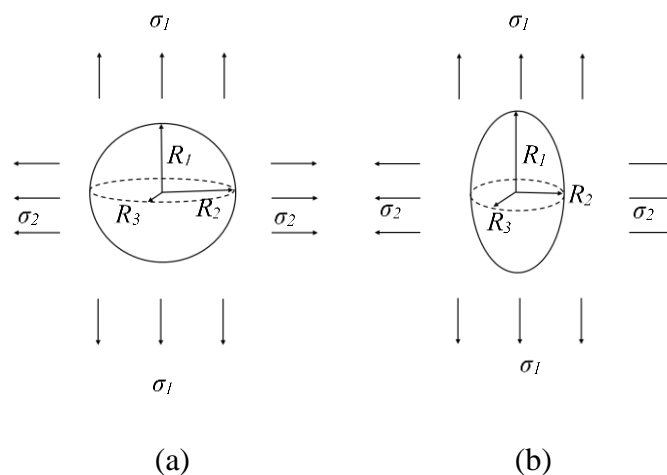

(a)   (b)

Fig 3. 15 (a) Oblate (R_1/R_2=1, R_2/R_3=2 or 3), and (b) prolate inclusions (R_1/R_2=2 or 3, R_2/R_3=1) with remote loading in plane strain

It has been observed that the inclusions in the middle section tend to have a longer axis along the RD and a shorter axis along the ND, as shown in Fig 3. 10. The aspect ratio of individual inclusions varies significantly. In this study, an assumption of aspect ratio of 2 and 3 is used to estimate the effect.

For both the oblate and prolate shapes, the minor axis lies along the ND, which is the out of plane direction of the SENB specimens, and the major axis lies perpendicular to the crack ($\theta=0°$). Table 3.7 shows the results of cleavage parameter determination considering the variety of inclusion geometry.

Table 3.7 Parameter values from inverse modelling considering inclusion geometry

Parameters	Oblate (R_1/R_2=1, R_2/R_3=2)	Oblate (R_1/R_2=1, R_2/R_3=3)	Prolate (R_1/R_2=2, R_2/R_3=1)	Prolate (R_1/R_2=3, R_2/R_3=1)
Crack arrest parameter of grain boundary: K_{Ia}^{mm} (MPa$\sqrt{\text{m}}$)	23.1	23.2	23.2	23.2
Critical stress for hard inclusion σ_H^C (MPa)	1350	1600	2100	2550

This example shows that the inclusion strength strongly depends on the inclusion shape, while the crack arrest parameter of the grain boundary is independent of inclusion features. Compared with Table 3.6, when the inclusions are modelled with shapes that are prone to cracking, a higher critical stress of hard inclusion is determined, as the stress concentration effect is considered in the calculation of inclusion stress.

Table 3.7 shows the critical inclusion stresses obtained from the cases Oblate (R_1/R_2=1, R_2/R_3=3) and Prolate (R_1/R_2=2, R_2/R_3=1) are closer to the values determined for the top quarter section. The prolate geometry would lead to anisotropy in the rolling direction and the longitudinal direction, while the oblate geometry does not. Since the microscopic observation and fracture tests only reveal anisotropy between the rolling direction and the normal direction, but not for the longitudinal direction, the oblate assumption is more sensible for the investigated material. Although the present example only shows the trend of critical inclusion stress versus inclusion shape, it proves the strong correlation between fracture modelling and the microstructural feature of inclusions. If the inclusion geometry and orientation can be determined in a statistical format, the developed solution is capable of exploring its effect on cleavage fracture with more detail.

3.5 Discussion

3.5.1 Capabilities of the model

In the above validations and applications, the analytical solution reflects the influence of several factors on the inclusion stress, which corresponds to the observations of hard inclusion behaviour in cleavage fracture that have been reported in literature. The following factors have been reflected:

(1) The stress level depends on the shape and orientation of the inclusion. The tensile stress on the inclusion is much more pronounced when the inclusion has its major axis along the remote first principal stress. This difference can explain the observation that particle fracture is often reported for elongated inclusions when loaded along their length [5].

(2) The representative inclusion stress increases with remote plastic strain when matrix hardening is considered. It agrees with the observation that plastic deformation is necessary for cleavage initiation even if the cleavage is stress-controlled [5].

(3) Various matrix plasticity parameters have been used to validate the solution. It is found that the inclusion stress increases with the yield stress of the matrix. It explains the observation that particle cracking is preferred in a hard matrix and a soft matrix favours particle decohesion [9].

3.5.2 Comparison with existing solutions

The analytical solution developed in this paper can also be compared with empirical equations. The empirical equations for the stress in an inclusion that have been used by other researchers are in a format similar to equation 2-6. [35] calculated the maximum principal stress at a cementite particle by:

$$\sigma_{1,inclu} = \frac{E_{inclu}}{E_{matrix}}\sigma_{1,matrix} + 0.179\sigma_y(\frac{\varepsilon_{p,matrix}}{\varepsilon_y})^{0.627}. \qquad \text{3-5-1}$$

[20] calculated the maximum principal stress in the M-A particle by:

$$\sigma_{1,inclu} = \sigma_{1,\text{matrix}} + 1.8(\sigma_{eq,matrix} - \sigma_{y,matrix}). \qquad \text{3-5-2}$$

[34] proposed an equation to calculate the particle stress and attempted to account for particle geometry and orientation with four empirical parameters:

$$\sigma_{1,inclu} = c_I\sigma_{1,\text{matrix}} + c_M c_{II}(\varepsilon_1)^{c_{III}}, \qquad \text{3-5-3}$$

while the determination of the c parameters is not explicit in the publication.

The proposed analytical solution eq. 3-2-6 can be written as an empirical equation fitted with the present results of FEA:

$$\sigma_{1,inclu} = \sigma_{1,matrix} + c_F\sigma_{eq,matrix}, \qquad \text{3-5-4}$$

where c_F is a fitted parameter related to the aspect ratio and orientation of the inclusion. For the case $\theta=0°$, the fitted relationship is:

$$c_F = 0.3026\frac{R_2}{R_1}. \qquad \text{3-5-5}$$

As introduced at the beginning of this paper, methods based on Eshelby tensors have been used to calculate the stress of inclusions. Beremin ductile fracture model provides equations in a similar format of eq. 3-2-6 [46]:

$$\sigma_{1,inclu} = \sigma_{1,\text{matrix}} + c_B(\sigma_{eq,matrix} - \sigma_y), \qquad \text{3-5-6}$$

where parameter c_B is determined analytically with the usage of Eshelby tensors. In the following discussion, Eq. 3-5-6 is used as the representative of Eshelby tensor-based equations to be compared with the present analytical solution.

Fig 3. 16 shows the performance of the developed analytical solution (eqs. 3-2-6 to 3-2-17), the fitted empirical equation (eqs. 3-5-4 and 3-5-5), and the solutions provided by other researchers (eqs. 3-5-1, 3-5-2 and 3-5-6), by comparing with FEA results. The comparison is in terms of the ratio $(\sigma_{1,inclu} - \sigma_{1,matrix})/\sigma_{eq,matrix}$. The matrix material is material A in Fig 3. 9 and comparison is at $\varepsilon_{p,matrix} = 0.05$. The comparison is based on spheroidal inclusions of various aspect ratios (R_1/R_2=0.5, 1, 1.5, and 2) with θ=0°. Among the considered equations, only the Shibanuma formula (eq. 3-5-1) always accounts for the elastic mismatch, which is not supported by the FE results. Eqs. 3-5-1 and 3-5-2 have the shortcoming of not reflecting the influence of particle geometry and orientation (which results in a single data point representing a spherical inclusion in Fig 3. 16). Eq. 3-5-3 attempts to reflect the particle geometry, but deviates from FEA results. Both the fitted empirical equation (eqs. 3-5-4 and 3-5-5) and the analytical solution (eqs. 3-2-6 to 3-2-17) in the present article give good predictions in terms of particle geometry. However, the empirical equations 3-5-4 and 3-5-5 are unable to take account of the orientation of the inclusion.
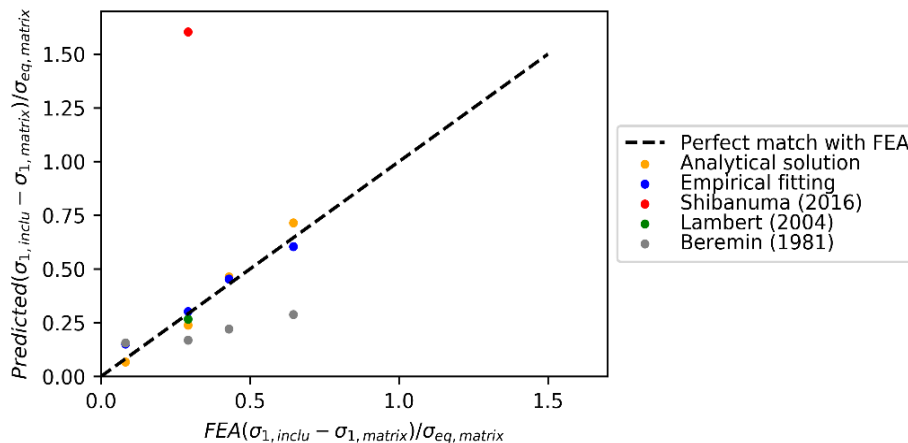

Fig 3. 16 Performance of the current developed analytical solution and empirical equations

As described in Part 1, Mean-Field method has been widely used in multi-scale material modelling. Fig 3. 17 shows the results by using the MF method in Abaqus 2017, which was adapted from [30], to analyse the inclusion problem (with R_1/R_2=1, η=0, matrix material A). Both the general method and the

spectral method [30] have been tested for the isotropization of the matrix material. The result shows that the two isotropization methods can well predict the matrix behaviour (which is equivalent to the macroscale behaviour in a dilute inclusion problem), but fail to predict the inclusion stress when the matrix material enters nonlinearity. It requires calibration from FEA to predict the stress concentration of inclusions in the case of highly nonlinear constituent materials.
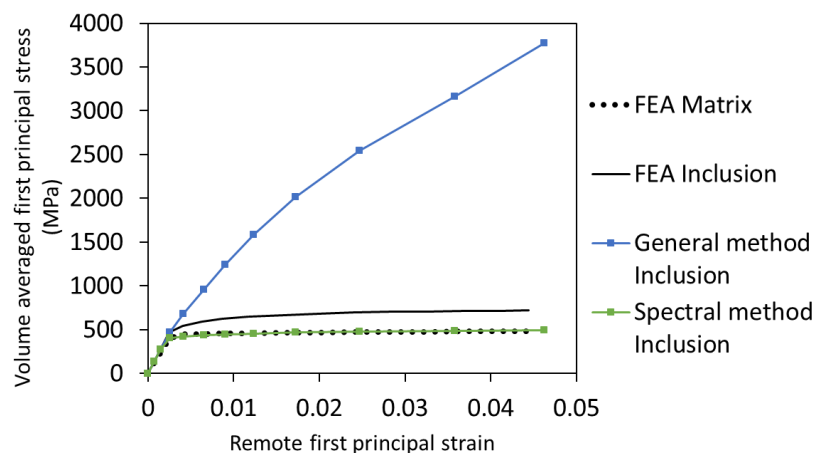

Fig 3. 17 Result of using Mean-Field method on the inclusion problem

3.5.3 Limitations

In general, the analytical equations derived in the present paper are able to involve several features as the inclusion geometry, the inclusion orientation, the far-field stress state and different matrix material properties. It should be noticed that the analytical solution is only suitable for the following situations:

(1) The inclusions are distributed sparsely in the matrix. The space between inclusions should be at least five times the inclusion diameter. Otherwise, there will be interaction between inclusions, which the developed solution does not account for.

(2) The matrix material has low-hardening behaviour after yielding. The presence of an inclusion will result in high local plastic strain in the matrix. If the matrix material has pronounced hardening behaviour after yielding, the local stress state in the matrix near the inclusion will be much higher than assumed. The stress in the inclusion will be underestimated by the analytical solution.

(3) The inclusion can be assumed as a spheroid. The analytical solution estimates the representative stress of the inclusion, which is an average stress over the midsection. If the inclusion has a very irregular shape, the average stress may not represent the stress level within the inclusion and the analytical solution should not be used.

3.6 Conclusions

This paper presents analytical equations to quantitatively calculate the stress on a hard inclusion from far-field stress on a matrix. The solution has been derived based on the assumption of shear-dominated behaviour in fully-formed plasticity. Validation was performed by numerical modelling of a microscopic hard inclusion in a high strength steel. The simulation validates the assumptions on which the analytical solution is based and estimates the performance of the analytical solution. Finally, the solution was demonstrated by using it in an existing statistical framework to model cleavage fracture in CTOD specimens.

The main conclusions are highlighted as the following:

(1) A set of analytical equations is established to quantitatively estimate the inclusion stress from far-field matrix stress. The analytical equations together with the classic Eshelby's solution are able to take account of the interaction of the far-field hydrostatic pressure and deviatoric stress.

(2) The analytical equations are able to take account of features such as the inclusion shape and the inclusion orientation. The prediction corresponds to the FEA results that the inclusion stress is much more pronounced for the inclusion that has its major axis along the remote first principal stress.

(3) The analytical equations give an approximate solution for the inclusion stress that is asymptotically approached in plastic deformation of low-hardening materials. The maximum error of $\sigma_{1,inclu}$-$\sigma_{1,matrix}$ is 25% for the studied cases. For materials with more pronounced hardening behaviour, the analytical solution is less satisfying.

The analytical solution to quantitively determine the stress on a microstructural hard inclusion can be used for the statistical characterization of macroscale cleavage fracture, and on the identification of anisotropic fracture behavior. It avoids costly numerical simulations when the features of microstructural inclusions vary widely in the steel and provides an efficient estimation of inclusion fractures in the cleavage process. Because the solution can account for multiple parameters, it can be used not only for a particular material but in general for high strength steels containing heterogeneous microstructures and under various loading patterns. The ductile damage mode is often modeled based on the assumption that hard particles separate from the surrounding matrix material. While it was not the purpose of this study, such a failure model may also benefit from the current developments if a failure model is applied to determine when decohesion occurs between the hard particle and the surrounding matrix.

References

[1] Lin, T., Evans, A. G., & Ritchie, R. O. (1986). A Statistical Model of Brittle Fracture by Transgranular Cleavage. Mrch. Phys. Solids, 34(5), 477–497.

[2] Martín-Meizoso, A., Ocaña-Arizcorreta, I., Gil-Sevillano, J., & Fuentes-Pérez, M. (1994). Modelling cleavage fracture of bainitic steels. Acta Metall. Mater., 42(6), 2057–2068.

[3] Pineau, A. (2008). Modeling ductile to brittle fracture transition in steels - Micromechanical and physical challenges. International Journal of Fracture, 150(1–2), 129–156.

[4] Chen, J. H., Li, G., Cao, R., & Fang, X. Y. (2010). Micromechanism of cleavage fracture at the lower shelf transition temperatures of a C–Mn steel. Materials Science and Engineering: A, 527(18–19), 5044–5054.

[5] Pineau, A., Benzerga, A. A., & Pardoen, T. (2016). Failure of metals I: Brittle and ductile fracture. Acta Materialia, 107, 424–483.

[6] Namegawa, T., Hoshino, M., Fujioka, M., & Minagawa, M. (2019). Effect of Carbon Content on Toughness of Tempered Martensitic Steels Analyzed by Toughness Prediction Model. ISIJ International, 59(7), 1337–1343.

[7] Jiang, Q., Bertolo, V. M., Popovich, V. A., & Walters, C. L. (2019). Recent Developments and Challenges of Cleavage Fracture Modelling in Steels: Aspects on Microstructural Mechanics and Local Approach Methods. Proceedings of the ASME 2019 38th International Conference on Ocean, Offshore and Arctic Engineering. Vol 4: Materials Technology.

[8] Ray, A., Sivaprasad, S., & Chakrabarti, D. (2012). A critical grain size concept to predict the impact transition temperature of Ti-microalloyed steels. International Journal of Fracture, 173(2), 215–222.

[9] Chen, J. H., & Cao, R. (2015). Micromechanism of Cleavage Fracture of Metals. Micromechanism of Cleavage Fracture of Metals.

[10] Jia, T., Zhou, Y., Jia, X., & Wang, Z. (2017). Effects of Microstructure on CVN Impact Toughness in Thermomechanically Processed High Strength Microalloyed Steel. Metallurgical and Materials Transactions A, 48(2), 685–696.

[11] Tankoua, F., Crépin, J., Thibaux, P., Cooreman, S., & Gourgues-Lorenzon, A. F. (2018). Quantification and microstructural origin of the anisotropic nature of the sensitivity to brittle cleavage fracture propagation for hot-rolled pipeline steels. International Journal of Fracture, 212(2), 143–166.

[12] Ghosh, A., Ray, A., Chakrabarti, D., & Davis, C. L. (2013). Cleavage initiation in steel: Competition between large grains and large particles. Materials Science and Engineering: A, 561, 126–135.

[13] Popovich, V. A., & Richardson, I. M. (2015). Fracture Toughness of Welded Thick Section High Strength Steels and Influencing Factors. TMS2015 Supplemental Proceedings, (March), 1031–1038.

[14] Pallaspuro, S. (2018). On the factors affecting the ductile-brittle transition in as-quenched fully and partially martensitic low-carbon steels. PhD thesis. Oulu University

[15] Bertolo, V.M, Jiang, Q., Walters, C.L., & Popovich, V.A. (2020). Effect of Microstructure on Cleavage Fracture of Thick-Section Quenched and Tempered S690 High-Strength Steel. In: Li J. et al. (eds) Characterization of Minerals, Metals, and Materials 2020: 155-168.

[16] Lindley, T., Oates, G., & Richards, C. . (1970). A critical of carbide cracking mechanisms in ferride/carbide aggregates. Acta Metallurgica, 18(11), 1127–1136.

[17] Ray, A., Paul, S. K., & Jha, S. (1995). Effect of Inclusions and Microstructural Characteristics on the Mechanical Properties and Fracture Behavior of a High- Strength Low- Alloy Steel. Journal of Materials Engineering and Performance, 4(6), 679–688.

[18] Bordet, S. R., Karstensen, A. D., Knowles, D. M., & Wiesner, C. S. (2005). A new statistical local criterion for cleavage fracture in steel. Part II: Application to an offshore structural steel. Engineering Fracture Mechanics, 72(3), 453–474.

[19] Miao, P., & Knott, J. F. (2016). Effects of Inclusions and Their Surface Chemistry on Cleavage Fracture in a C-Mn Steel Weld Metal. HSLA Steels 2015, Microalloying 2015 & Offshore Engineering Steels 2015, 1149–1161.

[20] Lambert-Perlade, A., Gourgues, A. F., Besson, J., Sturel, T., & Pineau, A. (2004). Mechanisms and modeling of cleavage fracture in simulated heat-affected zone microstructures of a high-strength low alloy steel. Metallurgical and Materials Transactions A: Physical Metallurgy and Materials Science, 35(13), 1039–1053.

[21] Huang,W. C. (1972). Theoretical study of stress concentrations at circular holes and inclusions in strain hardening materials. International Journal of Solids and Stuctures, 8, 149–192

[22] Lee, Y. S., & Smivri, L. C. (1981). Analysis of the stress concentration non-linear viscous material. Int. J. Mech. Sci,23(8), 487–496.

3

[23] Wilner, B. (1988). Stress analysis of particles in metals. Journal of the Mechanics and Physics of Solids, 36(2), 141–165.

[24] Lee, B. J. & Mear, M. E. (1999). Stress concentration induced by an elastic spheroidal particle in a plastically deforming solid. Journal of the Mechanics and Physics of Solids, 47, 1301–1336.

[25] Lauke, B. & Schüller, T. (2002). Calculation of stress concentration caused by a coated particle in polymer matrix to determine adhesion strength at the interface. Composites Science and Technology, 62(15), 1965–1978.

[26] Huang, M., & Li, Z. (2005). Size effects on stress concentration induced by a prolate ellipsoidal particle and void nucleation mechanism. International Journal of Plasticity, 21(8), 1568–1590.

[27] Gao, X. L. (2008). Analytical solution for the stress field around a hard spherical particle in a metal matrix composite incorporating size and finite volume effects. Mathematics and Mechanics of Solids, 13(3–4), 357–372.

[28] Eshelby, J. D. (1957). The determination of the elastic field of an ellipsoidal inclusion, and related problems. Proceedings of the Royal Society of London. Series A, 241, 376-396.

[29] Mori, T., Tanaka, K. (1973). Average stress in matrix and average elastic energy of materials with misfiting inclusions. Acta Metall. 21: 571–574.

[30] Doghri, I., & Ouaar, A. (2003). Homogenization of two-phase elasto-plastic composite materials and structures study of tangent operators, cyclic plasticity and numerical algorithms. International Journal of Solids and Structures, 40(7), 1681–1712.

[31] Pierard, O., González, C., Segurado, J., LLorca, J., & Doghri, I. (2007). Micromechanics of elasto-plastic materials reinforced with ellipsoidal inclusions. International Journal of Solids and Structures, 44(21), 6945–6962.

[32] Delannay, L., Doghri, I., & Pierard, O. (2007). Prediction of tension-compression cycles in multiphase steel using a modified incremental mean-field model. International Journal of Solids and Structures, 44(22–23), 7291–7306.

[33] Brassart, L., Doghri, I., & Delannay, L. (2010). Homogenization of elasto-plastic composites coupled with a nonlinear finite element analysis of the equivalent inclusion problem. International Journal of Solids and Structures, 47(5), 716–729.

[34] Hardenacke, V., Hohe, J., Friedmann, V., & Siegele, D. (2012). Enhancement of local approach models for assessment of cleavage fracture considering micromechanical aspects. In 19th

3

European Conference on Fracture: Fracture of Materials and Structures from Micro to Macro Scale.

[35] Shibanuma, K., Aihara, S., & Suzuki, K. (2016). Prediction model on cleavage fracture initiation in steels having ferrite-cementite microstructures - Part II: Model validation and discussions. Engineering Fracture Mechanics, 151, 181–202.

[36] Mura, T. (1987). Micromechanics of defects in solids. Kluwer Academic Publishers.

[37] Bannister, A. C., Ruiz Ocejo, J., & Gutierrez-Solana, F. (2000). Implications of the yield stress/tensile stress ratio to the SINTAP failure assessment diagrams for homogeneous materials. Engineering Fracture Mechanics, 67(6), 547–562.

[38] Ludwik, P., & Scheu. R. (1923). Ueber Kerbwirkungen bei Flusseisen, Stahl U. Eisen, vol. 43.

[39] Lamagnere, P., Girodin, D., Meynaud, P., Vergne, F., & Vincent, A. (1996). Study of elasto-plastic properties of microheterogeneities by means of nano-indentation measurements : application to bearing steels, Materials Science and Engineering A, 215, 134–142.

[40] Chen, D., Li, R., Lang, D., Wang, Z., Su, B., Zhang, X., & Meng, D. (2017). Determination of the mechanical properties of inclusions and matrices in α-U and aged U-5.5Nb alloy by nanoindentation measurements. Materials Research Express, 4, 116516.

[41] Gu, C., Lian, J., Bao, Y., Xiao, W., & Münstermann, S. (2019). Numerical study of the effect of inclusions on the residual stress distribution in high-strength martensitic steels during cooling. Applied Sciences (Switzerland), 9(3), 455.

[42] Thomson, R. D., & Hancock, J. W. (1984). Local stress and strain fields near a spherical elastic inclusion in a plastically deforming matrix. International Journal of Fracture, 24(3), 209–228.

[43] Wuertemberger, L., & Palazotto, A. N. (2016). Evaluation of Flow and Failure Properties of Treated 4130 Steel. Journal of Dynamic Behavior of Materials, 2(2), 207–222.

[44] International Standard (2015) ISO 12135: metallic materials – unified method of test for the determination of quasistatic fracture toughness.

[45] Andrieu, A., Pineau, A., Besson, J., Ryckelynck, D. & Bouaziz, O. (2012). Beremin model: Methodology and application to the prediction of the Euro toughness data set. Engineering Fracture Mechanics. 95: 102-117.

[46] Beremin, F. M. (1981). Cavity formation from inclusions in ductile fracture of A508 steel. Metallurgical Transactions A, 12, 723–731.

4

Microstructure-informed statistical modelling of cleavage fracture in high strength steels considering through-thickness inhomogeneities

Abstract

Thick section S690 QT steel is modelled with a modified multibarrier model that is based on the weakest-link mechanism. Segregation bands are modelled as discrete layers which have different grain size, yield properties, and local fracture parameters from outside of the bands. The results show that embrittlement from segregation bands can only be adequately reflected if the inhomogeneities of the fracture parameters are accounted for. The present methodology quantitively captures the cooperation of complex microstructural features in cleavage and can facilitate the trade-off between the effects of various microstructural parameters in toughness control.

4.1. Introduction

Toughness of ferritic steels at low temperatures and the ductile-to-brittle transition temperature region are related to transgranular quasi-cleavage fracture, which will be called cleavage in this paper. In most engineering applications, the trade-off between various controllable parameters (e.g. weld travel speed, process, wire composition, cooling rate, etc.) to generate both cost-effective and sufficiently tough base metal/weld/HAZ (heat-affected zone) combination is accepted (e.g. [1]). These processing

parameters determine the microstructure of the material, such as prior austenite grain size [2], carbide size [3], the presence of inclusions [4], M-A (martensite-austenite) phases [5], precipitates, etc. (for an overview, see [6]). As a highly localized phenomenon, cleavage fracture exhibits strong sensitivity to material characteristics at the microstructural level, dependent on composition and structure fabrication, and it is coupled with a constraint effect originating from the macroscopic stress state. This coupling complicates the development of fracture mechanics assessments based on available standard specimen data. Many studies have attempted to correlate the toughness and microstructural parameters of steels [3-11], but most of them are descriptive rather than predictive.

The local approach to cleavage fracture is a class of physically-driven statistical models that account for the probability of failure based on the local stress (and sometimes strain) field [12]. [13] and [14] proposed the Weibull formulation based on the weakest-link mechanism. Following these studies, many attempts were made to quantitatively predict the scatter in the toughness [15-20]. More recently, other studies have tried to predict the toughness of steels from their microstructural parameters [21-23]. These efforts have shown the potential effectiveness of the local approach to cleavage fracture. However, the gradient of properties through the thickness and welded zones makes it impossible to predict and control cleavage fracture based only on a single microstructural region [24-26].

The need for more accurate cleavage modelling is particularly acute for a new generation of high- and very high-strength steels (yield strength of 500 to 1300 MPa) because they obtain their favorable properties through complex, multi-phase microstructures, which complicates microstructural modelling of cleavage-driven failure. The rolling of thick plates can also give rise to so-called segregation bands or spatial segregation of both alloying and impurity elements [27, 28]. The consequence of such inhomogeneous and multiphase microstructures is a large scatter of properties through the thickness.(e.g. [29]). It is reported that up to 90% of brittle failure originates from the middle third of the material thickness [30], which indicates the importance of the centerline and possible segregation zones [31]. Macroscopic inhomogeneities, including macro-segregation and HAZ, have been modelled by bimodal methods [32-33], where the variations in cleavage properties are represented by macroscopic toughness parameters. The bimodal methods are not applicable to modelling segregation bands that are too small to extract specimens to determine those macroscopic parameters. Hence, to judge the susceptibility of such steel structures to catastrophic failures and to design future generations of improved steels, a quantitative, physically-based method taking into account the statistical and multi-parametric nature of steel microstructures is required.

A statistical method is proposed in this paper for the modelling of cleavage fracture based on microstructural parameters. The statistical model is a multi-barrier model that accounts for microcrack nucleation at hard inclusions and microcrack propagation based on the weakest-link mechanism. This

model is validated with previously published experimental data, which includes specimens of S690 QT steel plate fractured at -100 ℃ and corresponding characterization of microstructures. Specimens taken from top quarter and middle-section of the plate have different microstructures, and their measured crack tip opening displacement (CTOD) values differ significantly. Centreline segregation bands appear in the middle section specimens, producing significant inhomogeneities. Approaches of modelling the segregation bands ("Yield and grain size variation method" and "Cleavage variation method") are compared in this paper to determine the transferability of microstructural fracture parameters through the thickness and to investigate the total effect of segregation bands on cleavage fracture.

4.2. Model description

4.2.1 Micromechanism of cleavage fracture

The model developed in this paper is based on a multiple-barrier theory of the cleavage mechanism [34-37]. The modelling of fracture toughness is based on a local fracture criterion and then is upscaled from unit volume to a specimen.

In the proposed model, cleavage fracture of ferritic steels is regarded as the result of successive occurrence of three events (Fig 4. 1):

I: nucleation of the slip-induced crack at a brittle second-phase particle (i.e., carbides in steels) or inclusion. Plastic flow is a necessary precursor, which might be by slipping or twinning.

II: propagation of the microcrack across the particle/matrix interface under the local stress state.

III: propagation of the grain-sized crack to neighbouring grains across the grain boundary under the local stress state.
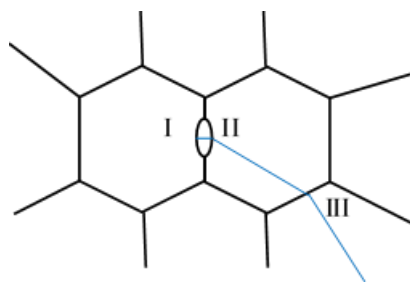

Fig 4. 1 Critical events of cleavage fracture

Inclusions and second phase particles are associated with the fracture initiation (event I). Under plastic flow, stress in a second phase particle is raised to a level to nucleate a microcrack. If the particle is brittle and deforms elastically during cracking, a single-parameter condition can be motivated for crack nucleation, where a critical-strain-based model can be transformed into a critical-stress-based model. The stress level needed for inclusion cleavage is characterized by critical particle strength σ_H^C.

Based on observations in [13][18], hard particle cracking only occurs after local yielding of the matrix, and the number of cracked particles is found to be in proportion to plastic strain in notched tensile bar tests. These facts indicate that σ_H^C is commonly higher than the peak stress in a specimen at the start of local yielding, and σ_H^C shows noticeable scatter. Here it is assumed the value of inclusion strength is uniformly distributed in the range [σ_H^C, $\sigma_H^C + \Delta \sigma_H^C$], as shown in Fig 4. 2. For a volume that contains N inclusions, the number of cracked inclusions (N_{cr}) is in proportion to the inclusion stress σ_H and can be calculated as

$$N_{cr} = \min\{N \times (\sigma_H - \sigma_H^C)/\Delta \sigma_H^C, N\}. \qquad \text{4-2-1}$$

Where the inclusion stress σ_H is calculated from the first principal stress of the matrix $\sigma_{1,matrix}$ and the equivalent von-mises stress of the matrix $\sigma_{eq,matrix}$, by

$$\sigma_H = \sigma_{1,matrix} + f_\alpha \sigma_{eq,matrix}, \qquad \text{4-2-2}$$

and the factor f_α is determined using the analytical solution in [38] based on the inclusion geometry. In eq. 4-2-2, $\sigma_{eq,matrix}$ increases with plastic strain for a strain-hardening material, and f_α is always positive for an elastic inclusion. As a result, the calculated inclusion stress σ_H increases with plastic strain, and given eq. 4-2-1, the number of cracked particles also increases with plastic strain.
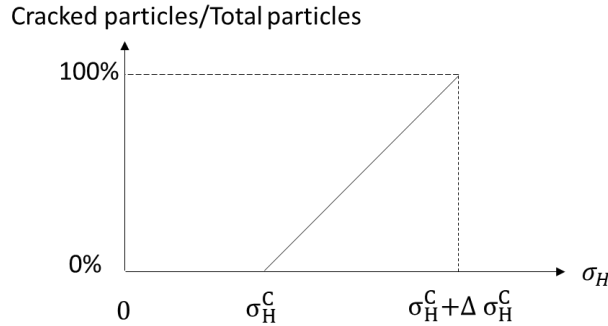

Fig 4. 2 Number of cracked particles vs maximum principal stress inside hard particles

Phase boundaries and grain boundaries in ferritic steels offer important resistance to the propagation of cleavage cracks (event II and III). The critical stress is usually used as a criterion for the crack propagation across the particle/matrix interface or across the grain boundary. The critical stress for a micro-crack to propagate within a grain has been related to the Griffith theory [39] based on energy balance. [6] has confirmed that an approximate relationship between σ_f (fracture stress) and $D^{-1/2}$ (root of grain diameter) exists. In the present paper, the particle/matrix interface strength is characterized by the local cleavage parameter K_{Ia}^{pm} and the grain boundary strength is characterized by the local cleavage parameter K_{Ia}^{mm}. A minimum particle size (d_c) and a minimum grain size (D_c) are calculated

for the first principal stress within the grain ($\sigma_{1,matrix}$) to propagate the micro-crack across the particle/matrix interface and grain boundary, by:

$$d_c = (K_{Ia}^{pm}/\sigma_{1,matrix})^2 \qquad\qquad 4\text{-}2\text{-}3$$

$$D_c = (K_{Ia}^{mm}/\sigma_{1,matrix})^2. \qquad\qquad 4\text{-}2\text{-}4$$

4.2.2 Microstructure-informed statistical model

This section outlines the computational model to calculate the cleavage probability of macroscale specimens. Finite element analysis (FEA) of a macroscopic volume gives the result of stress/strain distribution under a certain global load level. The stress calculated from FEA of each finite element will be used to calculate the cleavage probability of that finite element. The cleavage probability is calculated from a cleavage check based on the stress level, shape of the stress field, and statistical information of the microstructure. For a certain microstructure, the failure probability is a function of stress level and will be evaluated based on the volume of finite element. By accounting for the cleavage probability of all finite elements in the fracture process zone (areas that are plastically deforming), the total failure probability of the specimen can be calculated and can be expressed as a function of the global load. Fig 4. 3 gives a flow chart of the computational model to calculate the cleavage probability of macroscale specimens. The required inputs include FEA results (which contain $\sigma_{1,matrix}$, $\sigma_{eq,matrix}$, and $\varepsilon_{plastic}$ values within each finite element at each load increment), f_α calculated from inclusion geometry, the distribution density function of the grain major axis $f_g(D)$, the distribution density function of the hard particle major axis $f_p(d)$, number of inclusions N per elementary volume, cleavage parameters K_{Ia}^{pm}, K_{Ia}^{mm} and σ_H^C. Other parameters need to be defined are threshold plastic strain $\varepsilon_{plastic,thre}$, elementary volume V_0, and scatter of the inclusion fracture strength $\Delta\sigma_H^C$. Further explanation and definitions of the process depicted in Fig 4. 3 are given in the following paragraphs.

The cleavage probability of element j under load level i is noted as $P_{f,ij}$, and the cleavage probability of the specimen in the load increment i is noted as $P_{f,i}$. The cumulative cleavage probability of the specimen is calculated based on the following steps:

(1) Calculate the inclusion stress from $\sigma_H = \sigma_{1,matrix} + f_\alpha\sigma_{eq,matrix}$ and check if the inclusion stress exceeds the critical value σ_H^C.

(2) If the inclusion stress exceeds the critical value to nucleate a crack (σ_H^C), a minimum inclusion size d_c and a minimum grain size D_c are calculated for the first principal stress within the grain ($\sigma_{1,matrix}$) to propagate the crack across interface or boundary.

4

(3) A cleavage probability $P_{f,ij}$ is calculated as the integral of probability density that hard particles larger than the minimum particle size d_c and grains larger than the minimum grain size D_c, by

$$P_{f,ij} = \int_{D_c}^{+\infty} f_g(D)\, \mathrm{d}D \int_{d_c}^{+\infty} f_p(d)\, \mathrm{d}d. \qquad 4\text{-}2\text{-}5$$

(4) If $\sigma_{H,i} > \sigma_{H,i-1}$, the number of newly cracked inclusions ΔN_{cr} per elementary volume (V_0) is calculated by

$$\Delta N_{cr} = N \times (min\{\sigma_{H,i},\ \sigma_H^C + \Delta\,\sigma_H^C\} - max\{\sigma_{H,i-1},\ \sigma_H^C\})/\Delta\,\sigma_H^C. \qquad 4\text{-}2\text{-}6$$

(5) The cleavage probability $P_{f,ij}$ of the element j is modified based on the number of newly cracked inclusions and volume of the finite element V_j. The cleavage probability $P_{f,i}$ of the specimen in the load increment i is updated as $1 - (1 - P_{f,i})(1 - P_{f,ij})^{\Delta N_{cr}V_j/V_0}$.

(6) If the inclusion stress exceeds the critical value $\sigma_H^C + \Delta\,\sigma_H^C$, which means the number of cracked inclusions reaches N per elementary volume, the corresponding finite element will be deactivated for the rest of load steps for cleavage (which implies that the element still carries load but is assumed to not contain any newly cracked inclusions).

(7) After looping over all finite elements, the cumulative cleavage probability of the specimen is updated as:

$$P_f = P_{f,i-1} + \left(1 - P_{f,i-1}\right) \times P_{f,i}. \qquad 4\text{-}2\text{-}7$$

When the computation is finished, the output is the fracture probability of each load step, in terms of CTOD value. This procedure is shown in Fig 4. 3.
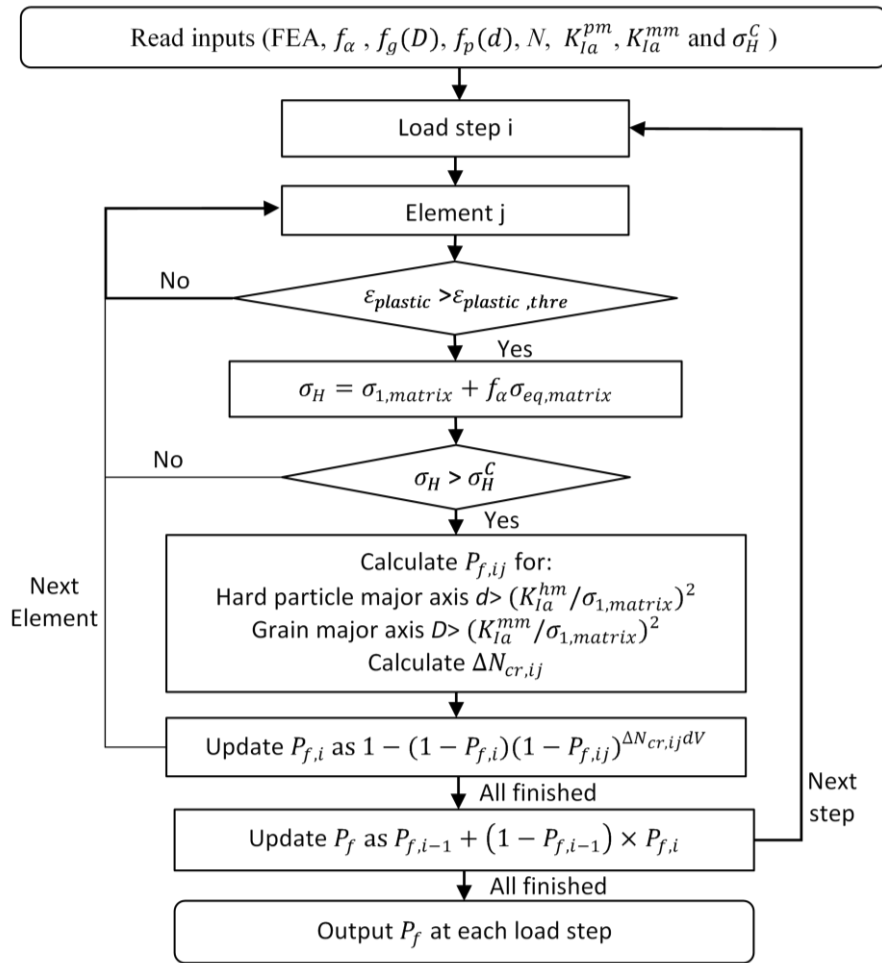
Fig 4. 3 Flow chart of the computational scheme

4.3. Material

A commercially available 80 mm thick quenched and tempered S690 high strength steel plate is used in this paper for illustration and validation of the developed model. Materials are extracted from the top quarter section and the middle section of the plate. The materials have been previously characterized in [40, 41]. The chemical composition of top quarter and middle sections of the steel plate was studied by XRF (X-ray fluorescence) and LECO combustion analysis [40]. The chemical composition of the steel plate is shown in Table 4.1.

Table 4.1. Chemical composition of S690 QT [40]

wt (%)	Fe	C	Si	Al	Mo	Other
Top	Bal.	0.17 ± 0.001	0.29 ± 0.022	0.07 ± 0.005	0.30 ± 0.007	Mn, Ni, Cr, Nb
Middle	Bal.	0.160 ± 0.001	0.30 ± 0.03	0.08 ± 0.01	0.29 ± 0.02	

The through thickness microstructure of the steel plate was analysed by means of scanning electron microscopy (SEM) with 5% Nital immersion etching for 15s [40]. The microstructure of the plate varies through the thickness from a fully tempered martensitic structure in the regions close to the surfaces to a mixed tempered martensitic-bainitic structure in the middle section of the plate. Centreline segregation bands (CLs) appear in the middle section.

4.3.1 Volume fraction and spacing of CLs

It is observed that the CLs form layers parallel to the rolling direction and are sparsely distributed near the centreline of the plate, as shown in Fig 4. 4 (a). The section containing the CLs has an average thickness of approximately 8 mm. Microscopic image (Fig 4. 4 b) shows RD,ND plane intersecting the CLs. The mean thickness of each band is measured as 0.1 mm. The mean spacing between bands is measured as 0.2 mm.
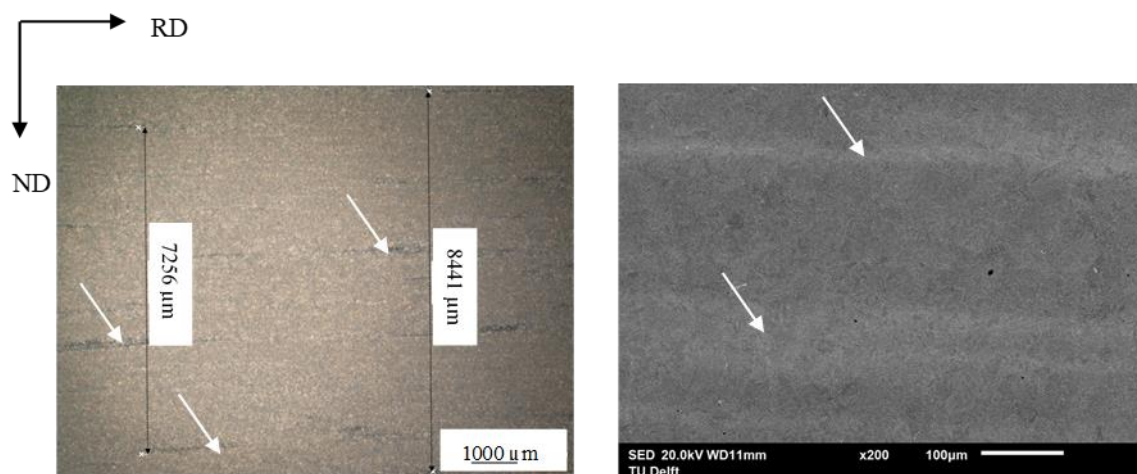
(a) distribution of CLs   (b) spacing and thickness of CLs

Fig 4. 4 Microscopic images of CLs (shown by white arrows) at middle section

4.3.2 Grain size

For the prior austenite grain (PAG) investigation, samples were swab etched with 100 ml saturated aqueous picric acid solution and 0.5g of sodium dodecyl benzene sulfonate etching for 5 min [41]. From analysis on the reconstructed Prior Austenite Grains (PAG) the statistical distribution of grain size has been measured in the top section, within CLs and outside CLs in the middle section of the steel plate. Fig 4. 5 shows one example of the reconstructed PAG map in the middle section.
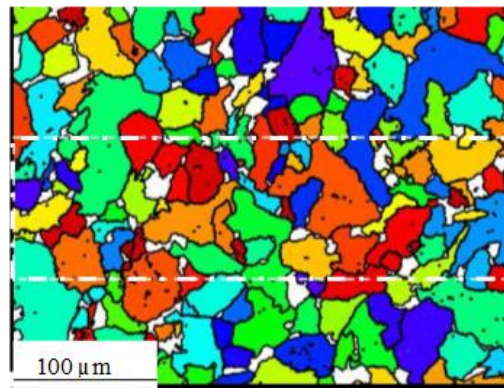
Fig 4. 5 Reconstructed PAG map for the middle section including the CL (white rectangle) [41]

To quantify the grain size in cleavage modelling, least-square fitting is performed on the grain size data to get the function representing the distribution:

$$P(\text{major axis} > D) = \min\left\{1 - \text{lognormalCDF}(D, \mu, S), \frac{\alpha}{D^\beta}\right\} \qquad \text{4-3-1}$$

where α and β are fitting parameters, and $\text{lognormalCDF}(D, \mu, S)$ represents equation $1/2 + 1/2erf(\frac{lnD - \mu}{\sqrt{2}\,S})$, where μ is the mean and S is the standard deviation.

Fig 4. 6 shows the grain size data with the fit of eq. 4-3-1, with the fitting parameters in Table 4.2, zoomed in on the large grains. Note that because eq. 4-3-1 is a composite of two distributions that it might become discontinuous in the transition from one distribution to the other. The top sections have smaller grains and the microstructure outside CLs in the middle section has larger grains, while CLs have an intermediate grain size. The ratio of major axis of grains in the top section, outside CL and within CL is 1.10: 1.00: 0.86.
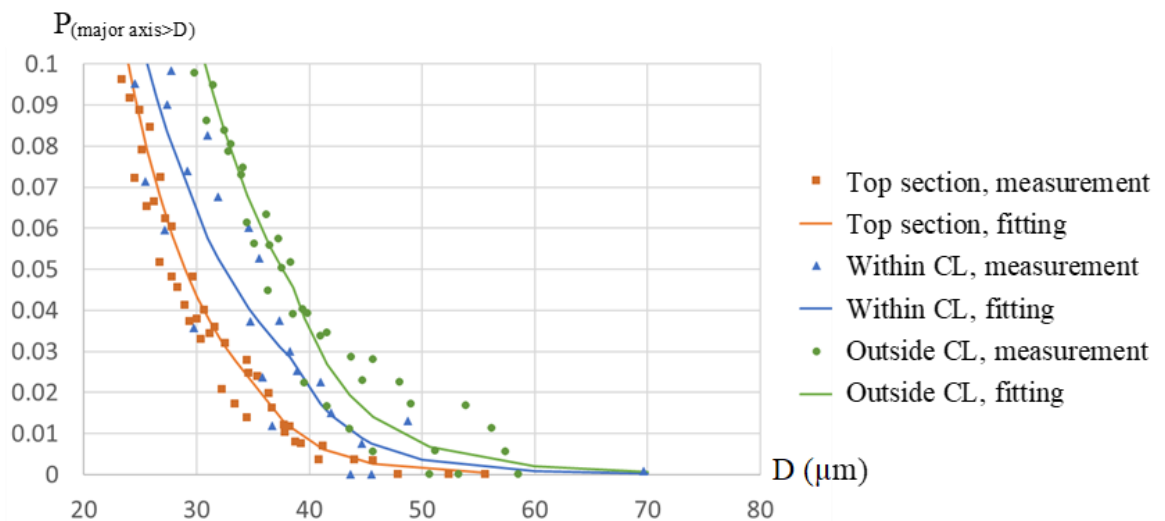

Fig 4. 6 Distribution of the major axis of PAG

Table 4.2 Parameters used to quantify grain size distributions (μ, S in μm, α, β correspond to D in μm)

Values for Top	Values for Middle	
	Outside CLs	Inside CLs
$\mu = 2.50$ $S = 0.53$ $\alpha = 2.46 \times 10^{17}$ $\beta = 12.24$	$\mu = 2.79$ $S = 0.52$ $\alpha = 4.80 \times 10^{9}$ $\beta = 6.95$	$\mu = 2.52$ $S = 0.59$ $\alpha = 5.01 \times 10^{10}$ $\beta = 7.73$

4.3.3 Inclusions

SEM with Energy-dispersive X-ray spectroscopy (EDS) was used to study morphology and chemical composition of inclusions, while quantification was performed by Keyence optical microscope [40]. Spherical inclusions and second-phase particles were observed through the full thickness, including oxides and nitrides of rather complex chemical composition such as (Mg,Ti)(O,N), (Mg,Al,Ca)(O,N) and (Mg,Al,Ca,Ti)(O,N). In the middle position, in addition to the spherical inclusions, cubic and elongated inclusions were observed. Niobium-rich carbides and nitrides such as (Ti,Nb)(N), (Ti,Nb)(C), Nb(C), and (Nb,Ti)(C,N) are present in the middle position. Fig 4. 7 shows the statistical distribution of oxides and Nb inclusion sizes measured in top quarter specimens and middle section specimens. For oxides, the difference between these two locations is very slight. For Nb inclusions, the density in the middle section is much higher, and the Nb inclusions tend to have larger length compared to oxide inclusions. Least-square fitting with eq. 4-3-2 is performed on the inclusion size data to obtain the parameters. The parameters of two types of inclusions are listed in Table 4.3.

$$P(\text{Diameter or major axis} > d) = \ \min\left\{1 - \text{lognormalCDF}(d, \mu, S), \frac{\alpha}{d^{\beta}}\right\} \qquad \text{4-3-2}$$

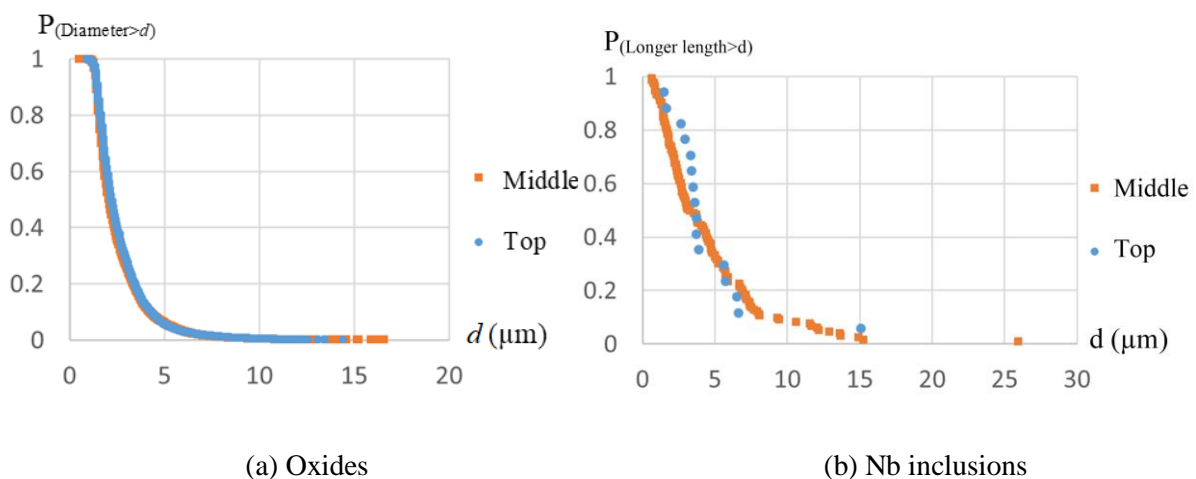

(a) Oxides (b) Nb inclusions

Fig 4. 7 Statistical distribution of inclusion size at top quarter and middle section

Table 4.3 Parameters quantify inclusion size and density

Parameters	Values for Top	Values for Middle
Number of oxides per 0.001 mm^3	43	38
Number of Nb inclusions per 0.001 mm^3	1	13
Diameter of oxides (μm)	$\mu = 0.85$, $S = 0.50$ $\alpha = 18.32$, $\beta = 3.57$	$\mu = 0.81$, $S = 0.52$ $\alpha = 31.64$, $\beta = 3.86$
Major axis of Nb inclusions (μm)	$\mu = 1.15$, $S = 0.86$ $\alpha = NA$, $\beta = NA$*	$\mu = 1.25$, $S = 0.72$ $\alpha = 121.93$, $\beta = 3.07$

* α and β are not applicable to Nb inclusions in the top quarter section because the number of observed Nb inclusions is not enough for the fitting.

4.3.4 Yield properties

Tensile tests were performed [40] according to ISO 6892-3 [42] at -100 °C using cylindrical specimens, in three different orientations relative to the rolling direction: parallel, perpendicular and 45°. All tensile specimens were tested at a deformation rate of 1.2 mm/s in order to apply similar strain rate conditions as in CTOD specimens. The true-stress vs true-strain curves are present in Fig 4. 8. Tensile tests of specimens taken from the top and middle sections of the plate indicate that the material at the top section has a higher yield strength and slightly lower degree of hardening. The stress-strain relationship of the steel is characterized by Ludwik's law, which is defined with the flow stress (σ) and the effective plastic strain (ε_p) as:

$$\sigma = \sigma_y + K\varepsilon_p^{n_L}. \qquad\qquad 4\text{-}3\text{-}3$$

where K and n_L are material parameters. The parameters of Ludwik's law are fitted from tensile tests and the fitted stress-strain curves are shown in Fig 4. 8. Regarding the effect of orientation, for both thickness positions – top and middle –there is no significant and clear effect of orientation in tensile properties for this material at -100 °C. Therefore, the materials are considered isotropic.
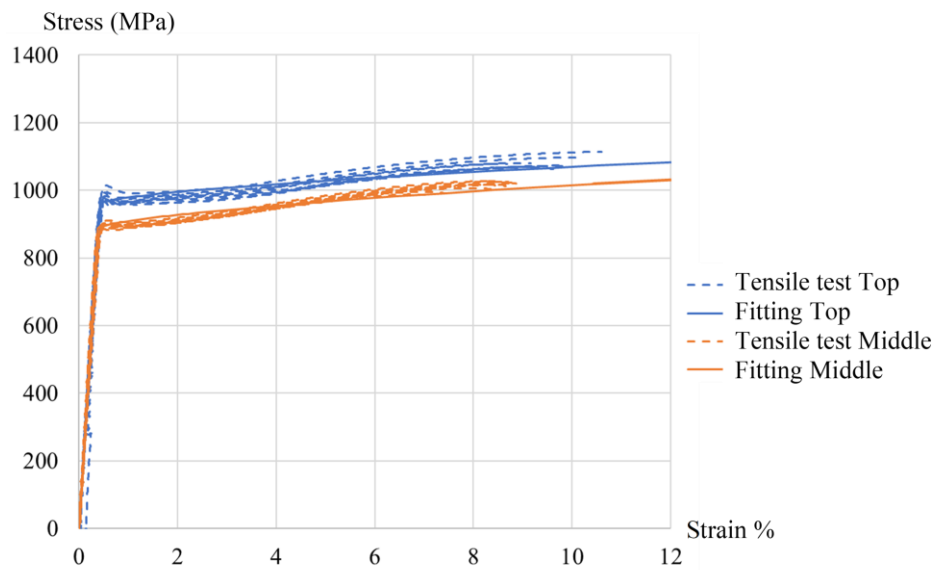
Fig 4. 8 True stress vs True strain curve of tensile tests and fitting with eq. 4-3-3 (tensile test curves are plotted until the maximum stress)

In order to extract the constitutive parameters of the CLs and quantify the variation of local yield parameters in the middle section specimens, nano-indentation measurements have been performed at room temperature [41]. Fig 4. 9 shows one indentation map where CLs appear. The average hardness values within the CLs are 35% higher than the values outside CLs.
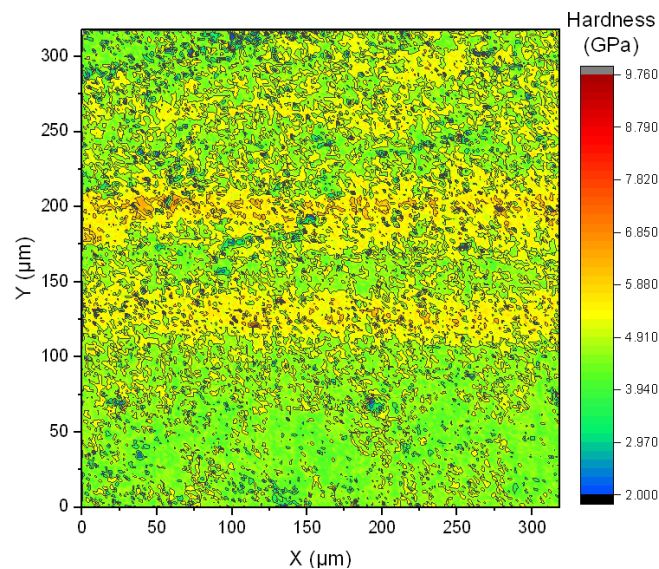

Fig 4. 9 Hardness map from nano indentations within CLs and outside CLs [41]

Inverse analysis method proposed by [43] is used to determine the Young's modulus, yield strength and Hollomon hardening exponent from the load-depth curves of the nano-indentation measurements. As expected, little variation of Young's modulus is observed inside and outside CLs. The hardening

behaviour of the material is found to be very slight for all indentations, with average value for the Hollomon exponent of 0.006 and standard deviation of 0.032. Therefore, the main distinction in the constitutive parameters is reflected by the yield strength. Table 4.4 shows the mean value and standard deviation (S) of the yield strength calculated from the locations within and outside CLs in the middle specimen.

Table 4.4 Yield strength determined by nano-indentation at room temperature

Locations	Mean value (MPa)	S (MPa)
CLs	2050	425
Outside CLs	1739	336

The yield strength of the middle section calculated from the nano-indentation test is higher than the value determined from macroscopic tensile tests. This can be explained by the small scale of the indentation (average indentation depth is smaller than 100 nm) and the possibility that the indentations are partially at particles or carbides. Therefore, instead of directly using values in Table 4.4 as the yield strength for modelling, a relative ratio of the yield strength $\sigma_{y,CL}/\sigma_{y,Out\ CL} = 2050/1739 = 1.18$ is calculated between the location within and outside CLs and is later used to model the segregation bands.

4.3.5 Fracture toughness tests

Fracture toughness tests were performed [40] according to the standard ISO 12135 [44] at -100 °C using sub-sized Single Edge Notched Bending (SENB) specimens, with dimensions of 20 mm × 10 mm × 92 mm, crack depth to width ratio a/W of 0.5, 0.25, and 0.1 and on both L-T and T-L orientations (as defined in [44]). All fracture specimens were tested in 3-point bending at a loading rate of 2 mm/s using a MTS servo hydraulic. A summary of the measured crack-tip-opening-displacement (CTOD) values is present in Table 4.5. The CTOD values for the top section are greater than for the middle and specimens in low-constraint condition exhibit much higher CTOD values than those of high constraint. There is no significant and clear effect of orientation on toughness, and the data of L-T and T-L are mixed for further analysis in this paper.

Table 4.5 Summary of fracture toughness test results [40]

Constraint		Position	Orientation	Average CTOD [mm]	Number of specimens
High constraint	a/W=0.5	Top Quarter	T-L	0.048 ± 0.019	10
			L-T	0.036 ± 0.025	4
		Middle	T-L	0.011 ± 0.001	6
			T-L	0.012 ± 0.006	8
Low constraint	a/W=0.25	Top Quarter	T-L	0.067 ± 0.045	18
	a/W=0.1	Middle	T-L	0.034 ± 0.031	6
			L-T	0.046 ± 0.018	7

The failure probability, P_f, of a specimen fractured in experiment, was calculated as a rank probability:

$$P_f = \frac{i - 0.3}{N + 0.4}$$

4-3-4

where *i* is the rank number in terms of CTOD and *N* is the total number of experiments.

4.4. Method

The data sets include deep cracked and shallow cracked specimens taken from the top quarter section and middle section of the S690 QT steel plate. The developed model is firstly applied on the top section specimens to determine the dominant micro-features in the cleavage process and the associated parameters. The model is then applied on the middle section specimens to investigate the modelling of CLs in cleavage fracture.

4.4.1 FE model and input parameters

The geometry of the specimen is shown in Fig 4. 10 and specified in Table 4.6. For top quarter section specimens, geometry of a/W=0.5 and a/W=0.25 are considered as high (deep-cracked) and low (shallow-cracked) constraint conditions, respectively. For middle section specimens, geometry of a/W=0.5 and a/W=0.1 are considered as high and low constraint conditions, respectively.
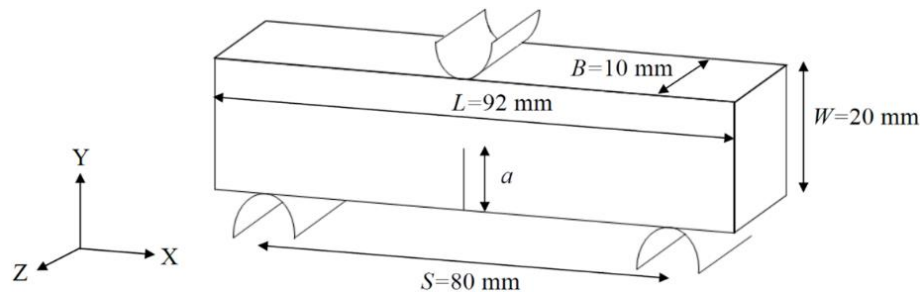

Fig 4. 10 Geometry layout of the SENB specimen

Table 4.6 Geometric information of the initial crack length

Constraint	Position in material	Crack length, *a* (notch length + prefatigued crack length) [mm]
a/W=0.5	Top quarter section Middle section	10 mm (8.6 mm + 1.4 mm)
a/W=0.25	Top quarter section	5 mm (3.6 mm + 1.4 mm)
a/W=0.1	Middle section	2 mm (0.6 mm + 1.4 mm)

SENB specimens with the geometry specified in Table 4.6 are modelled in Abaqus 2017. In total, four analyses are performed to consider the variety of initial crack length and material properties. For

each analysis, a quarter of the specimen ($L/2 \times B/2 \times W$) is modelled as a 3D deformable solid by using symmetry. The support and load roller are modelled as analytical rigid surfaces. The contact surface between rollers and the specimen is frictionless. Fig 4. 11 (a) shows the 3D model of a quarter of the specimen and two rollers. Fig 4. 11 (b) shows the mesh near the crack tip. The initial prefatigued crack tip is modeled as a finite notch that is 0.005 mm in radius. According to algorithm used by [45], this finite notch is small enough to model the near-crack-tip-field for the CTOD value considered in this study. A 20-noded hexahedral element with reduced integration (C3D20R) is used for the mesh. The smallest element near the crack tip has the dimension 0.001 mm×0.005 mm×0.067 mm. A convergence study on element size has been conducted. Displacement control is used to apply a total deflection of 1 mm. A full Newton-Raphson algorithm is used to solve the geometric and material nonlinearity in an implicit method. The stress-strain relationship of the steel is characterized by eq. 4-3-3 and are reported in Table 4.7.

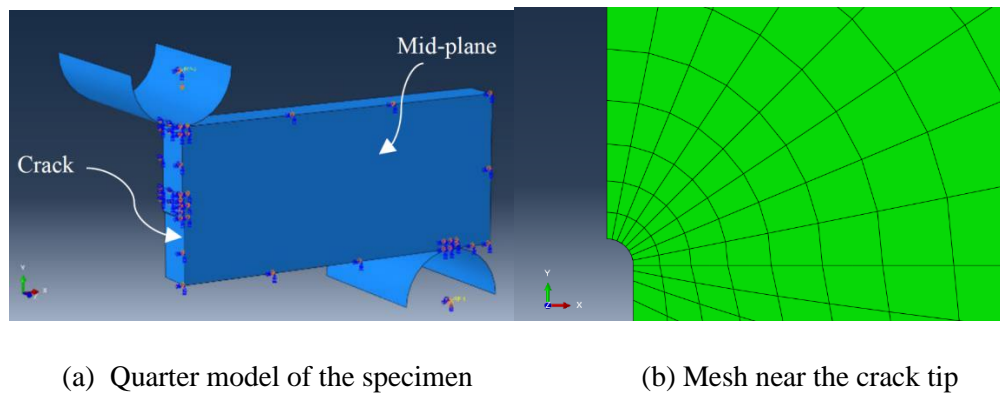(a) Quarter model of the specimen　　　　(b) Mesh near the crack tip

Fig 4. 11 Finite element model of the three-point bending test

In addition to yield properties, other parameters need to be predefined for cleavage modelling are $\varepsilon_{plastic,thre}$, V$_0$, and $\Delta \sigma_H^C$. The values of all the input parameters are summarized in Table 4.7.

Table 4.7 Value of the input parameters

Parameters	Values for Top	Values for Middle	Source
Young's modulus of matrix	219 GPa	236 GPa	Tensile tests
Yield stress (average value) σ_y	961 MPa	888 MPa	
Ludwik hardening parameter: K	489 MPa	593 MPa	
Ludwik hardening exponent: n_L	0.64	0.66	
Threshold plasticity strain $\varepsilon_{plastic,thre}$	10^{-5}	10^{-5}	/

Elementary volume V_0	0.001 mm^3	0.001 mm^3	[45]
Stress concentration factor of spherical inclusion f_α	0.239	0.239	[38]
Scatter of the inclusion fracture strength $\Delta \sigma_H^C$	0.10 GPa	0.10 GPa	/

4.4.2 Macroscopic homogeneous material

In the specimens taken from the top section of the plate, the statistical characteristics of particles and grains do not show spatial inhomogeneity. Due to the homogeneity, cleavage parameters K_{Ia}^{pm}, K_{Ia}^{mm} and σ_H^C can be determined by inverse analysis of the measured CTOD values on high and low constraint specimens.

Using the method described in Section 2, each combination of K_{Ia}^{pm}, K_{Ia}^{mm} and σ_H^C can generate a probability distribution of CTOD for two different constraint levels of specimens. Inverse modeling is performed by iteratively changing these three key parameters until the likelihood is maximized based on the cumulative distribution of all admissible CTOD values for both constraint conditions. The values of K_{Ia}^{pm} and K_{Ia}^{mm} characterize crack arrest by particle/matrix interface and by grain boundary, that may have similar effect on the macroscopic fracture toughness. Based on the microstructural features, the microcrack propagation in cleavage fracture can be either inclusion-size controlled or grain-size controlled [46][47]. The σ_H^C is related to the stress threshold of the cleavage, and is physically not correlated to K_{Ia}^{pm} and K_{Ia}^{mm}.

4.4.3 Material with macroscopic inhomogeneity

The specimens taken from the middle section of the steel plate contain CLs, which are inhomogeneous through thickness in terms of microstructure and mechanical properties. In section 3, it shows that the microstructures and yield properties differ between the CLs and areas outside CLs in the middle section specimens.

In this paper, simulation is performed on the middle section specimens with through-thickness crack (representing TL and LT orientation according to [44]). Fig 4. 12 shows the model of a middle section specimen. The white part is the material that does not contain CLs, and the green layers represent the CLs. The CLs are uniformly distributed over 8 mm across the thickness of the specimen. The thickness of the segregation bands and the spacing between them are 100 µm and 200 µm, respectively.
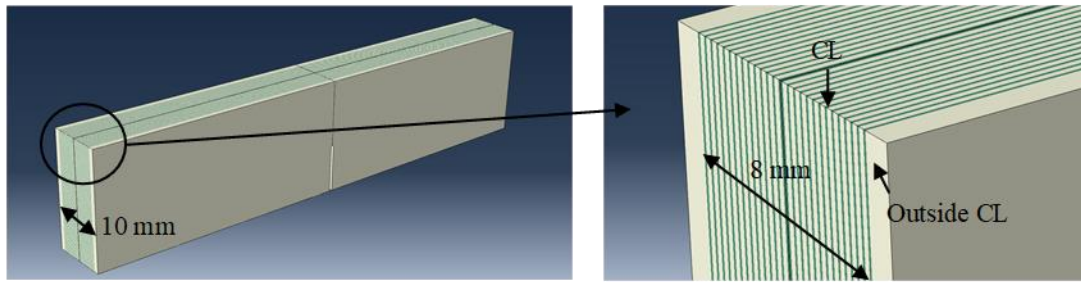
Fig 4. 12 Modelling of segregation bands as layers in the middle section specimen

In section 3, the characterization of materials suggests three possible distinctions of the segregation bands that can influence the cleavage behavior: the yield strength, the grain size, and the distribution (spatial, size and type) of inclusions. The yield strength difference influences the tensile stress distribution through the thickness, the grain size difference is related to probability of the crack propagation, and the inclusion difference can be reflected by cleavage parameters and inclusion density. While the yield strength difference and the grain size difference are determined explicitly from macroscopic and microscopic measurements, it is questionable whether the cleavage parameters within CLs can be transferred outside CLs, and whether the detrimental effect of brittle inclusions can be homogenized outside CLs. In order to investigate the possible difference in cleavage parameters and the effect on cleavage toughness, two approaches listed in Table 4.8 are compared within the proposed model.

Table 4.8 Approaches with varied considerations of CLs

Approach	Parameter different inside and outside of segregation band			
	Inclusion density	Grain size	Yield strength	K_{Ia}^{mm} and σ_H^C
Yield and grain size variation	No	Yes	Yes	No
Cleavage variation	Yes	Yes	Yes	Yes

A "Yield and grain size variation method" is firstly applied on the material. The yield strength and the grain size are considered as different inside and outside the CLs. The volume averaged yield strength of the specimen maintains the value as determined from tensile tests. The yield strength inside and outside the CLs is modified to the ratio calculated from nano-indentation measurements. As a result, yield strength inside CLs $\sigma_{y,CL} = 1.113\sigma_{y,tensile}$ and yield strength outside CLs $\sigma_{y,Out\ CL} = 0.944\sigma_{y,tensile}$. The same set of cleavage parameters (K_{Ia}^{mm}, σ_H^C) is assumed inside and outside CLs and is fitted from the measured CTOD values. Inclusions are assumed to be uniformly distributed in the middle section. The middle section specimens are assumed as a material that has different cleavage

parameters from the top section specimens and the cleavage parameters are homogeneous through the thickness.

In a "Cleavage variation method", the aggregation of Nb inclusions in the CLs is considered by assuming the cleavage parameters are different within and outside CLs, and the Nb inclusions are only distributed in the CLs. The yield strength, and the grain size are considered different inside and outside of the CLs, as in the "Yield and grain size variation method". In this approach, the segregation bands are considered as the main features that are different between the middle section specimens and the top section material. The material outside CLs is assumed to have the same value of cleavage parameters as at top section.

4.5. Results

4.5.1 Macroscopic homogeneous material

The cleavage parameters are fitted with maximum likelihood method from toughness data measured in two constraint conditions. A non-uniqueness situation occurs when the inverse modelling finds several combinations of K_{Ia}^{pm} and K_{Ia}^{mm} that can produce good fits. Fig 4. 13 shows several sets of K_{Ia}^{pm} and K_{Ia}^{mm} are found to generate the same CTOD distributions that fit the experiments of the reference steel, when inverse modelling is performed with "initial guess of parameters" varying in a wide range. The dashed line in Fig 4. 13 are formed by connecting the fitted [K_{Ia}^{pm} , K_{Ia}^{mm}] combinations.
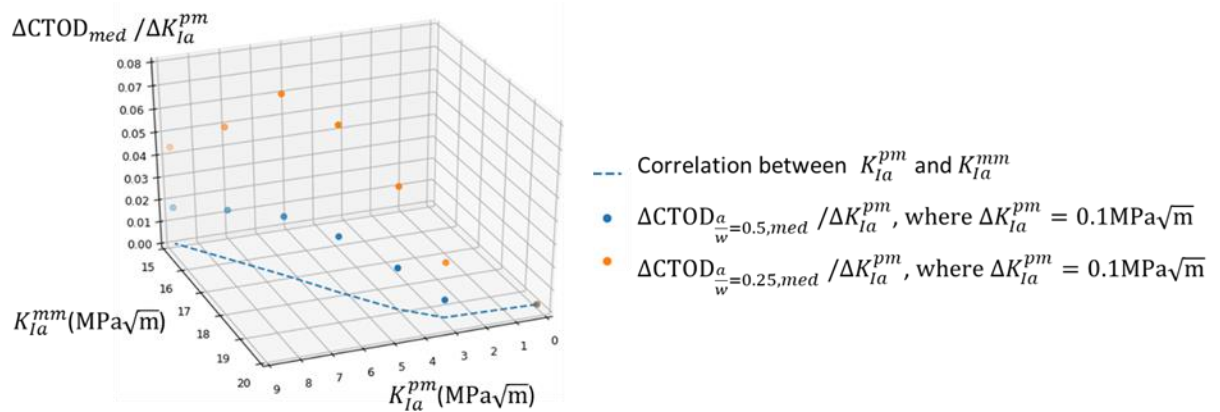

Fig 4. 13 Sensitivity of the median predicted CTOD value to K_{Ia}^{pm}

The non-uniqueness of K_{Ia}^{pm} and K_{Ia}^{mm} can be explained analytically. Both K_{Ia}^{pm} and K_{Ia}^{mm} relate local tensile stress $\sigma_{1,matrix}$ to a probability of microcrack propagation, via eq. 4-2-3, 4-2-4 respectively. The probability of a microcrack propagating across inclusion/grain interface and grain boundary is:

$$p = p_1(\text{inclusion size} > d_c) \times p_2(\text{grain size} > D_c) . \qquad 4\text{-}5\text{-}1$$

If $p_1 \ll 1$ and $p_2 \ll 1$, it means that both the inclusion/grain interface and the grain boundary act as the barrier to crack propagation. It is found that when $p_1 \ll 1$ and $p_2 \ll 1$, eqs. 4-3-1 and 4-3-2 can be characterized by power-law equations, and 5-1 can be written as

$$p = \frac{\alpha_1}{d_c^{\beta_1}} \times \frac{\alpha_2}{D_c^{\beta_2}} = \frac{\alpha_1}{\left(K^{pm}/\sigma_{1,matrix}\right)^{2\beta_1}} \times \frac{\alpha_2}{\left(K^{mm}/\sigma_{1,matrix}\right)^{2\beta_2}}. \qquad \text{4-5-2}$$

When eq. 4-5-2 holds, several sets of K_{Ia}^{pm} and K_{Ia}^{mm} result in the same value of p, and neither of the two parameters can be uniquely determined from the probability distribution of CTOD. However, an unique value of K_{Ia}^{pm} or K_{Ia}^{mm} can be determined by evaluating the sensitivity of the simulated toughness to the change in the fitted parameters.

Fig 4. 13 evaluates the sensitivity of the median value of the simulated CTOD (CTOD_{med}) to the change of K_{Ia}^{pm}. Seven points having values of K_{Ia}^{pm} and K_{Ia}^{mm} on the dashed line are evaluated. The change in CTOD_{med} (ΔCTOD_{med}) is calculated for a small change in K_{Ia}^{pm} ($\Delta K_{Ia}^{pm} = 0.1$ MPa$\sqrt{\text{m}}$) of each points. The sensitivity is expressed as $\Delta\text{CTOD}_{med}/\Delta K_{Ia}^{pm}$ and is plotted along the vertical axis in Fig 4. 13. It is found that, $\Delta\text{CTOD}_{med}/\Delta K_{Ia}^{pm}$ starts to increase when $K_{Ia}^{pm} > 3.0$ MPa$\sqrt{\text{m}}$. It is also found, when $K_{Ia}^{pm} > 3.0$ MPa$\sqrt{\text{m}}$, the dashed line coincides with eq. 4-5-2. It means $p_1 \ll 1$ and $p_2 \ll 1$ holds for $K_{Ia}^{pm} > 3.0$ MPa$\sqrt{\text{m}}$.

However, when $K_{Ia}^{pm} < 3.0$ MPa$\sqrt{\text{m}}$, it is shown that $\Delta\text{CTOD}_{med}/\Delta K_{Ia}^{pm}$ is close to zero, which means the simulated fracture toughness is not sensitive to the change of K_{Ia}^{pm}. It indicates p_1 cannot be approximated by a power law equation and eq. 4-5-2 does not hold when K_{Ia}^{pm} is low (< 3.0 MPa$\sqrt{\text{m}}$ for the reference material). In this case, inclusion/grain interface is not a barrier to crack propagation, and as the only controlling parameter, K_{Ia}^{mm} can be uniquely determined.

The threshold value of K_{Ia}^{pm} for the non-uniqueness depends on the microstructure of the steel. For the reference steel, FEA shows the $\sigma_{1,matrix}$ is around 2000 – 2500 MPa. The critical inclusion size corresponding to $K_{Ia}^{pm} = 3$ MPa$\sqrt{\text{m}}$ is 1.44 – 2.25 µm according to eq. 4-2-3. Fig 4. 7 shows that the brittle inclusions have a relatively large dimension compared to 1.44 – 2.25 µm, and the nucleated microcracks are in sizes that can automatically propagate into the neighbouring or parent grain if $K_{Ia}^{pm} < 3.0$ MPa$\sqrt{\text{m}}$.

Examination of fracture surfaces was performed using SEM to characterize the mode of failure and to locate and identify microstructural features that may have triggered cleavage [40]. Larger inclusions have been observed on the fracture surface, while Fig 4. 14 shows the smallest inclusions that are identified as local cleavage fracture initiation sites. The micro-cracks of the shown inclusion size are able to propagate across the inclusion/matrix interface and form cleavage facets among neighboring

grains. The inclusions are of sizes 1.22 (±0.08) µm and 1.27 (±0.10) µm respectively, below the value of 1.44 – 2.25 µm. It shows that in the reference steel, the K_{Ia}^{pm} should below 3.0 MPa√m, and the dominant barrier to micro-crack propagation is the grain boundary.
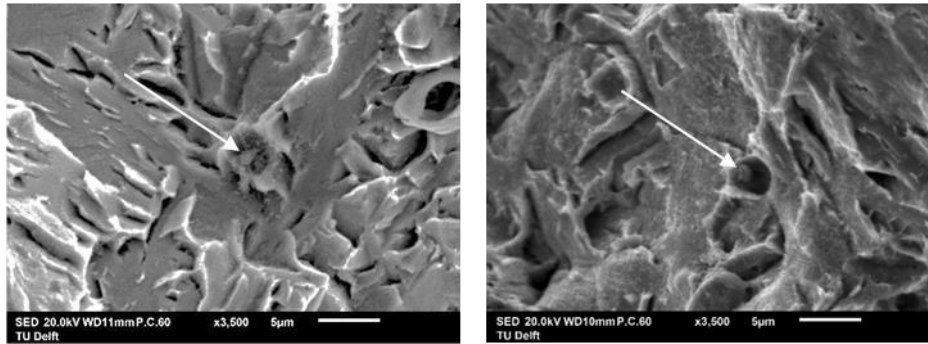
<table>
<tr><td>(a) High constraint, Top quarter</td><td>(b) Low constraint, Top quarter</td></tr>
</table>

Fig 4. 14 Inclusions (indicated by white arrows) acting as initiation site of the fractured specimens

Similar sensitivity studies were performed for all the other parameters. It was found that σ_H^C ranged from 1.00 GPa to 3.50 GPa is another controlling parameter independent of K_{Ia}^{pm} and K_{Ia}^{mm}, while $\varepsilon_{plastic,thre}$, V_0, and $\Delta\sigma_H^C$ show little impact with their predefined values in Table 4.7. Fig 4. 15 shows the sensitivity of the simulated CTOD to the values of K_{Ia}^{mm} and σ_H^C. While the simulated toughness monotonically increases with K_{Ia}^{mm}, it shows non-monotonicity for σ_H^C. Determination of σ_H^C with only one constraint condition may lead to non-uniqueness.
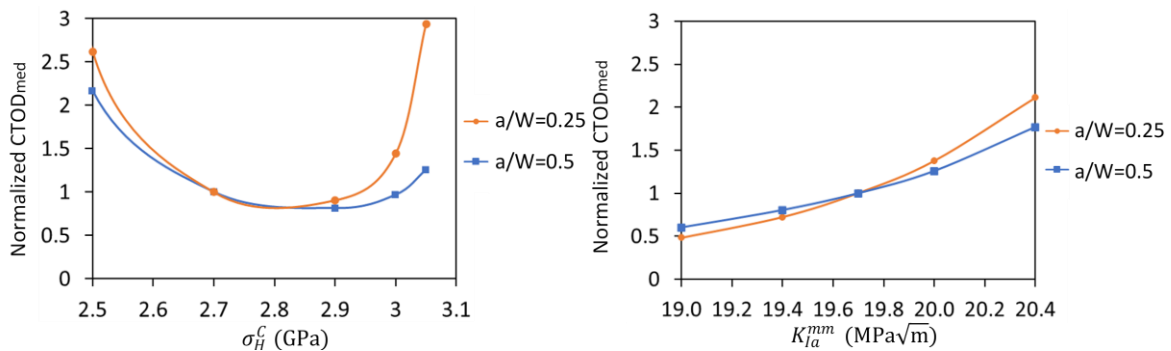
(a) Sensitivity to K_{Ia}^{mm} when $\sigma_H^C = 2.71$ GPa   (b) Sensitivity to σ_H^C when $K_{Ia}^{mm} = 19.7$ MPa√m

Fig 4. 15 Sensitivity of the simulated CTOD to cleavage parameters (present as the simulated CTOD corresponds to 50% fracture probability normalized by the ones simulated by the best-fit parameters)

With the recognition that the micro-crack propagation is grain-size controlled, the probability of inclusion-sized micro-crack propagation is set to be 1. Maximum likelihood fitting is performed with this modification, and the values of K_{Ia}^{mm} and σ_H^C are determined as $K_{Ia}^{mm} = 19.7 \text{ MPa}\sqrt{m}$ and $\sigma_H^C = 2.71 \text{ GPa}$. Fig 4. 16 shows the cleavage probability curve reproduced by the determined cleavage parameters for the top section specimens, which matches the experimental results well for high constraint specimens and low constraint specimens.
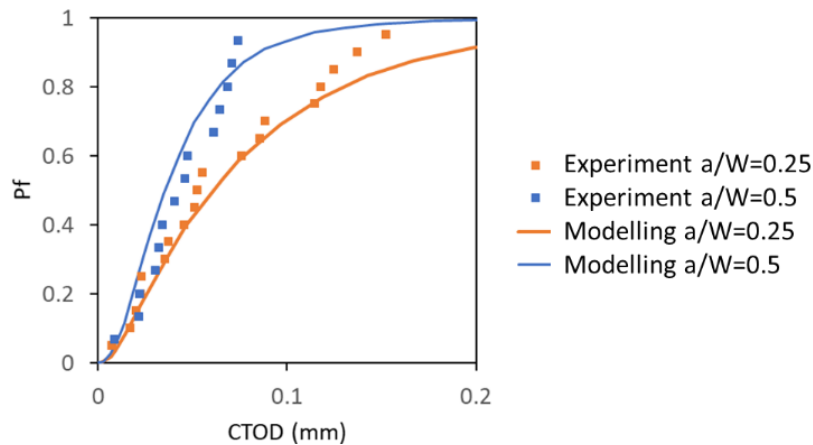

Fig 4. 16 Cleavage probability calculation of top section specimens based on fitted parameters

4.5.2 Material with macroscopic inhomogeneity

For "Yield and grain size variation method", the maximum likelihood fitting results in $K_{Ia}^{mm} = 20.0 \text{ MPa}\sqrt{m}$ and $\sigma_H^C = 2.03 \text{ GPa}$. For "Cleavage variation method", K_{Ia}^{mm} within CLs and σ_H^C of Nb inclusions are fitted with maximum likelihood fitting as $K_{Ia}^{mm} = 19.0 \text{ MPa}\sqrt{m}$ and $\sigma_H^C = 2.21 \text{ GPa}$. Table 4.9 summarized the value of cleavage parameters determined for both top and middle sections. Consequently, Fig 4. 17 shows the curves produced by the fitted parameters. The two approaches both extract cleavage parameters from maximum likelihood fitting and result in a similar level of fitting quality. However, the varying values of cleavage parameters indicate that the effect of segregation bands is differently represented in these two approaches, which will be further compared in section 5.3.

Table 4.9 Summary of cleavage parameters determined for both top and middle sections.

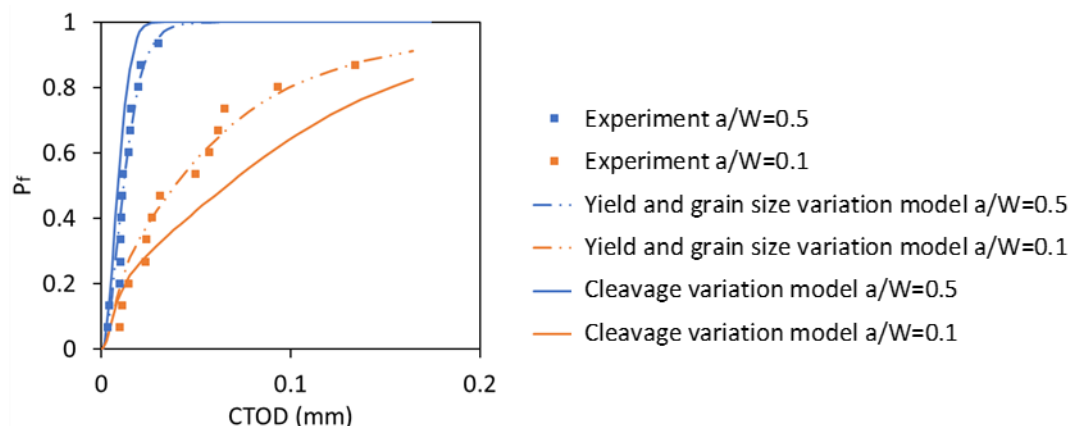| Parameters	Top	Middle (Cleavage variation method)		Middle (Yield and grain size variation method)
		CL	Out CL	
K_{Ia}^{mm}	19.7 MPa$\sqrt{m}$	19.0 MPa$\sqrt{m}$	19.7 MPa$\sqrt{m}$	20.0 MPa$\sqrt{m}$
σ_H^C with $\Delta \sigma_H^C = 100$ MPa	2.71 GPa	Nb inclusion 2.21 GPa	2.21 GPa	2.03 GPa
		Oxides 2.71 GPa	2.71 GPa	

Fig 4. 17 Cleavage probability calculation of middle section specimens and corresponding fitted parameter from "Cleavage variation method"

4.5.3 Effect of volume fraction, yield stress, and spacing of segregation bands on fracture toughness

To further evaluate the effect of segregation bands on cleavage toughness and to investigate the more physically-based approach of modelling the through thickness inhomogeneity, a sensitivity study is performed with the two methods proposed in section 4 on virtual materials assuming various volume fraction, yield strength, and spacing of CLs. The fitted K_{Ia}^{mm} and σ_H^C from "Yield and grain size variation method" and "Cleavage variation method" are used to predict the fracture probability.

(1) Volume fraction of CLs

CLs show two opposite effects on cleavage fracture. The finer grains prevent crack propagation across grain boundaries, while the stress concentration promotes inclusion cracking and micro-crack propagating. The ratio between volume of CLs (V_{CL}) and the total volume including CLs ($V_{\mathrm{CL}} + V_{\mathrm{OutCL}}$), is defined as the volume fraction of CLs $f_{CL} = \frac{V_{\mathrm{CL}}}{V_{\mathrm{CL}} + V_{\mathrm{OutCL}}}$. The reference analysis in section 4 corresponds to $f_{CL} = 1/3$. For a virtual material, assuming the properties inside CLs and outside CLs as same as for the reference analysis in section 4, an increased f_{CL} increases the local tensile stress but decreases the grain size. When the cleavage parameters are the same inside and outside CLs, the total effect on fracture toughness depends on the relationship between the yield stress and the grain size. If, in relation to the change of grain size, there is a more significant increase in yield stress, the existence of CLs is detrimental to toughness. Otherwise, the effect of finer grains is more pronounced and the CLs shows no detrimental influences.

Fig 4. 18 shows fracture toughness predicted by the "Yield and grain size variation method" is not sensitive to the volume fraction of CLs, which indicates that for the investigated material, the effects of higher yield stress and finer grain size inside the CLs approximately cancel each other.

However, with the "Cleavage variation method", the toughness is more sensitive to the existence of CLs. The tensile stress in the middle section would not be high enough to initiate crack in oxides. CLs contain Nb inclusions that have lower fracture strength and are more prone to cracking, and the toughness will be much decreased as the volume fraction of CLs increases.
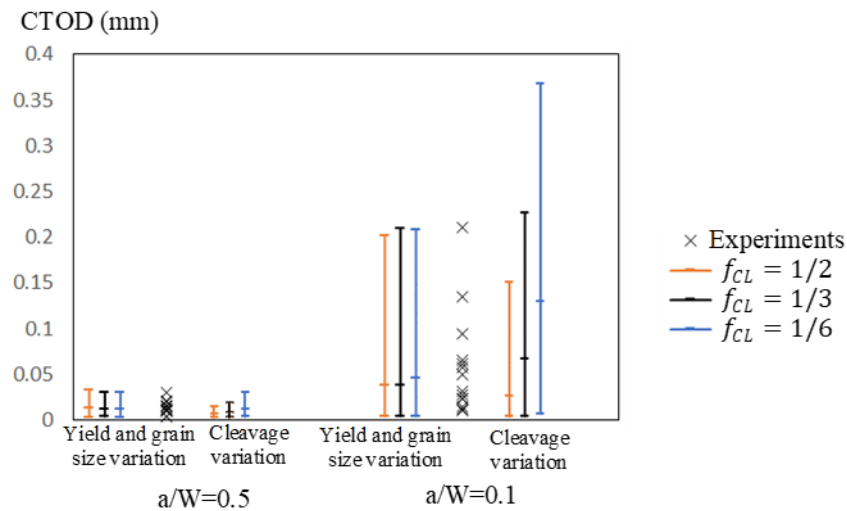

Fig 4. 18 Cleavage prediction of various $f_{CL} = \dfrac{V_{CL}}{V_{CL} + V_{OutCL}}$

(2) Yield stress of segregation bands

Hardness tests showed that the CLs have a higher yield stress. The ratio between the yield stress inside and outside CLs $f_{\sigma} = \sigma_{y,CL}/\sigma_{y,outCL}$ represents the stress concentration effect brought by the CLs. The reference analysis in section 4 has $f_{\sigma} = 1.18$. While the average yield stress remains constant, an increased ratio f_{σ} results in a higher stress inside the CLs, but a lower stress outside.
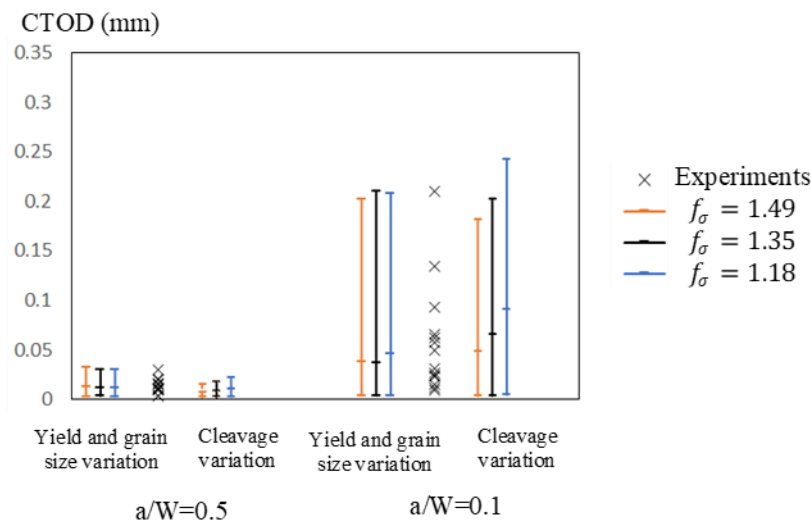
Fig 4. 19 Cleavage prediction of various $f_\sigma = \sigma_{y,CL}/\sigma_{y,outCL}$

Fig 4. 19 shows the sensitivity of the fracture toughness predicted by the two methods to the change of f_σ. For the "Yield and grain size variation method", the materials inside and outside CLs both contribute to the cleavage fracture. The increased stress inside CLs raises the fracture probability and the reduced stress outside CLs decrease the fracture probability. Consequently, little influence is reflected by varying the f_σ. For the "Cleavage variation method", the cleavage fracture is initiated by Nb inclusions distributed within CLs. The material outside CLs has little contribution. The increase of yield stress inside CLs leads to a lower level of fracture toughness, while the decrease of yield stress outside CLs has little effect. As a result, the fracture toughness predicted by the "Cleavage variation method" is reduced by a higher f_σ.

(3) Spacing of the segregation bands

In previous sections, the CLs are uniformly modelled over 8 mm across the thickness of the specimen, and the space among bands is 200 µm. Fig 4. 20 shows an extreme condition where the same volume of CLs is aggregated together instead of uniformly distributed, that the space among the modelled bands is zero. In Fig 4. 20, the CLs are located at the mid-plane. The aggregated bands increase the stress level in CLs by giving more constraint on the deformation. Meanwhile, the aggregated bands reduce the stress level outside the CLs, as the constraint of deformation is reduced.
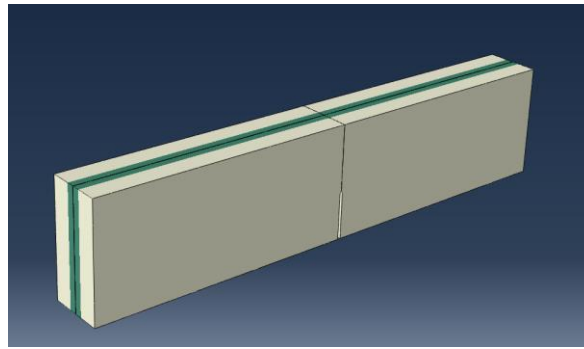
Fig 4. 20 Aggregated segregation bands (zero space between bands)

Fig 4. 21 shows CTOD predictions of the case in Fig 4. 20 based on "Yield and grain size variation method" and "Cleavage variation method". For the "Yield and grain size variation method", the aggregation of segregation bands leads to opposite effects on the predicted fracture toughness, and the fracture toughness is not sensitive to the change in band spacing and band location. For the "Cleavage variation method", the tensile stress within the CLs is dominant in the cleavage behaviour. The aggregated bands lead to a lower level of fracture toughness.
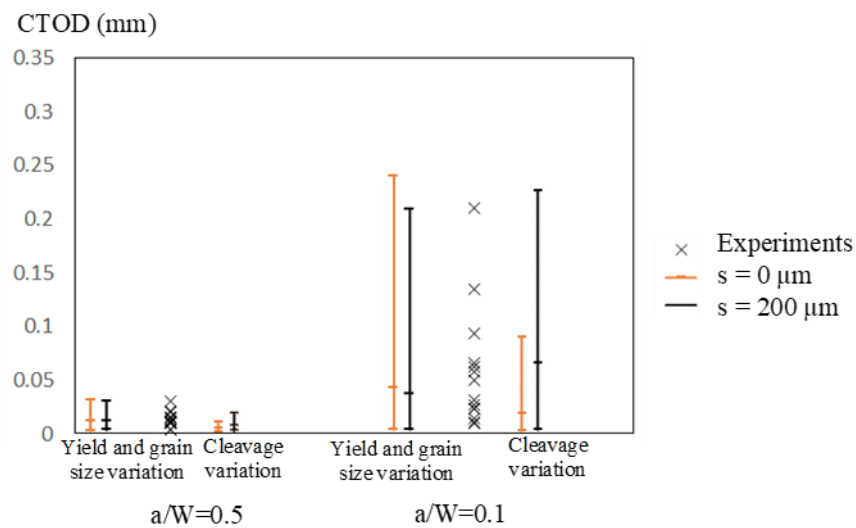

Fig 4. 21 Cleavage prediction of uniformly distributed (s= 200 µm) and aggregated (s = 0 µm) CLs

4.6. Discussion

The microstructural-informed statistical model presented in this paper is developed from multi-barrier theory of cleavage fracture, and it predicts the cleavage fracture toughness of steels from the microstructural information and tensile properties. The method has been applied on an 80 mm thick S690 QT steel plate, and the capability to characterize the scatter of the macroscopic fracture toughness

for deep and shallow cracked geometries is verified. The investigated material shows through thickness inhomogeneity and the model is able to reflect the microstructural changes on fracture toughness.

4.6.1 Determination of cleavage parameters

The model contains three cleavage parameters K_{Ia}^{pm}, K_{Ia}^{mm} and σ_H^C, that correspond to three critical events in the cleavage process. For each combination of the three cleavage parameters, the model predicts the fracture probability at a global load. The σ_H^C is related to the stress threshold of the cleavage, and is physically not correlated to K_{Ia}^{pm} and K_{Ia}^{mm}. The values of K_{Ia}^{pm} and K_{Ia}^{mm} characterize crack arrest by particle/matrix interface and by grain boundary, that may have similar effect on the macroscopic fracture toughness. When there is a distinct difference in the sensitivity of predicted toughness to the change of K_{Ia}^{pm} and K_{Ia}^{mm}, as for the sample steel in this paper, the controlling factor can be judged. In other cases, either microscopic measurements need to be performed, or another set of macroscopic measurements should be performed for a varied microstructure to determine the unique values of K_{Ia}^{pm} and K_{Ia}^{mm}. The cleavage parameters need to be determined by combinations of macroscopic mechanical testing and microstructural characterizations, and can be applied on toughness prediction in structural components where gradient changes of microstructures are expected (e.g. HAZ).

The current model calculates the fracture probability in the volume that has plastic deformation. This is based on the assumption that plasticity near hard particles is necessary to initiate cracks in them. For the investigated high strength steel, the fitted σ_H^C is higher than 2.00 GPa. The first principal stress of the material at local yielding is less than 1.70 GPa for deep cracked specimens, which supports the assumption. Analysis without the plastic strain criterion also shows there is little influence by applying a stress threshold, instead.

The initial crack tip is modelled as stress-free, while in reality there could be residual compressive stress from pre-fatigue. The maximum fatigue precracking load is determined according to [44], that $K_{I,max} = 25\ \mathrm{MPa\sqrt{m}}$. 96% of all the fractured specimens have $K_{I,c} > 50\ \mathrm{MPa\sqrt{m}}$, and the remaining two specimens have the lowest $K_{I,c} = 42\ \mathrm{MPa\sqrt{m}}$. Since the failure loads are much higher than the fatigue load, the effect of residual stress resulted from pre-fatigue on the cleavage initiation of the tested specimens can be assumed as minor.

Constraint conditions influence cleavage fracture due to the local state of tensile stress and the plastic deformation. In previous local approach models, such as Beremin method, Weibull stress is used to quantify the effect of local tensile stress and a threshold of Weibull stress has been proposed by [48, 49], to improve the agreement between high and low constraint conditions. In [17, 50], plastic strain based terms are used to correct Weibull stress to reflect the effect of plastic strain on particle cracking, which further improve the transferability of cleavage parameters among various geometries. In

comparison, the present model uses parameter K_{Ia}^{mm} to represent the effect of local tensile stress on crack propagation, and parameter σ_H^C to set a threshold of tensile stress. The effect of plastic deformation on particle cracking is reflected by eqs. 4-2-1, 4-2-2. The present model is applied on SENB specimens with different crack depths (a/W=0.1, 0.25, 0.5), and shows the ability to simulate toughness for both high and low constraint conditions. When represented by T-stress/nominal stress (as defined in [51]) the present geometries cover a range of [-0.46, 0.25], and when represented by stress triaxiality at the crack tip (as defined in [52]) the present geometries cover a range of [1.80, 2.33]. Both values are typical for cracked specimens. It is reasonable to assume the determined cleavage parameters can be transferrable to other geometries (such as pre-cracked CT specimens) where the fracture is pure cleavage. However, for uncracked geometries (such as round notched bars) that show interactions of cleavage and ductile failure due to lower constraint, the cleavage parameters will be varied.

4.6.2 Simulation of segregation bands

In this paper, two strategies of modelling CLs are compared. The main difference of the two methods is whether to assume the material containing CLs to have homogenous cleavage parameters, or assume the cleavage parameters inside CLs to be distinctive. Although the two methods both show satisfactory correlation with the experiments on S690 QT steel, they result in different reflection of the CLs on fracture toughness predicted for virtual materials. CLs have finer grains preventing crack propagation, and higher yield strength promoting inclusion cracking and micro-crack propagating. Clusters of Nb inclusions have been observed within the CLs as shown in Fig 4. 22 (a). Nb inclusions were also identified as a trigger in the cleavage fracture. Fig 4. 22 (b) and (c) show that a cubic Nb-rich inclusion large in size triggered the fracture process of a middle section specimen. From fracture surface analysis, initiation sites can be identified in nine of the middle section specimens, and seven of them have initiation sites identified as Nb inclusions.
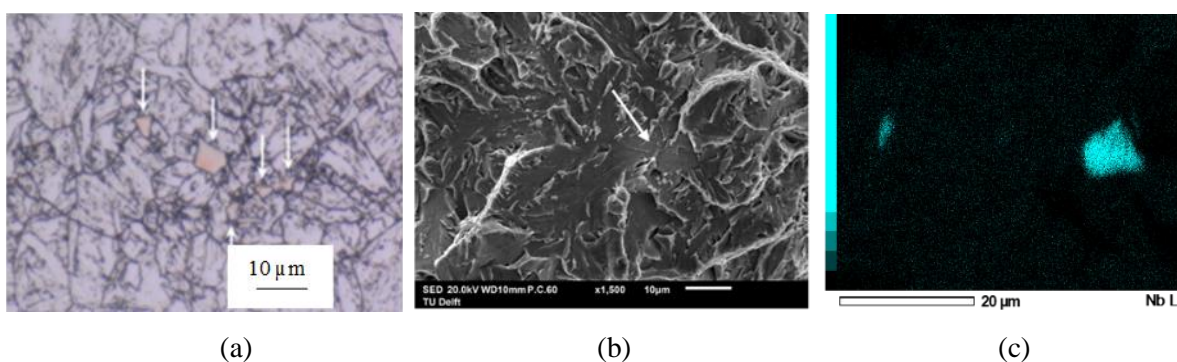

(a) (b) (c)

Fig 4. 22 Images showing (a) inclusions present in CLs (indicated by arrows) for the middle section (b) Nb-rich inclusion (indicated by white arrow) acting as cleavage initiation site (c) Nb maps of the inclusion at the fracture initiation site in (b) [40]

With the "Yield and grain size variation method", the effects of higher yield stress and finer grain size inside the CLs approximately cancel each other. The predicted fracture toughness is not sensitive to changes in CLs. In the case of "Cleavage variation method", the fracture toughness is predicted to be reduced for higher volume fraction of CLs, higher yield strength ratio of CLs, and aggregation of CLs. It proves that the detrimental effect of CLs is not only associated with grain structures and tensile properties, but strongly related to the microstructural toughness parameters, especially the cleavage strength of inclusions. As a comparison, in previous literature studying CLs [31], brittle TiN particles appears with similar frequency at the top and middle sections of a steel plate, and a profound refinement of the local grain size at the centreline is observed. The refinement of grain size compensates for the harder microstructure in CLs, and the heterogeneous material containing CLs does not show detrimental effect to toughness properties.

In the two methods, the value of fracture strength of inclusions σ_H^C cannot be transferred from middle section to the top quarter section, while the values of K_{Ia}^{mm} are relatively stable through the thickness. When microstructural cleavage parameters are assumed to be transferred from the centreline to outside the centreline, the detrimental effect of CLs is not properly reflected. It indicates that the cleavage parameter associated to a local brittle microstructure should not be homogenized outside the local brittle zone and a "Cleavage variation method" is required to better capture the influence of the local brittle zone on macroscopic toughness.

Bimodal local approach methods were applied to model the effect of inhomogeneities on fracture toughness [32-33], which assume the cleavage properties of local brittle zones can be represented by macroscopically homogeneous material at tens-of-millimeter scale. The Bimodal methods can successfully describe the statistical characteristics of a mixed data sets including several different materials, but are not able to relate the cleavage properties to microstructural features. Multi-barrier models that incorporate microstructural information are capable of capturing the micron-level features. However, such models were not applied to simulate CLs and rarely consider particle deactivations. For example, the same material studied in the present paper has been simulated in [38] with a multi-barrier method proposed by [36], without the modelling of CLs and the consideration of particle deactivations. The fitted parameters in [38] reflect similar conclusion as the "Yield and grain size variation method" used in the present paper, indicating a significantly lower cleavage stress of hard particles at the middle section, but did not provide insight into the specific effect of higher yield strength, finer grain size and brittle inclusions.

4.7. Conclusions

A microstructure-informed statistical method is proposed in this paper to model cleavage fracture in high strength steels containing through thickness inhomogeneities. The model is developed from a

multi-barrier theory with particular intention to include the effect of plastic strain and deactivation of hard inclusions. Examples of top quarter specimens and middle section specimens taken from the S690 QT steel plate fractured at -100 ℃ are used to validate the modelling method. Centreline segregation bands (CLs) appear in the middle section specimens, containing smaller grains and elongated inclusion clusters. In this paper, the statistical microstructural parameters and local yield properties of CLs are extracted from previous data in [40] and [41], and two modelling approaches are compared to discuss the effect of CLs in cleavage modelling. A sensitivity study has been performed to explore the influence of volume fractions, yield strength, and spacing of CLs. The following conclusions are highlighted for modelling cleavage fracture using the present model:

- Grain boundary rather than particle/matrix interface is identified as the barrier to microcrack propagation for the S690 QT, as the majority of hard inclusions are in size above micrometer.

- Existence of CLs has two opposite effects on cleavage fracture. The finer grains prevent crack propagation across grain boundaries, while the stress concentration promotes inclusion cracking and crack propagating.

- With "Yield and grain size variation method" the effects of 18% higher yield stress and 22% finer grain size inside the CLs approximately cancel each other. The predicted fracture toughness is therefore not sensitive to changes in CLs.

- In the case of "Cleavage variation method", the fracture stress of oxides is higher than the stress level outside CLs. The CLs of the sample steel contain Nb inclusions that have 19% lower fracture strength and characterize the cleavage behaviour.

- The "Cleavage variation method" shows that predicted fracture toughness is sensitive to the change of CLs. The toughness is predicted to be reduced for higher volume fraction, higher yield strength ratio, and aggregation of CLs.

The conclusions lead to a general suggestion that the cleavage parameter associated to a local brittle microstructure should not be homogenized outside the local brittle zone and a "Cleavage variation method" is required to better capture the influence of the local brittle zone on macroscopic toughness. The present methodology can quantitively capture the cooperating of complex microstructures in cleavage and can be used to facilitate the trade-off between various microstructural parameters in toughness control.

In addition, the present modelling approach has the following limitations that could be further investigated:

- The current model does not consider local variations of cleavage parameters at microscale. It does not account for cleavage parameters of ductile inclusions.

- The current model is verified for through thickness pre-fatigued crack, while surface crack and uncracked notch are not investigated in this paper.
- The current model does not include residual stress in CLs and around inclusions.

While the present paper focus on simulation method of through thickness inhomogeneities, a follow-up research is prepared to further investigate the transferability of cleavage parameters by applying the present method on different types of steels and specimen geometries. Another intended future research is to perform isoparametric changes of the microstructures by heat treatment to provide more quantitative comparisons from experiments.

4

References

[1] EN 1011, CEN (2009). Welding – Recommendations for welding of metallic materials.

[2] Miyata, T., Yang, R. C., Otsuka, A., Haze, T., & Ahira, S. (1989). Cleavage fracture of steels with fine grained ferrite, coarse grained bainitic and martensitic. Advances in fracture research Proceeding of the seventh international conference of fracture. 2563-2571.

[3] Lee, S., Kim, S., Hwang, B., Lee, B. S., & Lee, C. G. (2002). Effect of carbide distribution on the fracture toughness in the transition temperature region of an SA 508 steel. Acta Materialia, 50(19), 4755–4762.

[4] Zhou, M. W., & Yu, H. (2012). Effects of precipitates and inclusions on the fracture toughness of hot rolling X70 pipeline steel plates. International Journal of Minerals, Metallurgy and Materials, 19(9), 805–811.

[5] Li, X., Ma, X., Subramanian, S. V., Shang, C., & Misra, R. D. K. (2014). Influence of prior austenite grain size on martensite-austenite constituent and toughness in the heat affected zone of 700MPa high strength linepipe steel. Materials Science and Engineering A, 616, 141–147.

[6] Trampus, P. (2007). Micro structural aspects of unstable crack propagation in ferritic steels. Materials Science Forum, 537-538, 465-472.

[7] Curry, D. A., & Knott, J. F. (1978). Effects of microstructure on cleavage fracture stress in steel. Metal Science, 12(11), 511–514.

[8] Ray, A., Paul, S. K., & Jha, S. (1995). Effect of Inclusions and Microstructural Characteristics on the Mechanical Properties and Fracture Behavior of a High- Strength Low- Alloy Steel. Journal of Materials Engineering and Performance, 4(6), 679–688.

[9] Di Schino, A., & Guarnaschelli, C. (2010). Microstructure and Cleavage Resistance of High Strength Steels. Materials Science Forum, 638–642, 3188–3193.

[10] Armstrong, R. W. (2015). Material grain size and crack size influences on cleavage fracturing. Philosophical Transactions of the Royal Society A: Mathematical, Physical and Engineering Sciences, 373(2038), 20140474.

[11] Jia, T., Zhou, Y., Jia, X., & Wang, Z. (2017). Effects of Microstructure on CVN Impact Toughness in Thermomechanically Processed High Strength Microalloyed Steel. Metallurgical and Materials Transactions A: Physical Metallurgy and Materials Science, 48(2), 685–696.

[12] Pineau, A., Benzerga, A. A., & Pardoen, T. (2016). Failure of metals I: Brittle and ductile fracture. Acta Materialia, 107, 424–483.

4

[13] Beremin FM (1983). A local criterion for cleavage fracture of a nuclear pressure vessel steel. Metall Trans A, 14A, 2277–87.

[14] Wallin, K., Saario, T., & Törrönen, K. (1984). Statistical model for carbide induced brittle fracture in steel. Metal Science, 18(1), 13–16.

[15] Chen, J. H., Wang, G. Z., & Wang, H. J. (1996). A Statistical Model for Cleavage Fracture of Low Alloy Steel. Acta Metallurgica, 44(10), 3979–3989.

[16] Gao, X., Ruggieri, C., & Dodds, R. H. (1998). Calibration of Weibull stress parameters using fracture toughness data. International Journal of Fracture, 92(2), 175–200.

[17] Bernauer, G., Brocks, W., & Schmitt, W. (1999). Modifications of the Beremin model for cleavage fracture in the transition region of a ferritic steel. Engineering Fracture Mechanics, 64, 305–325.

[18] Bordet SR, Karstensen AD, Knowles DM, Wiesner CS (2005). A new statistical local criterion for cleavage fracture in structural steel. Part I: model presentation. Engineering Fracture Mechanics, 72, 435–452.

[19] Gao, X., Zhang, G., & Srivatsan, T. S. (2005). Prediction of cleavage fracture in ferritic steels: A modified Weibull stress model. Materials Science and Engineering A, 394(1–2), 210–219.

[20] Wallin, K., & Laukkanen, A. (2008). New developments of the Wallin, Saario, Törrönen cleavage fracture model. Engineering Fracture Mechanics, 75(11), 3367–3377.

[21] Shibanuma, K., Nemoto, Y., Hiraide, T., Suzuki, K., Sadamatsu, S., Adachi, Y., & Aihara, S. (2018). A strategy to predict the fracture toughness of steels with a banded ferrite–pearlite structure based on the micromechanics of brittle fracture initiation. Acta Materialia, 144, 386–399.

[22] Namegawa, T., Hoshino, M., Fujioka, M., & Minagawa, M. (2019). Effect of Carbon Content on Toughness of Tempered Martensitic Steels Analyzed by Toughness Prediction Model. ISIJ International, 59(7), 1337–1343.

[23] Kunigita, M., Aihara, S., Kawabata, T., Kasuya, T., Okazaki, Y., & Inomoto, M. (2020). Prediction of Charpy impact toughness of steel weld heat-affected zones by combined micromechanics and stochastic fracture model – Part I: Model presentation. Engineering Fracture Mechanics, 230, 106965.

4

[24] Mohseni, P., Solberg, J. K., Karlsen, M., Akselsen, O. M., & Østby, E. (2012). Investigation of mechanism of cleavage fracture initiation in intercritically coarse grained heat affected zone of HSLA steel. Materials Science and Technology, 28(11), 1261–1268.

[25] Keehan, E. (2004). Effect of Microstructure on Mechanical Properties of High Strength Steel Weld Metals, PhD thesis, Göteborg, Sweden.

[26] Tomita, Y. (1993). Improved fracture toughness of ultrahigh strength steel through control of non-metallic inclusions, J. Mater. Sci., 28, 853–859.

[27] Guo, F., Wang, X., Liu, W., Shang, C., Misra, R. D. K., Wang, H., Peng, C. (2018). The Influence of Centerline Segregation on the Mechanical Performance and Microstructure of X70 Pipeline Steel. Steel Research International, 89(12), 1800407.

[28] Echeverría, A. & Rodriguez-Ibabe, J. M. (1999). Brittle fracture micromechanisms in bainitic and martensitic microstructures in a C-Mn-B steel, Scr. Mater. 41, 131–136.

[29] Popovich V.A., Richardson I.M. (2015). Fracture Toughness of Welded Thick Section High Strength Steels and Influencing Factors. The Minerals, Metals & Materials Society (eds) TMS 2015 144th Annual Meeting & Exhibition, 1031-1038.

[30] Wallin, K., Yamamoto, M., & Ehrnstén, U. (2016) Location of initiation sites in fracture toughness testing specimen - the effect of size and side grooves, in: Proceedings ASME 2016 Press. Vessel. Pip. Conference, ASME, Vancouver, 1–9.

[31] Pallaspuro, S., Mehtonen, S., Kömi, J., Zhang, Z., & Porter, D. (2019). Materials Science & Engineering A Effects of local grain size and inclusions on the low-temperature toughness of low-carbon as-quenched martensite. Materials Science & Engineering A, 743, 611–622.

[32] Wallin, K., Nevasmaa, P., Laukkanen, A., & Planman, T. (2004). Master Curve analysis of inhomogeneous ferritic steels. Engineering Fracture Mechanics, 71(16–17), 2329–2346.

[33] Andrieu, A., Pineau, A., Besson, J., Ryckelynck, D., & Bouaziz, O. (2012). Bimodal Beremin-type model for brittle fracture of inhomogeneous ferritic steels : Theory and applications. Engineering Fracture Mechanics, 95, 84–101.

[34] Lin, T., Evans, A. G., & Ritchie, R. O. (1986). A Statistical Model of Brittle Fracture by Transgranular Cleavage. Mrch. Phys. Solids, 34(5), 477–497.

[35] Martín-Meizoso, A., Ocaña-Arizcorreta, I., Gil-Sevillano, J., & Fuentes-Pérez, M. (1994). Modelling cleavage fracture of bainitic steels. Acta Metallurgica Et Materialia, 42(6), 2057–2068.

4

[36] Lambert-Perlade, A., Gourgues, A. F., Besson, J., Sturel, T., & Pineau, A. (2004). Mechanisms and modeling of cleavage fracture in simulated heat-affected zone microstructures of a high-strength low alloy steel. Metallurgical and Materials Transactions A: Physical Metallurgy and Materials Science, 35(13), 1039–1053.

[37] Chen, J. H., & Cao, R. (2015). Micromechanism of Cleavage Fracture of Metals. Elsevier.

[38] Jiang, Q., Bertolo, V.M., Popovich, V.A., Sietsma, J., & Walters, C.L. (2021). Relating local stress on a hard microstructural inclusion from far-field stress on matrix to understand cleavage fracture in high strength steel. International Journal of Fracture, 232, 1–21.

[39] Griffith, A. A. (1921). The Phenomena of Rupture and Flow in Solids. Philosophical Transactions of the Royal Society A: Mathematical, Physical and Engineering Sciences, 221, 163–198.

[40] Bertolo, V. M., Jiang, Q., Walters, C.L., & Popovich, V.A. (2020). Effect of Microstructure on Cleavage Fracture of Thick-Section Quenched and Tempered S690 High-Strength Steel. In: Li J. et al. (eds) Characterization of Minerals, Metals, and Materials 2020, 155-168.

[41] Bertolo, V. M., Jiang, Q., Scholl, S., Petrov, R., Hangen, U., Walters, C.L., Sietsma, J., & Popovich, V.A. (2022). A Comprehensive Characterisation and Quantification of the Multiphase Microstructure of a Thick-Section High Strength Steel. Journal of Materials Science, 57, 7101–7126

[42] ISO 6892-3. (2015). Metallic materials - Tensile testing - Part 3: Method of test at low temperature.

[43] Dao, M., Chollacoop, N., Van Vliet, K. J., Venkatesh, T. A., & Suresh, S. (2001). Computational modeling of the forward and reverse problems in instrumented sharp indentation. Acta Materialia, 49(19), 3899–3918.

[44] ISO 12135. (2018). Metallic materials - Unifed method of test for the determination of quasistatic fracture toughness.

[45] Andrieu, A., Pineau, A., Besson, J., Ryckelynck, D. & Bouaziz, O. (2012). Beremin model: Methodology and application to the prediction of the Euro toughness data set. Engineering Fracture Mechanics. 95, 102-117

[46] Ray, A., Sivaprasad, S., & Chakrabarti, D. (2012). A Critical Grain Size Concept to Predict the Impact Transition Temperature of Ti-Microalloyed Steels. International Journal of Fracture, 173(2), 215–222.

4

[47] Ghosh, A., Ray, A., Chakrabarti, D., & Davis, C. L. (2013). Cleavage initiation in steel: Competition between large grains and large particles. Materials Science and Engineering A, 561, 126–135.

[48] Gao, X., & Dodds, R. H. (2000). Constraint effects on the ductile-to-brittle transition temperature of ferritic steels: a Weibull stress model. International Journal of Fracture, 102(1), 43–69.

[49] Rosahl, K., Booker, J. D., Lewis, S., & Smith, D. J. (2011). A statistical approach for transferring fracture events across different sample shapes. Engineering Fracture Mechanics, 78(1), 47–59.

[50] Ruggieri, C. (2020). A modified local approach including plastic strain effects to predict cleavage fracture toughness from subsize precracked Charpy specimens. Theoretical and Applied Fracture Mechanics, 105, 102421.

[51] Sherry, A. H., France, C. . C., & Gpldthorpe, M. R. (1995). Dimensional Cracked Geometries. Fatigue and Fracture of Engineering Materials and Structures, 18(1), 141–155.

[52] Hancock, J. W., & Mackenzie, A. C. (1976). On the mechanisms of ductile failure in high-strength steels subjected to multi-axial stress-states. Journal of the Mechanics and Physics of Solids, 24(2–3), 147–160.

4

4

5

Microstructure-based cleavage parameters in bainitic, martensitic, and ferritic steels

The contents of this chapter have been accepted as a journal paper by Engineering Fracture Mechanics (2023).

Abstract

Multi-barrier cleavage models consider the cleavage fracture with more than one microscale events. One of the challenges for multi-barrier cleavage models is the strong variations of cleavage parameters across different types of steels. The source of the variations has not been studied in a systematically. In the current paper, cleavage parameters corresponding to fracture initiation at a hard particle and crack propagation overcoming grain boundaries are estimated for three bainitic steels, a martensitic steel, and a ferritic steel, using a previously proposed model. It is found that the particle fracture parameter depends on particle morphology and composition, while the grain boundary cleavage parameter depends on the hierarchical grain structure. The determined cleavage parameters present a high degree of consistency among five different steels, which allows the further application on microstructure designs to control macroscopic toughness.

5.1. Introduction

Cleavage fracture shows strong sensitivity to material characteristics at the microstructural level, such as grain size [1], carbide size [2], hard inclusions [3], M-A (martensite-austenite) phases [4], precipitates [5], etc. The local approach to cleavage fracture is a class of physics-based statistical models that account for the probability of failure based on the local stress (and sometimes strain) field [6]. The Weibull formulation based on the weakest-link mechanism was first proposed by the Beremin group [7], Wallin et al. [8], and Lin et al. [9]. Many attempts [10-14] were made to represent the statistical

distribution of cleavage toughness based on the Weibull formulation. More recently, studies presented predictions of the toughness of steels from their microstructural information [15-17].

Among these models, effective surface energy γ_{eff} was proposed based on Griffith's criterion [18, 19] for simulating elastoplastic materials [20]. γ_{eff} is dependent on the local plastic behaviour of the matrix, and thus varies among different types of microstructures. There are two effective surface energy terms that are used: γ_{pm}, which represents the resistance of crack propagation from a brittle particle into the matrix; and γ_{mm}, which represents the resistance of crack propagation across a grain boundary [20]. The values of γ_{pm} and γ_{mm} have been reported from experimental estimations. Curry et al. [21] fitted γ_{pm} as 14 J/m^2 in a spheroidized ferrite/cementite steel. Bowen et al. [22] calculated γ_{pm} from the size of the carbide and the local fracture stress, and the resulting values vary in a range of 7-9 J/ m^2. Alexander et al. [23] calculated γ_{pm} to be 5-10 J/m^2 for pearlite eutectoid steel with a similar method. Linaza et al. estimated γ_{pm} for Ti bearing steels and Mn/B steels, and the resulting values vary in a range of 10-30 J/m^2 [24]. The value of γ_{mm} is more rarely determined and shows a wide variation in the values. Linaza calculated γ_{mm} to be 50-200 J/m^2 in [25]. A rapid increase of the estimated γ_{mm} from 50 J/m^2 at 173 K to 500 J/ m^2 at 223 K was reported by San Martin and Rodriguez-Ibabe [26]. Kawata et al. measured a range 25–100 J/m^2 of γ_{mm} for Ni-steels, depending on the temperature of measurement [27]. Li et al. measured the ratio γ_{mm}/γ_{pm} [28], and calculated γ_{mm} indirectly from γ_{pm}, which resulted in a range of 50–250 J/m^2.

A model based on multi-barrier theory was developed in [10, 15] for the prediction of cleavage fracture based on a statistical distribution of microstructural parameters and was recently improved through the incorporation of hard-particle deactivation in [29] for bainitic steels by the authors of this paper. The model is focused on inclusion cracking and the propagation of a microcrack through the first grain boundary. Cleavage parameters K_{Ia}^{mm} (crack arrest toughness of the grain boundary), and σ_H^C (fracture stress of hard inclusion) are fitted from fracture experiments. Previous analysis of a commercially available 80 mm thick S690 QT steel [29, 30] has been used to illustrate the modelling method and reveals the critically weak microstructural links in cleavage fracture. In the present paper, cleavage parameters of this model are determined for a commercially available 80 mm thick S690 QT steel (S690-A1) [29, 30], a variation of this commercial steel without Nb content (S690-A2), a commercial 100 mm thick S690 QT steel from a different provider (S690-B), a low-carbon martensitic steel [31], and a ferrite-cementite steel [32]. The variation of cleavage parameters is estimated and discussed considering thickness positions in S690 steel plate, chemical compositions, and process profile for the same 690 strength class, matrix types (bainite, martensite, ferrite), and hard particle types.

5.2. Materials and characterization

Three types of S690 quenched-tempered bainitic-martensitic steels (S690-A1, S690-A2, and S690-B), one martensitic steel, and one ferritic steel are studied in this paper. Table 5.1 shows the chemical composition of the five steels. The material S690-A1 is taken from a commercially available 80 mm thick steel plate. S690-A2 is a custom-made steel with the same nominal characteristics as S690-A1 but of a different chemical composition. Samples of S690-B are taken from another type of commercially available 100 mm thick steel plate. Materials of S690 steels are extracted from the top quarter section and the middle section of the plate. S690-A2 and S690-B are characterized and tested in this paper while S690-A1 has been characterized and tested in [30]. The martensitic steel and the ferritic steel have been characterized and tested by [31] and [32], respectively. All the steel plates were formed by hot-rolling.

Table 5.1 Chemical composition of steels in wt% (- stands for not detected)

Materials	C	Si	Mn	P	S	N	Al	Mo	Others*
S690-A1 [30]	0.17	0.29	1.29	0.009	< 0.002	0.005	0.067	0.304	Ni, Cr, Nb
S690-A2	0.17	0.25	1.01	0.012	<0.002	0.003	0.03	0.48	Ni, Cr, Ti
S690-B	0.097	0.07	0.94	0.006	0.004	<0.002	0.06	0.43	Ni, Cr, V, Cu
Martensitic [31]	0.124	0.20	1.08	0.007	0.002	0.005	0.03	0.155	Cr, Ti
Ferritic [32]	0.05	0.05	0.48	<0.002	0.0003	0.0014	0.01	-	-

*wt% is regarded as commercial confidential information and can be provided upon request.

5.2.1 Phases

Representative microstructures of the steels are shown in Fig 5.1 (micrographs of S690-A2 represent microstructures of the S690 steels). For the three types of S690 steel, both the top and middle sections of the plate have microstructures of 70-80% tempered bainite and 20-30% tempered martensite. The mid-thickness appears to have a higher fraction of tempered martensite and more pronounced segregation banding [30]. The microstructure of the martensitic steel is 90% auto-tempered lath-martensite and 10% untempered lath-martensite [31]. The ferritic steel has a ferrite–pearlite microstructure with coarsened cementite particles [32].
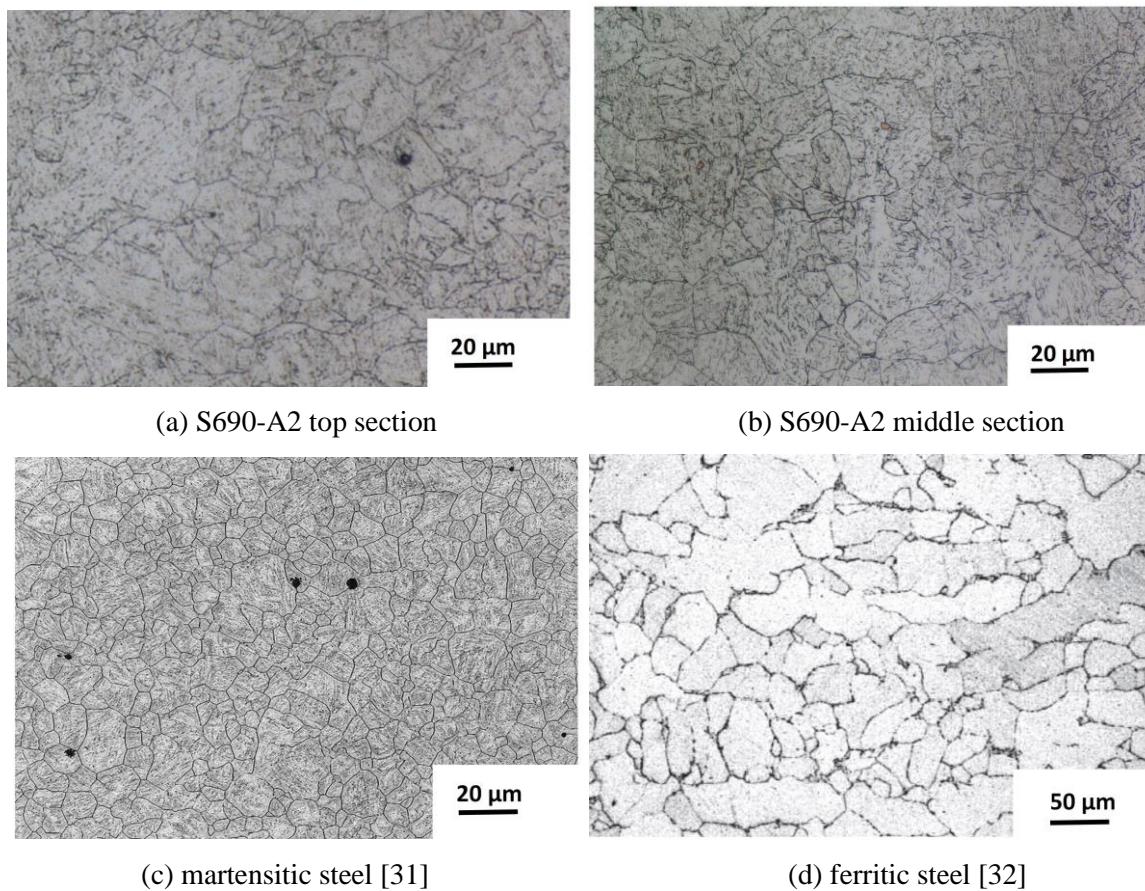
5

(a) S690-A2 top section

(b) S690-A2 middle section

(c) martensitic steel [31]

(d) ferritic steel [32]

Fig. 5.1 Micrographs of bainitic (S690), martensitic, and ferritic steels

5.2.2 Grain sizes

For lath microstructure such as bainite and martensite, "grains" show hierarchy structures, that ideally, individual Prior Austenite Grains (PAGs) are divided into four distinguishable packets that have the same Kurdjumov-Sachs (K-S) variant, and each packet is composed of three blocks of different Bain variants [33]. PAG size is used as the representative microstructural factor in the current analysis with the assumption that PAG size is linearly correlated to K-S packet size and to the possible cleavage facet size. For the bainitic steels and the martensitic steel, microstructural unit defined on the basis of the misorientation angle results in a large portion of ultra-small areas that do not act as cleavage facets. More discussions of the grain definitions are presented in Section 5.

For the three types of S690 steels, PAG, later referred as "grains", are reconstructed from Electron Backscatter Diffraction (EBSD) data in the top section and the middle section of the steel plate. EBSD data was acquired on a JEOL scanning electron microscope equipped with a Field Emission Gun (FEG-SEM) using 25 kV accelerating voltage, working distance of 25 mm, tilt angle of 70 °, and step size 0.2 μm; obtained by means of HKL Channel 5 software and post-processed with EDAX-TSL-OIM AnalysisTM software. The statistical distribution of grain size has been measured based on the major axis of PAGs, as the average aspect ratio (minor axis/major axis) is found to be 0.5 for the S690 steels.

To quantify the grain size (*D*) in cleavage modelling, least-square fitting is performed on the grain size data to get the function *P(D)* representing the probability of grains larger than *D*. *P(D)* is a combined function of lognormal distribution and power-law distribution, in order to accurately reflect the tails:

$$P(D) = \min\left\{1 - f(D, \mu, S), \frac{\alpha}{D^\beta}\right\} \qquad \text{5-2-1}$$

with $f(D, \mu, S)$ represents equation $1/2 + 1/2\text{erf}(\frac{\ln D - \mu}{\sqrt{2}\,S})$, where α and β are fitting parameters, μ is the mean and *S* is the standard deviation.

Fig. 5.2 shows the distribution function of each type of steel and the examples of the data measured in S690-A2 to indicate the goodness of fit. For all the S690 steels, the top sections have smaller grains and the middle section have slightly larger grains. For the martensitic steel, the PAG size was measured as equivalent circle diameter from etched micrographs, and eq. 5-2-1 is fitted to data published in [31]. For ferritic steel, there is no hierarchy grain structures and the grain boundaries are defined as boundaries where misorientation is larger than 5° measured by EBSD [32]. The ferrite grain size is defined as the equivalent circle diameter and eq. 5-2-1 is fitted to data published in [32]. Fig. 5.2 shows that of all the five steels the martensitic steel has the finest prior austenite grains, and the ferritic steel has the coarsest grains.
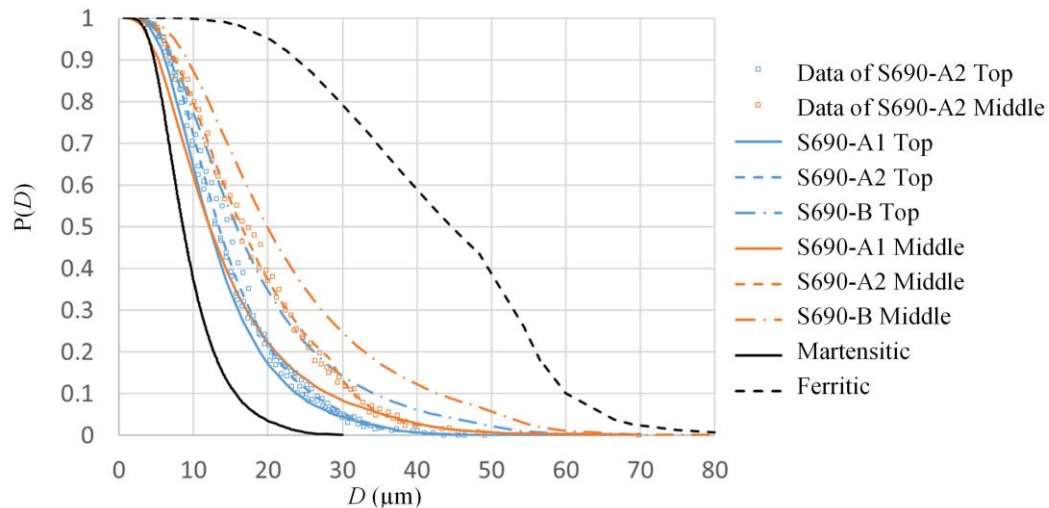

Fig. 5.2 Statistical distributions of the grain size obtained by fitting eq. 5-2-1 to experimental data, with examples of the data of S690-A2

5.2.3 Hard particles

Quantification of size of inclusions in S690 steels was performed by Keyence optical microscope. For S690-A1 and S690-A2, circular and square inclusions were observed in both top and middle sections. The size of circular inclusions is measured as equivalent diameter, while the square inclusions are represented by the longer axis. Fig. 5.3 shows the statistical distribution of particle size fitted by eq.

5-2-1 for the five steels. Volume density of inclusions is calculated from 2D measurement according to Schwartz-Saltykov method [34], and is listed in Table 5.2 for the S690 steels. Less circular and more square inclusions are present in S690-A2 steel than in S690-A1 steel. For square inclusions, the density in the middle section is higher, and the square inclusions tend to be larger compared to circular inclusions. S690-B steel contains smaller circular inclusions than the S690-A1 and S690-A2, and does not show square inclusions.

The inclusions in the martensitic steel can be divided into four groups based on the main element: aluminium, calcium, manganese, and titanium. Within these groups, there are nitrides, oxides, sulphides, and mixed types. The total number of mapped inclusions is 3651 in a 46 mm^2 area and 19.2% of the total inclusions are Ti-rich inclusions in square shape [31]. The circular shape inclusions and the square shape inclusions do not show difference in their size distributions. Compared with S690-A1 and S690-A2, the material has a higher frequency of smaller inclusions ($d < 2$ µm), which is similar to S690-B.

The hard particles that initiate cleavage in the ferritic steel are reported as cementite in [32]. The particle size was identified as a minor axis of an approximated ellipse because the crack was observed to generally occur in this direction [32]. The volume fraction of cementite was calculated from the carbon concentration, assuming cementite to contain 6.67% (wt) carbon. The shape of the particles is assumed as an oblate spheroid with the aspect ratio of 3.45 as reported in [32]. While S690 steels and martensitic steels have inclusions larger than 1 µm, cementite in the ferritic steel has sub-micro size.

Table 5.2 Inclusion number per 0.001 mm^3 (- stands for not detected)

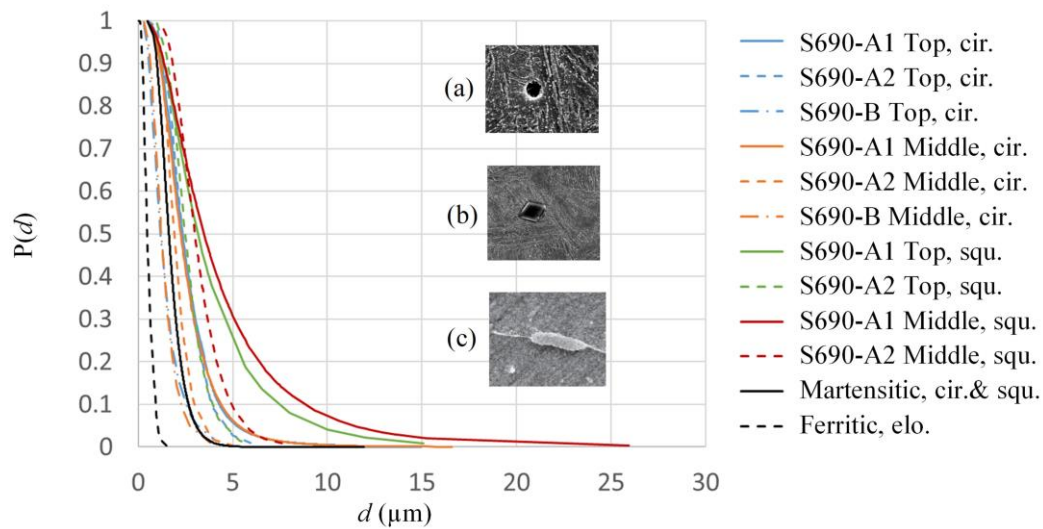| Inclusion types	S690-A1		S690-A2		S690-B	
	Top	Middle	Top	Middle	Top	Middle
circular inclusion	43.1	38.3	2.5	5.8	5.0	7.8
square inclusion	1.0	13.1	9.6	11.2	-	-

Fig. 5.3 Statistical distributions of the particle size obtained by fitting eq. 5-2-1 to experimental data, with figures showing the examples of (a) circular (cir.) inclusions, (b) square (squ.) inclusions, and (c) elongated (elo.) cementite

5.2.4 Tensile properties

The stress-strain relationship of the steels is characterized by Ludwik's law, which is defined with the flow stress (σ) and the effective plastic strain (ε_p) as:

$$\sigma = \sigma_y + K\varepsilon_p^{n_L}.$$

5-2-2

where σ_y is fitted yield stress, K and n_L are hardening parameters. For the steel S690-A2 yield point elongation is observed and in the strain range of elongation $\sigma = \sigma_{y,0.2}$ with $\sigma_{y,0.2}$ the 0.2% proof stress determined from the tensile curve. The parameters of Ludwik's law are fitted from tensile tests and are used to generate material input for the Finite Element Analysis (FEA).

Tensile tests of S690 steels were carried out at the temperature corresponding to the fracture tests (-100°C for S690-A1 and S690-A2, -130°C for S690-B) for top and middle specimens. The tensile tests of martensitic steel were performed at room temperature [31]. Since unstable necking occurs at a relatively low strain level, Digital Image Correlation data is used to generate the true-stress, true-stain curve after the maximum force. The fracture tests were performed at -60°C, -40 °C and -20°C. The true stress-strain curves at lower temperatures were derived from the tensile test at room temperature according to [35]. For the ferritic steel, tensile tests were conducted at -110°C, which is the same temperature as for the fracture tests [32]. The entire curve reported in [32] includes a tensile test until the maximum load and extrapolation after it. Eq. 5-2-2 is used to fit parameters for FEA based on the reported tensile curve. Fig. 5.4 shows the summary of fitting results.
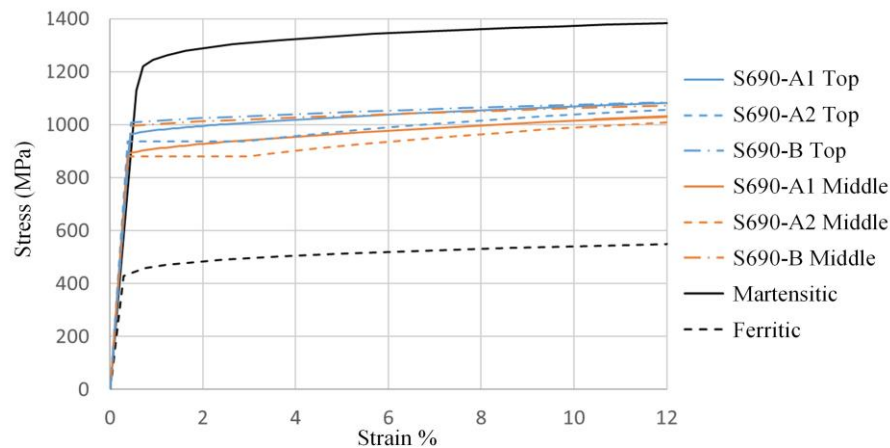
Fig. 5.4 True stress vs True strain curve of S690-A1 (at -100°C), S690-A2 (at -130°C), S690-B (at -130°C), martensitic steel (at room temperature), and ferritic steel (at -110°C) obtained by fitting eq. 5-2-2 to experimental data

5.3 Method of simulating cleavage fracture

This section outlines the method to model the cleavage probability of macroscale specimens, which are then used to determine the unknown cleavage parameters. Finite element analysis (FEA) of a macroscopic volume gives the result of stress/strain distribution under a certain global load level. The cleavage probability of each finite element is calculated as a function of stress level and will be evaluated based on the volume of finite element. The total failure probability of the specimen can be expressed as a function of the global load. Each combination of cleavage parameters K_{Ia}^{pm}, K_{Ia}^{mm} and σ_H^C can generate a probability distribution of CTOD of specimens. In this article, the unknown values of cleavage parameters are determined by inverse analysis based on the cumulative distribution of all admissible CTOD values.

5.3.1 Statistical model

The model applied in this paper is developed in [29] based on a multiple-barrier theory of the cleavage mechanism [10, 15]. Cleavage fracture of steels is regarded as the result of successive occurrence of three events:

I: nucleation of a slip-induced crack at a brittle second-phase particle or inclusion;

II: propagation of the microcrack across the particle/matrix interface;

III: propagation of the grain-sized crack to neighbouring grains across the grain boundary.

Inclusions and second phase particles are associated with the fracture initiation (event I). Under plastic flow, stress in a second phase particle is raised to a level to nucleate a microcrack. If the particle is brittle and deforms elastically during cracking, a single-parameter condition can be motivated for

crack nucleation, where a critical-strain-based model can be transformed into a critical-stress-based model [6]. The stress level needed for inclusion cleavage is characterized by particle strength σ_H^C. It is assumed that the value of inclusion strength is uniformly distributed in the range [σ_H^C, $\sigma_H^C + \Delta \sigma_H^C$]. For a volume that contains N inclusions, the number of cracked inclusions (N_{cr}) is in proportion to the stress σ_H at the inclusion, and can be calculated for $\sigma_H > \sigma_H^C$ as:

$$N_{cr} = \min\{N \times (\sigma_H - \sigma_H^C)/\Delta \sigma_H^C, N\}, \qquad \text{5-3-1}$$

where the stress σ_H at the inclusion is calculated from the first principal stress of the matrix $\sigma_{1,m}$ and the equivalent von Mises stress of the matrix $\sigma_{eq,m}$, by

$$\sigma_H = \sigma_{1,m} + f_\alpha \sigma_{eq,m}, \qquad \text{5-3-2}$$

where the factor f_α is determined using the analytical solution in [36] based on the inclusion geometry. In eq. 5-3-2, $\sigma_{eq,m}$ increases with plastic strain for a strain-hardening material, and f_α is always positive for an elastic inclusion. As a result, the calculated inclusion stress σ_H increases with plastic strain, and given eq. 5-3-1, the number of cracked particles also increases with plastic strain [36].

Phase boundaries and grain boundaries in ferritic steels offer important resistance to the propagation of cleavage cracks. When the cracks nucleated in particles encounter with the much tougher surrounding matrix material, the crack may instead of penetrating the surrounding matrix deflect into the interface (event II) [37]. When an advancing crack front meets a grain boundary, its propagation path can be deflected due to the large misorientation of cleavage planes (event III) [38]. A critical stress is usually used as a criterion for the crack propagation across the particle/matrix interface or across the grain boundary. In the present paper, the equivalent matrix toughness at the particle/matrix interface is characterized by the local cleavage parameter K_{Ia}^{pm}, and the equivalent toughness at the grain boundary is characterized by the local cleavage parameter K_{Ia}^{mm}. A minimum particle size (d_c) and a minimum grain size (D_c) are calculated for the first principal stress within the grain ($\sigma_{1,m}$) to propagate the micro-crack across the particle/matrix interface and grain boundary, respectively by:

$$d_c = (K_{Ia}^{pm}/\sigma_{1,m})^2 \qquad \text{5-3-3}$$

$$D_c = (K_{Ia}^{mm}/\sigma_{1,m})^2. \qquad \text{5-3-4}$$

The parameters K_{Ia}^{pm} and K_{Ia}^{mm} represent the equivalent effect of the boundaries, and eq. 5-3-3 and 5-3-4 do not assume the shape of the micro-crack.

Fig. 5.5 gives a flow chart of the computational model to calculate the cleavage probability of macroscale specimens. (FEA gives the stress/strain distribution (which contains $\sigma_{1,m}$, $\sigma_{eq,m}$, and ε_p values for each finite element). The cleavage probability is calculated from a cleavage check based on

the stress level, shape of the stress field, and statistical information of the microstructure. By accounting for the cleavage probability of all finite elements in the fracture process zone (areas that are plastically deforming), the total failure probability (P_f) of the specimen is calculated and expressed as a function of the global load. In addition to FEA stress and strain results, the required input includes f_α calculated from inclusion geometry, the distribution density function of the grain size $P(D)$, the distribution density function of the hard particle size $P(d)$, number of inclusions N per unit of volume, cleavage parameters K_{Ia}^{pm}, K_{Ia}^{mm} and σ_H^C. Other predefined parameters are threshold plastic strain $\varepsilon_{p,t}$, elementary volume V_0, and scatter of the inclusion fracture strength $\Delta \sigma_H^C$. All predefined values are summarized in Table 5.3.
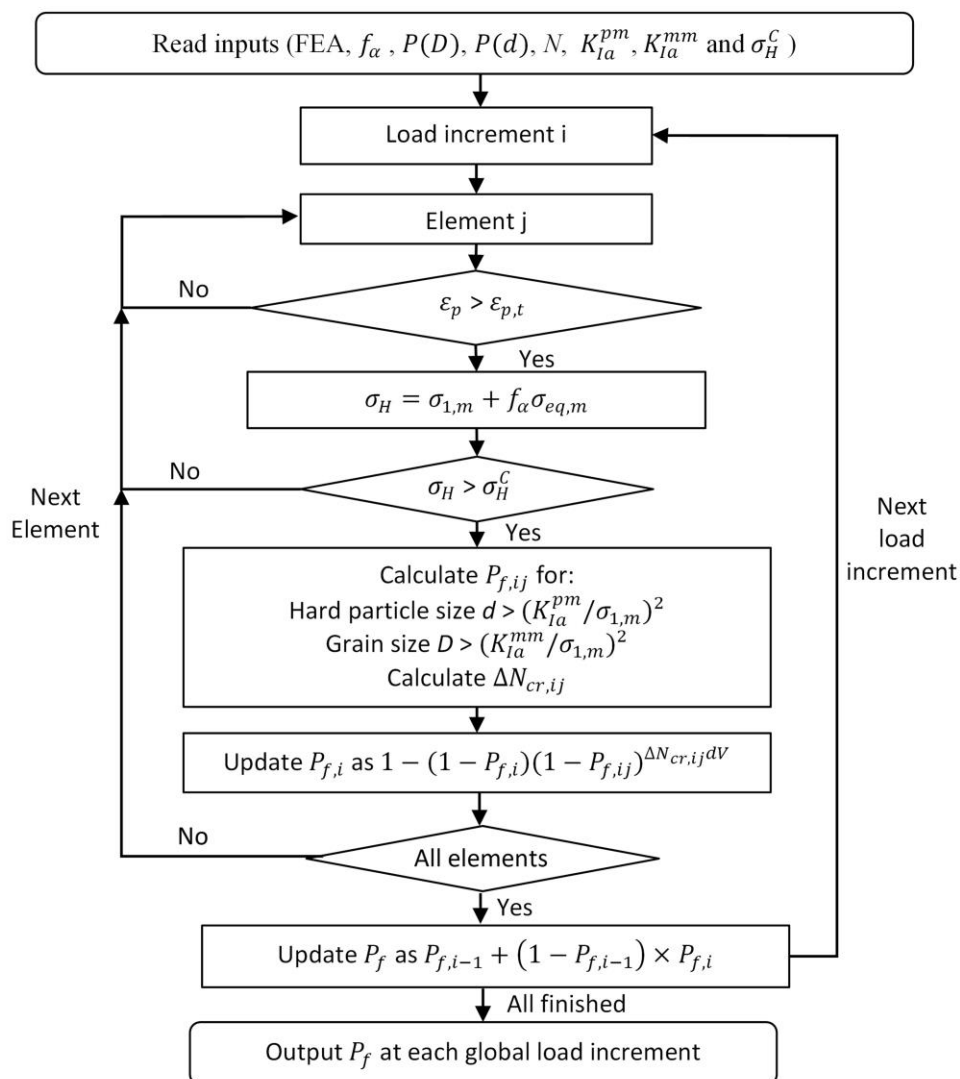

Fig. 5.5 Flow chart of the computational scheme [29]

Table 5.3 Values of the general input parameters for all types of steels

Parameters	Values	Reference
Threshold plasticity strain $\varepsilon_{p,t}$	10^{-5}	[6]
Elementary volume V_0	$0.001 \ mm^3$	[6]
Stress factor of inclusion f_α	1.495 for cementite, 0.239 for other inclusions	[36]
Scatter of the inclusion fracture strength $\Delta \ \sigma_H^C$	0.10 GPa	[29]

5.3.2 Finite element model of fracture toughness tests

Fracture tests of all types of steels were conducted on single-edge notched beam (SENB) specimens with static loading conditions, and toughness is measured as critical crack tip opening displacement (CTOD) [30-32]. The geometry of the specimen is shown in Fig. 5.6 and specified in Table 5.4 for each type of steel, together with the corresponding test temperatures.
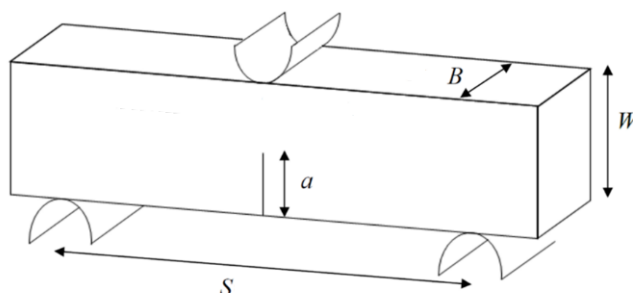

Fig. 5.6 Geometry layout of the SENB specimen

Table 5.4 Geometric information of specimens and test temperatures

Constraints	Geometry*	Crack length	Materials	Samples per condition	Temperatures
$a/W \geq 0.5$	1	10 mm	S690-A1	14 Top, 14 Middle	-100°C
			S690-A2	4 Top, 10 Middle	
			S690-B	6 Top, 9 Middle	-130°C
	1		Martensitic	8 at -20°C, 9 at -40°C, 8 at -60°C	-20, -40, -60°C
	2				
$a/W = 0.25$	1	5 mm	S690-A1	18 Top	-100°C
			S690-A2	4 Top, 10 Middle	-100°C
			S690-B	3 Top, 15 Middle	-130°C
$a/W = 0.1$	1	2 mm	S690-A1	13 Middle	-100°C
Unfatigued	3	7 mm	Ferritic	8	-110°C

*Geometry 1: $S = 80$ mm, $W = 20$ mm, $B = 10$ mm; Geometry 2: $S = 72$ mm, $W = 18$ mm, $B = 9$ mm.
Geometry 3: $S = 60$ mm, $W = 20$ mm, $B = 20$ mm.

SENB specimens are modelled in Abaqus 2017. For each analysis, a quarter of the specimen is modelled as a 3D deformable solid by using symmetry. The support and load roller are modelled as analytical rigid surfaces. The contact between rollers and the specimen is frictionless. Fig. 5.7 (a) mirrors the quarter of the specimen to show the 3D model of the pre-fatigued specimen and two rollers. Fig. 5.7 (b) shows the mesh near the crack tip for pre-fatigued specimens. The initial pre-fatigued crack is modelled as a finite notch that is 0.005 mm in tip radius. The smallest element near the crack tip has the dimension 0.001 mm×0.005 mm×0.067 mm. A convergence study on element size has been conducted. Fig. 5.7 (c) and Fig. 5.7 (d) show the 3D model and mesh near the crack tip for un-fatigued specimens of ferritic steel. A 20-noded hexahedral element with reduced integration (C3D20R) is used for the mesh. Displacement control is used to apply a total deflection of 1 mm. A full Newton-Raphson algorithm is used to solve the geometric and material nonlinearity in an implicit method.
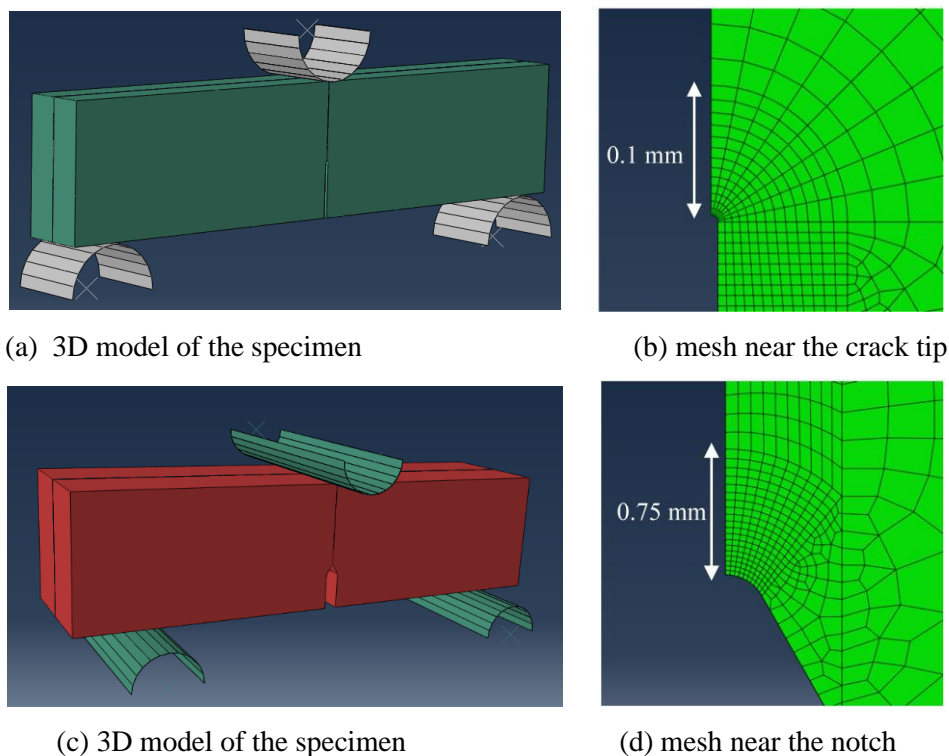

(a) 3D model of the specimen

(b) mesh near the crack tip

(c) 3D model of the specimen

(d) mesh near the notch

Fig. 5.7 Finite element model of the (a-b) prefatigued and (c-d) unfatigued three-point bending test

5.4. Results

5.4.1 Determination of cleavage parameters

Cleavage parameters K_{Ia}^{mm} (grain-boundary property) and σ_H^C (brittle-inclusion property) are determined by inverse analysis (maximum likelihood fitting) from the measured CTOD. The cleavage property of particle/interface, which is represented by K_{Ia}^{pm}, is provided by literature [31, 32] for martensitic steel and ferritic steel, respectively, and calculated from fracture surfaces analysis at the crack initiation sites for S690 steels.

Examination of fracture surfaces of S690-A1 was performed in our previous study using SEM to characterize the mode of failure and to locate and identify microstructural features that can triggered cleavage [39]. The smallest inclusions that are identified as local cleavage fracture initiation sites are of sizes 1.22 (±0.08) µm and 1.27 (±0.10) µm. The micro-cracks of such inclusion size are able to propagate across the inclusion/matrix interface and form cleavage facets among neighbouring grains. FEA shows that $\sigma_{1,m}$ is in the range of 2000 – 2500 MPa at the location of crack initiation sites. K_{Ia}^{pm} can be determined by eq. 5-3-3 with the identified particle size and stress state at the crack initiation site. The same analysis is performed for S690-A2 and S690-B. The value of K_{Ia}^{pm} is calculated as 2.5 MPa√m (with a standard deviation of 0.2 MPa√m) for S690 steels. For each type of S690 steel, the maximum likelihood fitting is performed on the data including deep cracked (*a/W*=0.5) and shallow cracked (*a/W*=0.1 or 0.25) pre-fatigued specimens taken from the top quarter section and the middle section. K_{Ia}^{mm} is separately fitted for top section and middle section, while σ_H^C of square inclusions and circular inclusions is fitted from the combined data of top and middle sections.

The surface energy for microcrack penetration across particle/matrix interface, γ$_{pm}$, is provided as 17 J/m^2 in [28] for the martensitic steel. Cleavage parameter K_{Ia}^{pm} are calculated by substituting the equation used in [28 & 31]:

$$\sigma_{fracture} = \sqrt{\frac{\pi E \gamma_{pm}}{(1-v^2)d_c}} \qquad \text{5-4-1}$$

where *E* is Young's modulus and v is Poisson's ratio, into $\sigma_{1,m}$ in eq. 5-3-3, and the resulting value is 3.5 MPa√m . Cleavage parameters K_{Ia}^{mm} and σ_H^C are fitted from combined CTOD data of three temperatures -60°C, -40°C and -20°C. The material's toughness K$_{Jc}$(1T) is less than 100 MPa√m at all three temperatures.

For the ferritic steel, fracture tests were conducted using un-fatigued SENB specimens with a notch of 0.25 mm root radius. The CTOD is calculated according to [32] as

$$\text{CTOD} = \frac{K^2(1-v^2)}{2\sigma_y E} + \frac{r_p(W-a)V_p}{(r_p(W-a)+a)} \qquad \text{5-4-2}$$

where r_p is the rotation factor (=0.4), *W* is specimen width, *a* is notch depth, V_p is a plastic component of the notch mouth opening displacement, which is measured by a clip-gauge, and *K* is the stress intensity factor calculated according to [35]. In [32], the surface energy for microcrack penetration across particle/matrix interface, γ$_{pm}$, is provided as 10 J/m^2. Cleavage parameter K_{Ia}^{pm} is calculated by substituting the equation

$$\sigma_{fracture} = \sqrt{\frac{4E\gamma_{pm}}{\pi(1-v^2)d_c}} \qquad \text{5-4-3}$$

used in [32] into $\sigma_{1,m}$ in eq. 5-3-3, and the resulting value is 1.7 MPa$\sqrt{\text{m}}$. Cleavage parameters K_{Ia}^{mm} and σ_H^C are fitted from the CTOD values measured at -110°C. Two out of nine specimens that failed with the ductile mode have been excluded from the present data points during fitting.

5.4.2 Summary of calculated cleavage parameters

A summary of the fitted values for cleavage parameters K_{Ia}^{mm} and σ_H^C is presented in Table 5.5. Fig. 5.8 shows the experiments and the simulations using the fitted parameters. The failure probability, P_f, of a specimen fractured in experiment, was calculated as a rank probability:
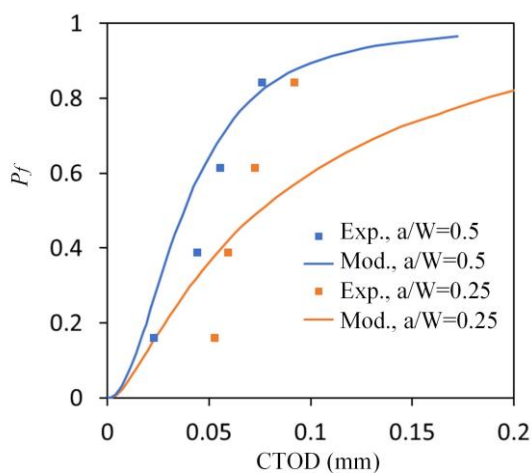
$$P_f = \frac{i-0.3}{N+0.4} \qquad \text{5-4-4}$$

where i is the rank number in terms of CTOD and N is the total number of experiments.
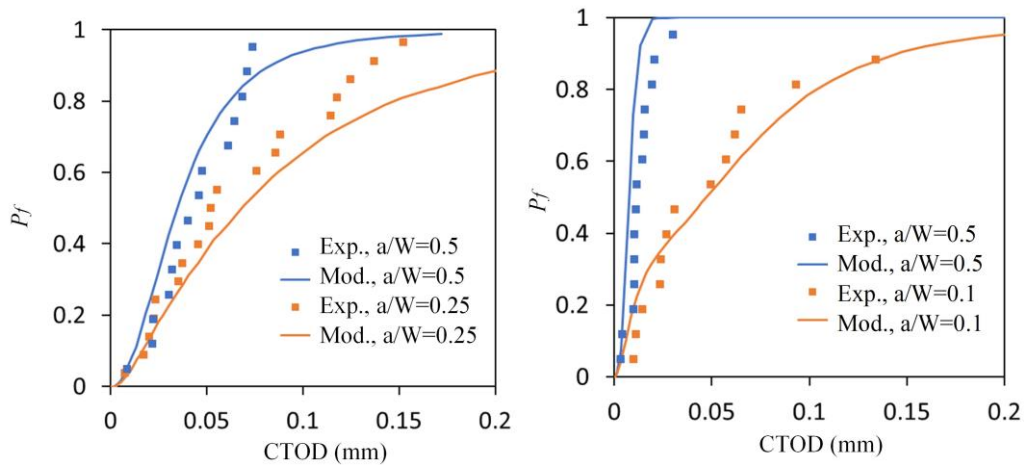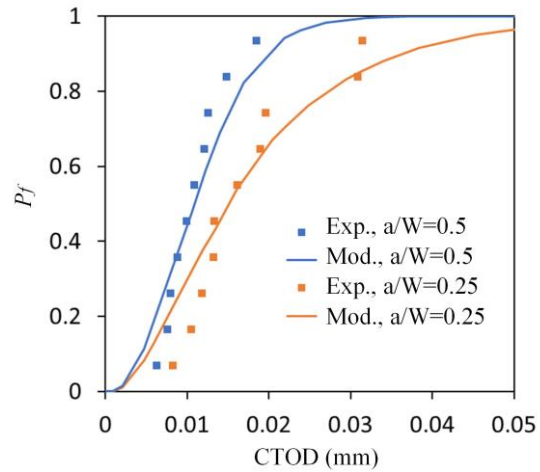

(a) S690-A1 top section (Exp. from [30]) (b) S690-A1 middle section (Exp. from [30])

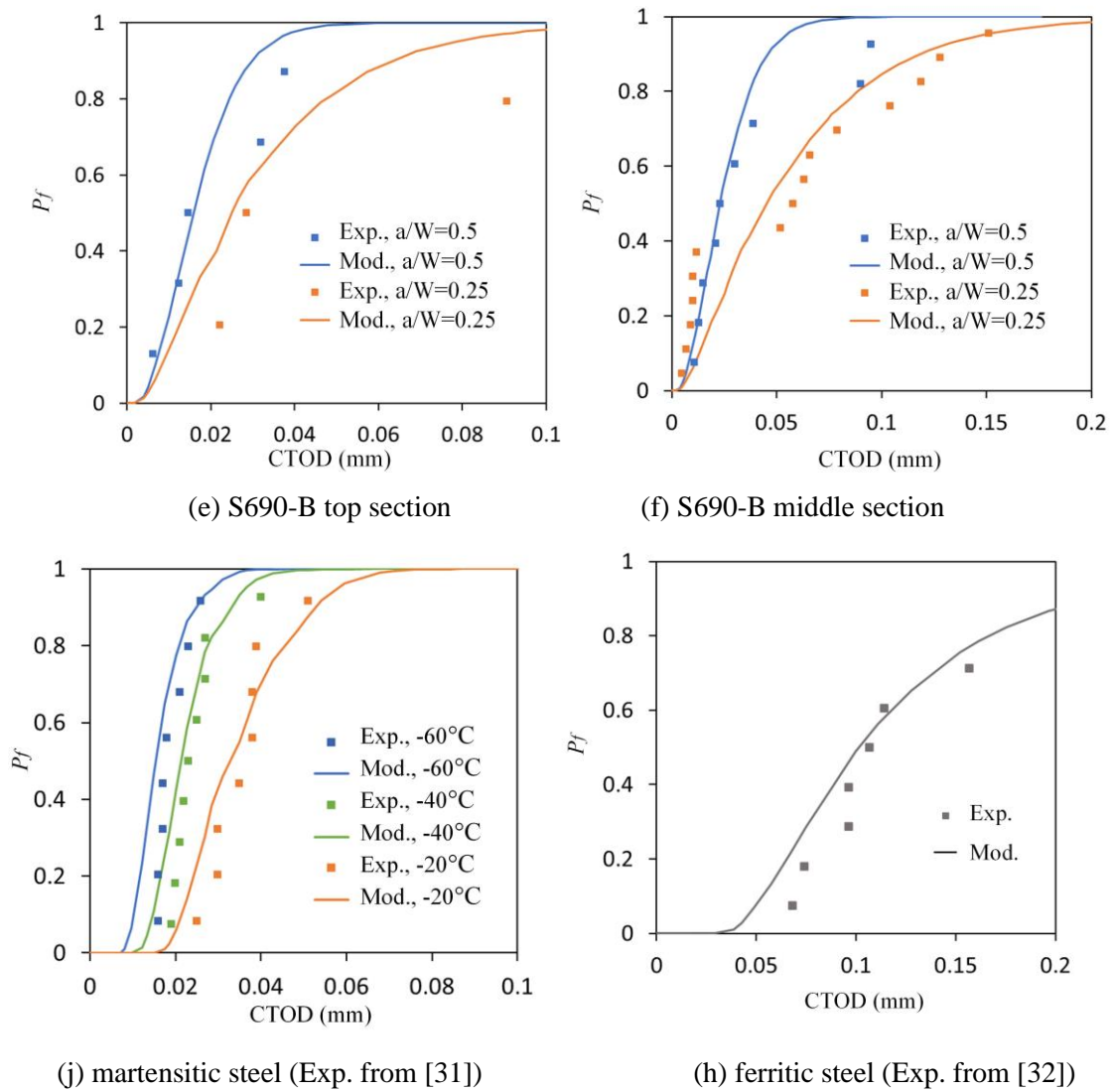(c) S690-A2 top section (d) S690-A2 middle section

(e) S690-B top section   (f) S690-B middle section

(j) martensitic steel (Exp. from [31])   (h) ferritic steel (Exp. from [32])

Fig. 5.8 Cleavage probability calculation based on fitted parameters (Exp. is experimental data and Mod. is modelled distribution)

Table 5.5 Summary of cleavage parameters determined for all materials (- stands for not detected)

Materials	K_{Ia}^{mm} (MPa$\sqrt{m}$)		σ_H^C (GPa) with $\Delta \sigma_H^C$ =0.1 GPa		
	top	middle	Circular	Square	Elongated
S690 –A1	19.7	19.5	2.7	2.2	-
S690 – A2	19.3	19.0	2.7	2.4	-
S690 - B	21.3	22.8	2.9	-	-
Martensitic steel	19.5		4.1	2.4	-
Ferritic steel	14.2		-	-	2.0

Sensitivity studies were performed in [29] for S690-A1. It was found that σ_H^C, K_{Ia}^{pm} and K_{Ia}^{mm} are controlling parameters while $\varepsilon_{p,t}$, V_0, and $\Delta \sigma_H^C$ have little impact with their predefined values in Table

5.3. Note that σ_H^C is the threshold stress for particle cracking, and with a scatter value $\Delta \sigma_H^C = 0.1$ GPa it also defines the maximum stress for particle cracking. For the bainitic and martensitic steels, the pre-fatigued specimen generates high local tensile stress (>2000 MPa) at low CTOD level (<0.01 mm), and during the fitting of σ_H^C and K_{Ia}^{mm} the gradient of simulated CTOD to σ_H^C becomes flat near its optimized value. An uncertainty of 7-10% in the fitted value of σ_H^C exists when one specimen geometry is used. To improve the accuracy of fitting, either two different *a/W* ratios or multiple temperatures are used to form the dataset of bainitic and martensitic steels. On the contrary, the unfatigued specimen of ferritic steel generates a local tensile stress that is gradually increased, and the gradient of simulated CTOD to σ_H^C remains sharp near its optimized value. The uncertainty of the fitted value of σ_H^C is within 2% when one geometry is used, and the dataset used in Fig. 5.8 (h) is sufficient to determine cleavage parameters for the studied ferritic steel.

The values of K_{Ia}^{mm} of the S690 steels are in the range of 19.0 to 21.7 MPa$\sqrt{m}$; the variation is within 15%. σ_H^C of circular inclusions of S690 steels are within 10% variation, ranging in 2.7-2.9 GPa. The cleavage parameter K_{Ia}^{mm} shows slight variation through the thickness of the plate. For S690-A1 and S690-A2, K_{Ia}^{mm} is larger for the top section than for the middle section, while for S690-B, K_{Ia}^{mm} is larger for the middle section than for the top section. σ_H^C value of square inclusions is 10% lower than of circular inclusions in the S690-A1 and S690-A2.

Comparing the S690 steels with the other two types of steel from literature, the martensitic steel shows a value of K_{Ia}^{mm} within 15% difference compared to S690 steels, while the ferrite-cementite steel shows a 30% lower K_{Ia}^{mm}. σ_H^C appears to vary largely. The circular inclusions in the martensitic steel show the largest value, 4.0 GPa, 50% higher than the value in the S690 steels. σ_H^C of cementite shows the lowest value 2.0 GPa, 10% lower than the value of square inclusions in the S690 steels.

5.5. Discussion

Lower σ_H^C of square inclusions of S690-A1 and S690-A2 are found compared to σ_H^C of circular inclusions, although they are of approximately the same magnitude. This indicates that brittle square inclusions are prone to cracking in both Nb-rich S690-A1 and Ti-rich S690-A2. σ_H^C of cementite shows the lowest value, even if the stress concentration due to larger aspect ratio is considered by the factor f_α. It may be due to the fact that the cementite particles are distributed with a high density and high local stresses may be generated locally in the region of particle clusters as demonstrated by [40], while the model assumes that there is no interaction among particles. The circular inclusions in the low-carbon martensitic steel show a 50% higher σ_H^C value than in the S690 steels. The higher stress threshold of particle cracking could be related to the more complex inclusions in the martensitic steel, which are prone to debonding from the matrix and would not have a tensile stress as high as calculated. However,

this significantly higher threshold may also be due to the temperature dependence of cleavage parameters, as the values of martensitic steel are fitted from fracture test at -60°C to -20°C, while the fitting of the other steels are at temperature not higher than -100 °C.

The cause of the variation in K_{Ia}^{mm} is possibly be related to sub-grain boundaries, such as packet and block boundaries. The model uses the size of PAG to represent the crack resistance of boundaries, while in S690 steels and the martensitic steel packets and blocks are present within PAGs. Fig. 5.9 shows the distribution of boundary misorientation angles for the top and middle section of the S690 steels, determined by EBSD. The S690 steels have narrowly varying K_{Ia}^{mm}, which can be explained by the narrow range of the misorientation angle of grain boundaries. There is a slight difference in the fraction of boundaries with 50-60° misorientation angle. The 50-60° misorientation angle corresponds to block boundaries and packet boundaries [30]. Increased fraction of high misorientation angle boundaries is associated with increased K_{Ia}^{mm} values. The low value of K_{Ia}^{mm} of the ferritic steel can similarly be explained by the lack of hierarchical grain structures. The ferrite grains are defined as grains with misorientation angle of 5° or more, and no packets or blocks are observed within the ferrite grains.
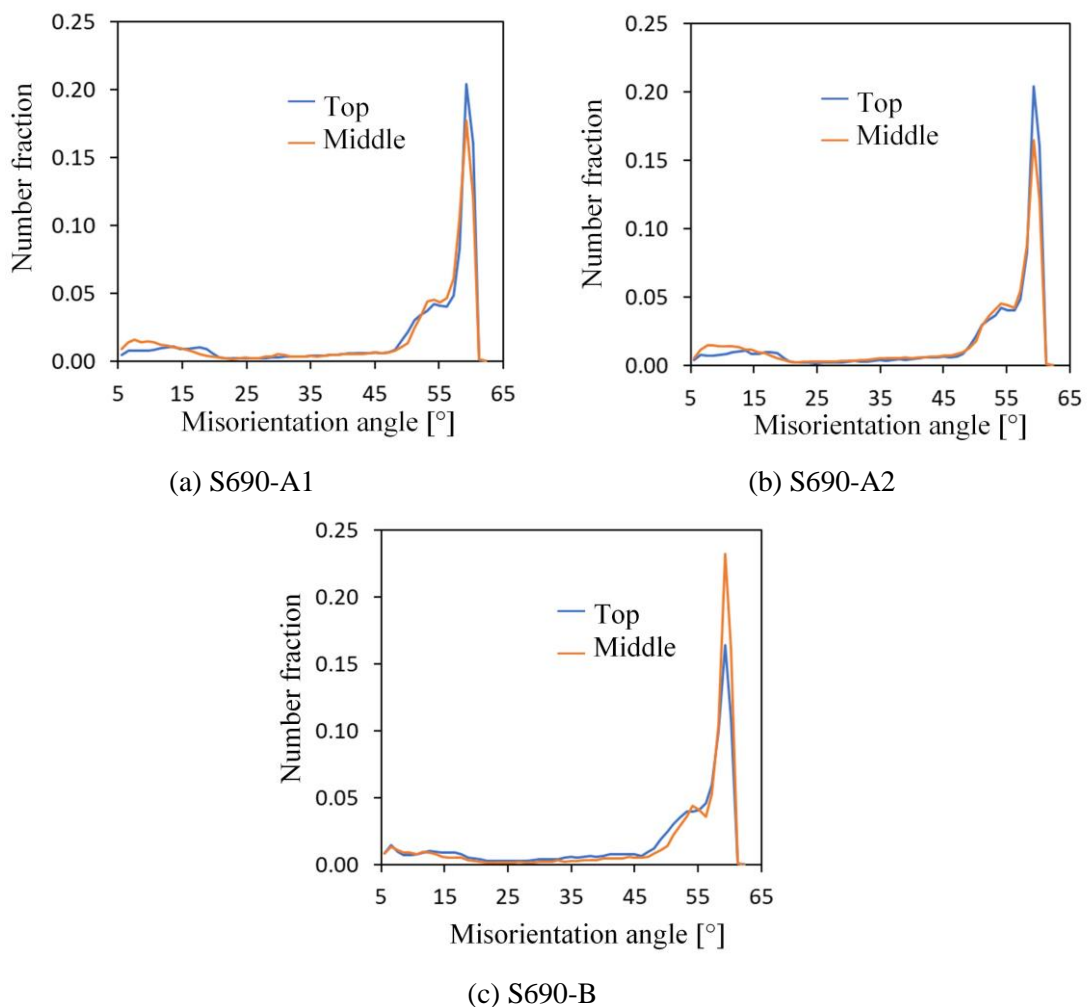

(a) S690-A1

(b) S690-A2

(c) S690-B

Fig. 5.9 Number fraction of boundary misorientation angles for S690 steels

The variation in K_{Ia}^{mm} leads to a discussion on whether the PAG or the grain defined by a misorientation angle should be used for modelling cleavage in bainitic and martensitic steels. Fig. 5.10 [39] shows a transverse section of the fracture path profile in S690-A1 and indicates that not all high misorientation boundaries show the ability to arrest cracks. For almost the entire analysed length (around 95%) of the fracture surface reported in [39], the cleavage crack propagates through the {100} and {110} planes in the top and middle sections, where both families of planes have a similar contribution. In both top and middle thickness positions, the crack deflects significantly from its path, or involve plastic deformation (revealed by a poor indexation in EBSD maps), where the neighbouring sub-structure divided by the PAG, packets, or block boundaries has a different Bain axis (for example, the locations indicated by black arrows in Fig. 5. 10 (b). According to this finding, the Bain zone is the effective crystallographic microstructural characteristic in deflecting the cleavage crack, which agrees with what was found by Wang et al. [41].
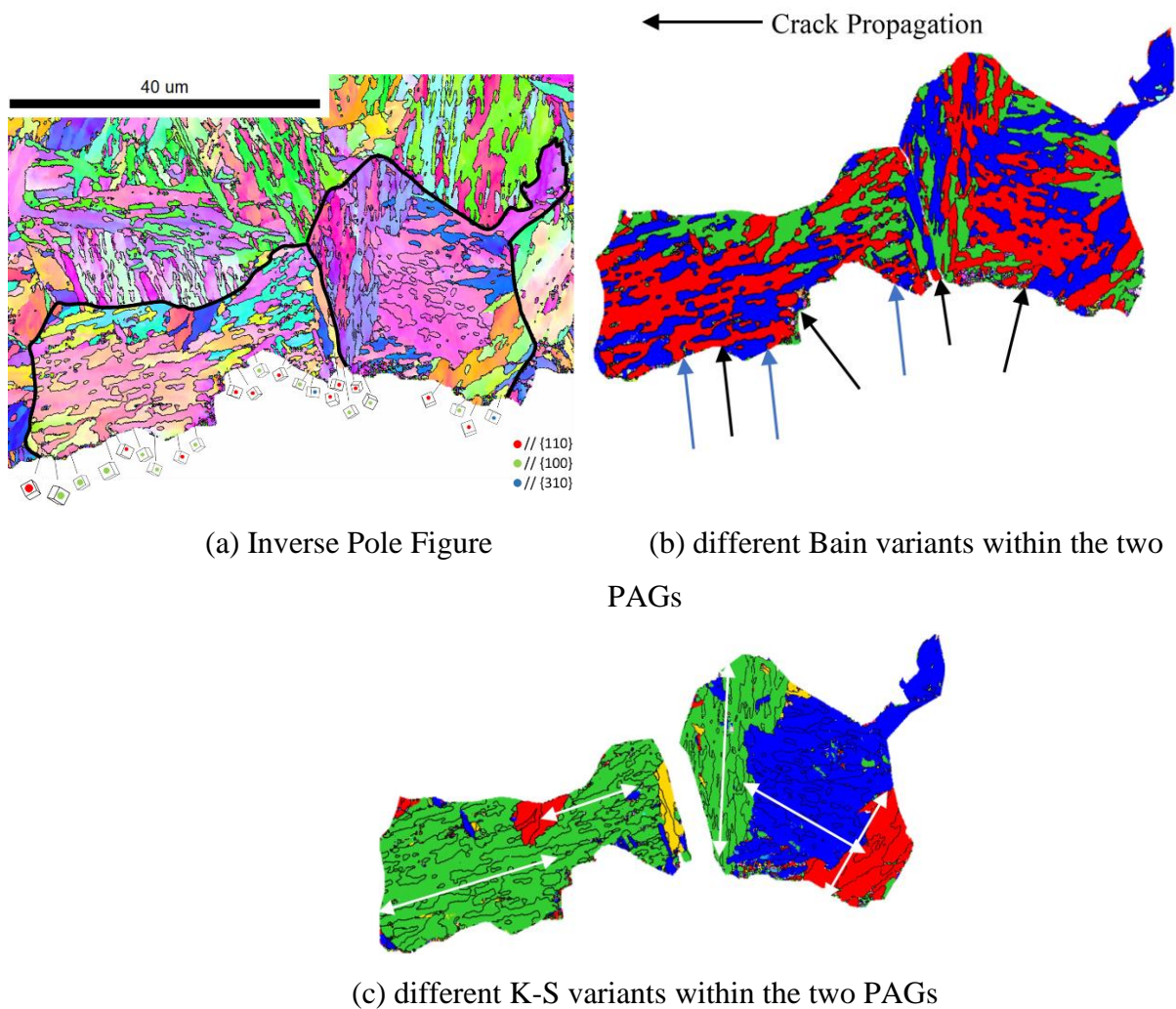

(a) Inverse Pole Figure

(b) different Bain variants within the two PAGs

(c) different K-S variants within the two PAGs

Fig. 5.10 Transverse fracture path profile in S690-A1 measured by EBSD [36] (Thin black lines are high-angle >15° grain boundaries and the thick black contour is the PAG boundary)

However, boundaries with different Bain axes that do not lead to deflections are also observed, as indicated by blue arrows in Fig. 5.10 (b). This can be attributed to the thickness of the Bain area, as observed by Wang et al. [41]. The observation in fracture path profile leads to a difficult determination of the effective size of the Bain area. Fig. 5.10 (c) shows the K-S variants of the same grains in (a) and (b), with white arrows indicating the approximate length of the large Bain area that can act as an initiation facet if cleavage occurs at the shown plane. Under the assumption that the PAG size is linearly correlated to the K-S packet size and to the possible cleavage facet size, the PAG size represents the microstructural unit, and the corresponding K_{Ia}^{mm} represents the crack resistance of all boundaries within a PAG.

Defining the Bain unit on the basis of the misorientation angle results in a large portion of ultra-small areas that do not act as cleavage facets, which will underestimate the value of K_{Ia}^{mm}. Fig. 5.11 shows the comparison of the size distribution of PAGs and of bainite grains defined by a misorientation angle of 15° or higher, for the same EBSD scan in the middle section of S690-A2. More than 50% of grains defined by a misorientation angle of 15° have major axis length lower than 2 µm. The 15° definition of grain boundary leads to a fitted $K_{Ia}^{mm} = 11.3$ MPa$\sqrt{\text{m}}$, which is even 20% lower than the fitted value of the ferritic steel (where ferrite grains are defined by a misorientation angle of 5°).
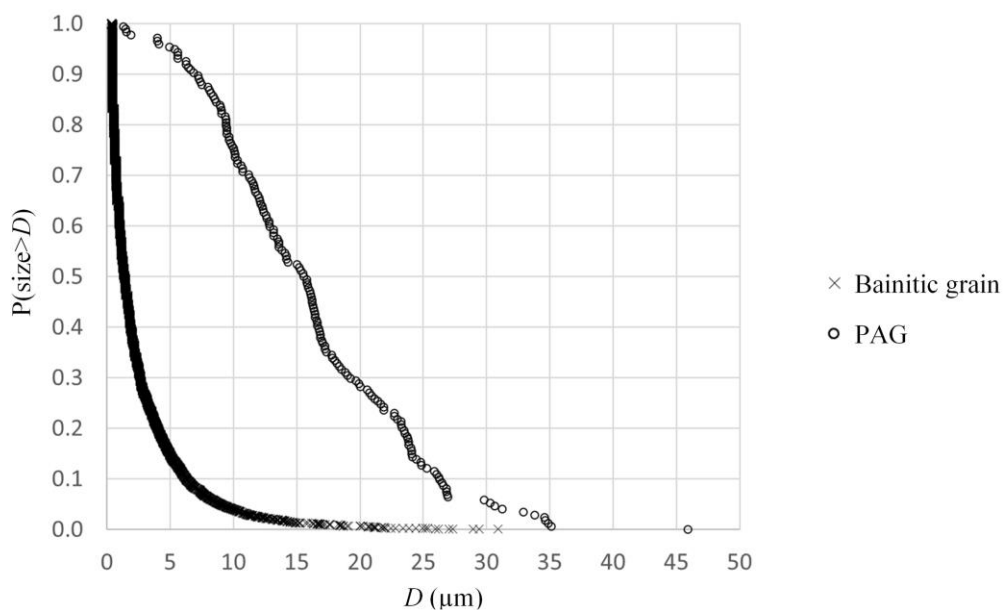

Fig. 5.11 Size distribution of PAG and of bainite grain defined by 15° misorientation for the microstructure of S690-A2

Among the methods of cleavage modelling proposed in literature, Beremin parameters (σ_u and m) [7] and surface energy parameters (γ_{pm} and γ_{mm}) [20] are most frequently used to represent material's fracture property at continuum-level and micro-level, respectively. Beremin parameters reflect the total effect of geometry of microstructures (e.g., microcrack size distribution, microcrack density) and

toughness of microstructures (e.g., resistance of boundaries, cracking criterion of particles). Any changes in the microstructure will affect the Beremin parameters. Fig. 5.12 shows the normalized (divided by the mean) cleavage parameters (K_{Ia}^{mm} and σ_H^C) presented in Table 5.5 and Beremin parameters (σ_u and m) determined for the same S690 steels by the method proposed in [42]. (Martensitic steel and ferritic steel are not used for determining Beremin parameters as the method requires a combined dataset of small-scale-yielding and large-scall-yielding.) The material parameters σ_u and m determined by the Beremin method vary in a range of 50% - 230% around the mean. Similar findings of the wide variation of Beremin parameters are reported in [13]. In comparison, the current method uses geometry information of microstructures as input, and the determined parameters solely represent effective resistance to fracture for the defined microstructures. Consequently, the cleavage parameters will not be influenced when grain size or particle size are changed, as long as the phases are the same. Fig. 5.12 shows that the values of K_{Ia}^{mm} and σ_H^C determined in this paper vary in a range of 95% - 115% around the mean for the S690 steels. The values are in high degree of consistency even the steels are from different sources and different sections of the steel plates.
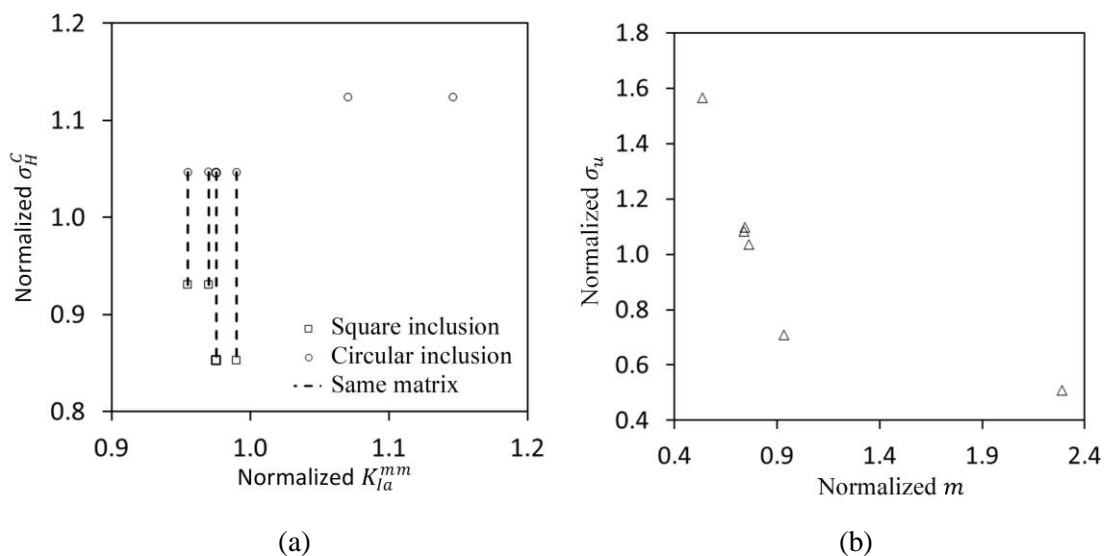

(a)   (b)

Fig. 5.12 Cleavage parameters in middle and top sections of S690-A1, A2, B steels calculated by (a) microstructural-informed model herein and (b) Beremin method proposed in [40]

The surface energy calculated from experimentally measured fractured facet sizes is a more local parameter compared to K_{Ia}^{mm}. The surface energy parameter is used to investigate the boundary of the actual initiation facet, while K_{Ia}^{mm} reflects the statistical equivalent effect of the defined grains. Very few measurements have been reported for bainitic and martensitic steels as their cleavage facets show complex morphology. Linaza [25] estimated a γ_{mm} range of 50-200 J/m² for martensitic steel at 77 K. For ferritic steels, San Martin and Rodriguez-Ibabe [26] calculated a γ_{mm} range of 110-176 J/m² at 77 K. Kawata et al. measured a γ_{mm} range of 25–100 J/m² for Ni-ferritic steels at -100°C [27], considering

correction of facet shape and 3D orientation. The values of γ_{mm} reported in literature vary in the range of 40% - 160% around the mean for a same type of steel. In comparison, K_{Ia}^{mm} determined in the present study vary in the range of 95% - 115% around the mean for three types of S690 steels. The reason is that surface energy is a parameter measured from each cleavage facet and can vary locally among microstructures. K_{Ia}^{mm} is an effective equivalence to model the macroscopic fracture that has average the local variations. When model the macroscopic fracture, the cleavage parameters in the present method are more consistent.

5.6. Conclusions

In the current paper, a statistical modelling approach is applied to estimate the cleavage parameters across different types of steels. Cleavage parameters are compared among three tempered bainitic (S690) steels, an as-quenched martensitic steel, and a ferritic steel. The top quarter and middle sections of the S690 steels are separately modelled in terms of tensile properties, grain sizes, inclusion distribution, and cleavage parameters. The other two types of steels are studied for a single thickness position. The tensile properties, grain sizes, and inclusion distributions of the latter two types of steel are taken from literature. The following conclusions are highlighted:

- The values of cleavage parameter K_{Ia}^{mm} are within 15% variation among all three S690 steels considered in this study, including two different sources. The values of cleavage parameter σ_H^C are within 10% variation for the same type of inclusions.
- The cleavage parameters K_{Ia}^{mm} for S690 steels are more similar to the martensitic steel than to the ferrite-cementite steel. The values of cleavage parameter σ_H^C vary significantly from 2.0 GPa to 4.1 GPa among the steels.
- The variation of cleavage parameter K_{Ia}^{mm} can be explained by the hierarchical grain structure of steels. The value represents the total effect of high misorientation boundaries of a grain on crack arrest.
- The cleavage parameters determined in this paper show a high degree of consistency across different types of steels, which allows the usage of the calculated values in microstructure designs to control macroscopic toughness.

The current method has the following limitations that could be investigated further:
- The current model does not account for the temperature dependence of cleavage parameters.
- Dynamic fracture behaviour is not investigated in this paper.

5

References

[1] Miyata, T., Yang, R. C., Otsuka, A., Haze, T., & Ahira, S. (1989). Cleavage fracture of steels with fine grained ferrite, coarse grained bainitic and martensitic. Proceeding of the seventh international conference of fracture. 2563-2571.

[2] Lee, S., Kim, S., Hwang, B., Lee, B. S., & Lee, C. G. (2002). Effect of carbide distribution on the fracture toughness in the transition temperature region of an SA 508 steel. Acta Materialia, 50(19), 4755–4762.

[3] Ray, A., Paul, S. K., & Jha, S. (1995). Effect of Inclusions and Microstructural Characteristics on the Mechanical Properties and Fracture Behavior of a High- Strength Low- Alloy Steel. Journal of Materials Engineering and Performance, 4(6), 679–688.

[4] Li, X., Ma, X., Subramanian, S. V., Shang, C., & Misra, R. D. K. (2014). Influence of prior austenite grain size on martensite-austenite constituent and toughness in the heat affected zone of 700MPa high strength pipeline steel. Materials Science and Engineering A, 616, 141–147.

[5] Zhou, M. W., & Yu, H. (2012). Effects of precipitates and inclusions on the fracture toughness of hot rolling X70 pipeline steel plates. International Journal of Minerals, Metallurgy and Materials, 19(9), 805–811.

[6] Pineau, A., Benzerga, A. A., & Pardoen, T. (2016). Failure of metals I: Brittle and ductile fracture. Acta Materialia, 107, 424–483.

[7] Beremin FM (1983). A local criterion for cleavage fracture of a nuclear pressure vessel steel. Metall Trans A, 14A, 2277–2287.

[8] Wallin, K., Saario, T., & Törrönen, K. (1984). Statistical model for carbide induced brittle fracture in steel. Metal Science, 18(1), 13–16.

[9] Lin, T., Evans, A. G., & Ritchie, R. O. (1986). A Statistical Model of Brittle Fracture by Transgranular Cleavage. Mrch. Phys. Solids, 34(5), 477–497.

[10] Martín-Meizoso, A., Ocaña-Arizcorreta, I., Gil-Sevillano, J., & Fuentes-Pérez, M. (1994). Modelling cleavage fracture of bainitic steels. Acta Metallurgica Et Materialia, 42(6), 2057–2068.

[11] Chen, J. H., Wang, G. Z., & Wang, H. J. (1996). A Statistical Model for Cleavage Fracture of Low Alloy Steel. Acta Metallurgica, 44(10), 3979–3989.

5

[12] Bernauer, G., Brocks, W., & Schmitt, W. (1999). Modifications of the Beremin model for cleavage fracture in the transition region of a ferritic steel. Engineering Fracture Mechanics, 64, 305–325.

[13] Bordet S.R., Karstensen A.D., Knowles D.M., Wiesner C, S. (2005). A new statistical local criterion for cleavage fracture in structural steel. Part I: model presentation. Engineering Fracture Mechanics, 72, 435–452.

[14] Gao, X., Zhang, G., & Srivatsan, T. S. (2005). Prediction of cleavage fracture in ferritic steels: A modified Weibull stress model. Materials Science and Engineering A, 394(1–2), 210–219.

[15] Lambert-Perlade, A., Gourgues, A. F., Besson, J., Sturel, T., & Pineau, A. (2004). Mechanisms and modeling of cleavage fracture in simulated heat-affected zone microstructures of a high-strength low alloy steel. Metallurgical and Materials Transactions A: Physical Metallurgy and Materials Science, 35(13), 1039–1053.

[16] Shibanuma, K., Nemoto, Y., Hiraide, T., Suzuki, K., Sadamatsu, S., Adachi, Y., & Aihara, S. (2018). A strategy to predict the fracture toughness of steels with a banded ferrite–pearlite structure based on the micromechanics of brittle fracture initiation. Acta Materialia, 144, 386–399.

[17] Kunigita, M., Aihara, S., Kawabata, T., Kasuya, T., Okazaki, Y., & Inomoto, M. (2020). Prediction of Charpy impact toughness of steel weld heat-affected zones by combined micromechanics and stochastic fracture model – Part I: Model presentation. Engineering Fracture Mechanics, 230, 106965.

[18] Irwin, G. (1948). Fracture dynamics, in: Fracturing of Metals vol. 8, American Society of Metals, Cleveland.147-166.

[19] Orowan, E. (1948). Fracture and strength of solids, in: Reports in Progress in Physics, Voll. XII.185.

[20] Griffith, A. (1921). The phenomena of rupture and flow in solids, in: Philosophical Transactions of the Royal Society of London. Series A vol.221,163-198.

[21] Curry, D. A., & Knott, J. F. (1978). Effects of microstructure on cleavage fracture stress in steel. Metal Science, 12(11), 511–514.

[22] Bowen, K., Druce, S.G., & Knott, J.F. (1986). Effects of microstructure on cleavage fracture in pressure vessel steel. Acta metal, 34, 1121-1131.

[23] Alexander, D.J. & Bernstein, I.M. (1989). Cleavage fracture in pearlitic eutectoid steel. Metal. Trans. A, 20, 2321-2335.

5

[24] Linaza, M.A., Romero, J.L., Rodríguez-Ibabe, J.M., & Urcola, J.J. (1995). Cleavage fracture of microalloyed forging steel specimens. Scripta Metall. Mater., 32, 395-400.

[25] Linaza, M.A., Rodríguez-Ibabe, J.M., & Urcola, J.J. (1997). Determination of the energetic parameters controlling cleavage fracture initiation in steel specimens. Fatig. Fract. Eng. Mater. Struct. 20, 619-632.

[26] San Martin, J.I., Rodriguez-Ibabe, J.M., (1999). Determination of energetic parameters controlling cleavage fracture in a Ti-V microalloyed ferrite-pearlite steel. Scripta Mater. 40, 459–464.

[27] Kawata, I., Nakai, H., Aihara, S. (2018). Experimental evaluation of effective surface energy for cleavage microcrack propagation across grain boundary in steels. Acta Mater. 150, 40–52.

[28] Li, Y., Pallaspuro, S., Ren, X., He, J., Kömi, J., & Zhang, Z. (2021). A multi-barrier model assisted CAFE method for predicting ductile-to-brittle transition with application to a low-carbon. Mechanics of Materials, 153, 103669.

[29] Jiang, Q., Bertolo, V. M., Popovich, V.A, Sietsma, J., & Walters, C.L. (2022). Microstructure-informed statistical modelling of cleavage fracture in high strength steels considering through-thickness inhomogeneities. Engineering Fracture Mechanics, 267, 108432.

[30] Bertolo, V. M., Jiang, Q., Scholl, S., Petrov, R., Hangen, U., Walters, C.L., Sietsma, J., & Popovich, V.A. (2022). A comprehensive characterisation and quantification of the multiphase microstructure of a thick-section high strength steel. Journal of Materials Science, 57, 7101–7126.

[31] Pallaspuro, S., Mehtonen, S., Kömi, J., Zhang, Z., & Porter, D. (2019). Effects of local grain size and inclusions on the low-temperature toughness of low-carbon as-quenched martensite. Materials Science & Engineering A, 743, 611–622.

[32] Shibanuma, K., Aihara, S., & Suzuki, K. (2016). Prediction model on cleavage fracture initiation in steels having ferrite-cementite microstructures - Part II: Model validation and discussions. Eng Fract Mech 2016;151: 181-202.

[33] Morris, J.W., Kinney, C., Pytlewski, K., & Adachi, Y. (2013). Microstructure and 756 cleavages in lath martensitic steels, Sci. Technol. Adv. Mater. 14 (1), 014208.

[34] De Hoff, R.T. (1962). The determination of the size distribution of ellipsoidal particles from measurements made on random plane sections. Trans TMS-AIME, 224, 474–486.

[35] ISO 12135. (2018). Metallic materials - Unifed method of test for the determination of quasistatic fracture toughness.

5

[36] Jiang, Q., Bertolo, V.M., Popovich, V.A., Sietsma, J., & Walters, C.L. (2021). Relating local stress on a hard microstructural inclusion from far-field stress on matrix to understand cleavage fracture in high strength steel. International Journal of Fracture, 232, 1–21

[37] Kroon M, Faleskog J (2008) Influence of crack deflection into the carbide/ferrite interface on cleavage fracture initiation in ferritic steels. Mech Mater, 40, 695–707

[38] Qiao Y. 2003 Modeling of resistance curve of high-angle grain boundary in Fe-3wt% Si alloy. Mater. Sci. Eng. A 361, 350–357.

[39] Bertolo, V. M., Jiang, Q., Tiringer, U., Walters, C.L., Sietsma, J., & Popovich, V.A. (2022). Cleavage fracture micromechanisms in thick-section high strength steels. Journal of Materials Science. 57, 20033–20055

[40] Wang, Z., Chen, T.-K., & Lloyd, D. J. (1993). Stress distribution in particulate-reinforced metal-matrix composites subjected to external load. Metallurgical Transactions A, 24(1), 197–207.

[41] Wang, X., Wang, Z., Xie, Z., Ma, X., Subramanian, S., Shang, C., Li, X., & Wang, J. (2019). Combined effect of M/A constituent and grain boundary on the impact toughness of CGHAZ and ICCGHAZ of E550 grade offshore engineering steel, Math. Biosci. Eng. ,16, 7494–7509.

[42] Gao, X., Ruggieri, C., & Dodds, R. H. (1998). Calibration of Weibull stress parameters using fracture toughness data. International Journal of Fracture, 92(2), 175–200.

5

5

6

Microstructure-based cleavage modelling to study grain size refinement and simulated heat affected zones of S690 high strength steel

The contents of this chapter have been submitted to Materials Science and Engineering A as a journal paper (2023).

Abstract

In this research, a microstructure-based method with input from finite element analysis is used to model the cleavage behavior of heat treated S690 steel. Cleavage simulations of steels subjected to heat treatments that cause grain refinement or Gleeble simulated heat affected zones are performed, and are compared with experiments. It is found that the experimental improvement of toughness from grain refinement is 80% of what would be expected based on the model. The 20% difference is due to the lower number fraction of high-angle misorientation boundaries. It is also found that the resistance to micro-crack propagation is more effective in heat affected zones, which can be explained by the residual compressive stress in martensite-austenite constituents. This study informs the trade-off between microstructural parameters and helps a designer choose a process for controlling cleavage toughness.

6.1 Introduction

Processing parameters (e.g., weld travel speed, process, wire composition, cooling rate, etc.) determine the ability of the microstructure of high strength steel to generate sufficiently tough base metal/weld/Heat Affected Zone (HAZ) combination [1]. In order to balance cost, toughness, and strength, it is critical for material designers to know the separate and combined effects of various microstructural features on cleavage, such as prior austenite grain size [2], carbide size [3], the presence of inclusions [4], M-A (martensite-austenite) phases [5], precipitates, etc. (for an overview, see [6]).

6

Better modelling of the relationship between the microstructures resulting from welding processes and HAZ toughness can lead to more cost-effective development and usage of welding procedures.

Austenite grain refinement has been recognized as an effective method to improve mechanical properties of high strength steels [7–9]. There are multiple studies performed on refining of austenite grain size [10-14]. However, high strength steels often have bainitic or martensitic microstructure, which has hierarchical crystallographic structures. In this case, the definition of grain is complicated, as a grain can be defined as prior austenite grain (PAG), packet, block, or lath [15]. Although it is generally observed that the refinement of a prior austenite grain can improve both strength and toughness of steel, it is also reported that the PAG refinement is less effective than expected as the local fracture stress is observed with little influence [16]. A modelling method that can incorporate comprehensive microstructure is needed to help estimate the effectiveness of grain refinement. There are a few attempts [17][18] to model the effect of grain size on cleavage toughness of steels using microstructure-based methods. However, those attempts did not validate the effect of isoparametric change in grain size.

Welding thermal cycles produce heterogeneous microstructure in the HAZ [19]. Coarse-grained heat affected zone (CGHAZ) and intercritically reheated coarse-grained heat affected zone (ICCGHAZ) are found to have low fracture toughness due to the coarsening of austenite grains and the formation of martensite-austenite (M-A) constituents [20–23]. One of the complexities of modelling the fracture process in an HAZ is when there are pre-existing carbides and brittle inclusions in the base material. Li and Baker [24] observed in a V and Nb microalloyed steel that M-A constituents have a more pronounced impact on the fracture process of ICCGHAZ than pre-existing carbides and aluminium oxide inclusions. Vassilaros [25] found in ultra-low carbon bainitic steel that the pre-existing TiN inclusions rather than M-A constituents trigger cleavage fracture in the CGHAZ. Therefore, a modelling method that can consider different types of brittle particles is needed to better understand the cleavage micromechanisms in a welded multi-phase steel.

This study contributes new knowledge to the understanding of cleavage fracture of steels subjected to heat treatments that cause grain refinement or simulated heat affected zones. The first objective is to estimate the effect of grain refinement on toughness improvement of a multi-phase steel, with numerical simulations and validation from a mostly isoparametric experimental program. It investigates how model parameters should be adjusted for changes in prior austenite grain sub-structures. The second objective is to simulate the cleavage fracture in welded steels with different types of brittle particles. It provides insight into the modelling of toughness degradation in CGHAZ and ICCGHAZ that contain pre-existing brittle inclusions.

6

The numerical method used in this paper was proposed by Jiang et al [26] based on prior multi-barrier models [27, 28] and has been demonstrated on fracture data from a S690 QT steel plate that was fractured at -100 ° C [26]. The method represents the cleavage fracture toughness of steels incorporating statistical information of microstructures and tensile properties. The method accounts for several microstructural features (grain size, hard particle size, and hard particle geometries) simultaneously, and incrementally considers the deactivation of crack initiators. Cleavage parameters K_{Ia}^{mm} (crack arrest of the grain boundary), and σ_H^C (critical fracture stress of hard inclusion) are the values fitted from fracture experiments and can be used to estimate the effect of microstructures affected heat treatments.

The current research applies the method to model the cleavage behavior of Gleeble heat treated S690 QT steel at -100°C and -40°C. The first type of heat treatment is a rapid cyclic heating (RCH) to represent variation of microstructure that solely refines the grains. The second type of heat treatment simulates HAZs, which represents welded microstructures where grains are coarsened and martensite-austenite (M-A) constituents are generated. In addition, theoretical calculation based on a multi-barrier model [26] are performed for variations of microstructural parameters, such as grain size and hard particle distributions (while keeping other modelling parameters constrained). The heat-treated materials' fracture behaviours are compared with the theoretical calculations.

6.2 Materials

A commercially available 80 mm thick quenched and tempered S690 high strength steel plate is used in this paper. The chosen thickness position for this study is the middle section that represents the worst fracture toughness of the S690 QT steel plate. Gleeble heat treatments were carried out to generate a grain refined microstructure, coarse-grained heat affected zone (CGHAZ) and intercritically reheated coarse-grained heat affected zone (ICCGHAZ). In the rest of the paper, the Gleeble simulated HAZ is referred to as HAZ for conciseness. The details of the heat treatment can be found in [29, 30] and a brief description is provided in the following paragraphs.

The RCH treatment route is applied to generate a refined grain microstructure, which includes the following steps: heating up the sample from room temperature to 870°C (above Ac₃) at 20°C/s and soaking at 870°C for 120 s; afterwards, industrial quenching and tempering heating and cooling profiles are used in to keep the microstructure and composition as close as possible to the as-received steel.

The thermal profile for the CGHAZ was experimentally obtained from an actual gas metal arc welding with a heat input of 2.2 kJ/mm. First, the material is heated at 210 °C/s up to 1300 °C and held for 2 s. Subsequently, the material is cooled down at 25 °C/s from 1300 to 800 °C, 17 °C/s from 800 to 500 °C, and 6 °C/s to room temperature. For the ICCGHAZ, the thermal profile for the first cycle was the same as used for the CGHAZ, followed by a second cycle with the same heating and cooling rates

6

as the first step, but with peak temperature 750°C (within the critical Ac_1 and Ac_3 temperatures). These thermal profiles were used to perform Gleeble thermal treatments (via Gleeble-1500 thermo-mechanical simulator) on samples for microstructural characterization, tensile and fracture testing.

The fracture tests were performed at -100°C for the RCH treated steel, and at -40°C for CGHAZ and ICCGHAZ. Fracture tests of the as-received reference steel were performed at both -100°C and -40°C. The different test temperature is aimed to have fracture mode of heat-treated steels in cleavage.

6.2.1 Microstructures

The as-received material has a microstructure of 64% tempered bainite, 29% tempered martensite, and of less than 7% ferrite [29]. The RCH treatment was designed to keep the microstructure of the as-received steel and the phases observed in the as-received steel remained present as shown in Fig. 6.1. The specimens of CGHAZ contain 88% auto-tempered martensite, 6% martensite and 6% coalesced martensite. The specimens of ICCGHAZ have a microstructure of 71% granular bainite, 12% auto-tempered martensite, 8% martensite, and of less than 10% ferrite [30]. Fig. 6. 1 shows the overview of microstructures of the steels. Details of the microstructure characterization can be found in [29, 31].

(a) As-received

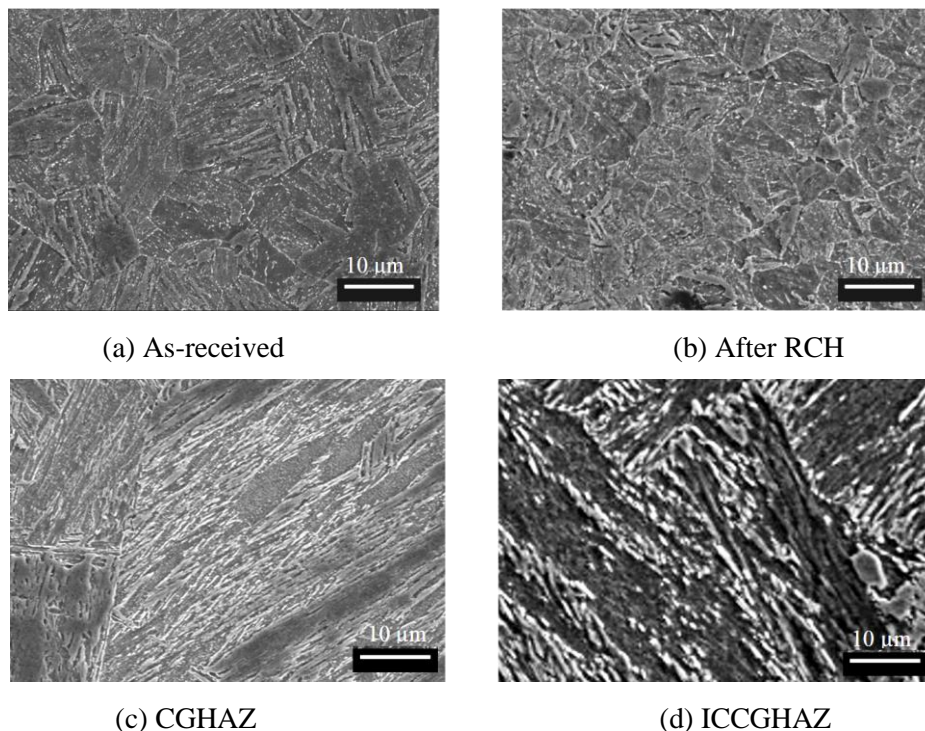(b) After RCH

(c) CGHAZ

(d) ICCGHAZ

Fig. 6. 1 Micrographs of S690QT steel before (a) and after heat treatments (b)-(d) [29, 30]

Prior Austenite Grains (PAG) are reconstructed based on EBSD measurements [29, 30]. The EBSD measurements were repeated at different locations for each steel. The statistical distribution of the grain size (D in μm) is obtained by least-square fitting of the grain size data to the function $P(D)$. $P(D)$ is a

combined function of lognormal distribution and power-law distribution, in order to accurately represent the tails:

$$P(D) = \min\left\{1 - f(D, \mu, S), \frac{\alpha}{D^\beta}\right\} \qquad \text{6-2-1}$$

with $f(D, \mu, S)$ representing equation $1/2 + 1/2\text{erf}(\frac{lnD - \mu}{\sqrt{2}\,S})$, where α and β are fitting parameters, μ is the mean and S is the standard deviation.

Fig. 6. 2 shows the grain size data measured from EBSD with the fitted curves for the as-received steel, RCH treated steel, CGHAZ, and ICCGHAZ. After the RCH treatment, grain refinement by 55% (in terms of average value) was achieved. After the HAZ heat treatment, grains are coarsened by 195% and 237% (in terms of average value), for CGHAZ and ICCGHAZ, respectively. The cusp in the plot is explained by the change between the two fitted probability functions. It is observed in Fig. 6. 2 that when the eq. 6-2-1 shift from lognormal distribution to power law distribution the cusp is concave. It indicates a nonproportional change in the tail of the grain size distribution compared with the mean. For RCH and HAZ treatments, the large-grain tail of the distribution becomes thinner compared to the as-received material.
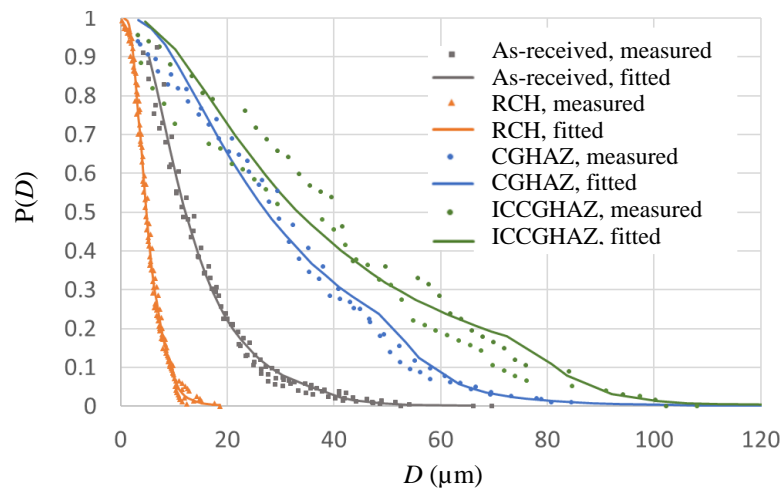

Fig. 6. 2 Distribution of the major axis of PAG

The hard particles that act as initiator of cleavage cracks in the as-received steel and in the steel after grain refinement are found to be circular oxides that are in the size range of 1-5 µm and rectangular Nb-rich inclusions that are in the size range of 1-12 µm. The oxides and Nb-rich inclusions are not changed after the heat treatments, and the characterization performed in as-received steel is used to model the particle distributions in the heat-treated steels. The size of circular inclusions (oxides) is measured as equivalent diameter, while the rectangular inclusions (Nb-rich inclusions) are represented by the longer axis. Fig. 6. 3 shows the inclusion size distributions measured by Keyence digital microscope. The number density of oxides and Nb inclusions is calculated as 38 and 13 per 0.001 mm^3,

6

respectively, which is converted from 2D measurements according to Schwartz-Saltykov method [31]. In the CGHAZ and ICCGHAZ, M-A constituents in sizes of less than 1 μm are present. The longer axis of M-A constituents is measured, and the size distribution is shown in Fig. 6. 4. The M-A constituents are distributed with a density of 7.2×10^5 and 1.38×10^6 per 0.001 mm^3 for CGHAZ and ICCGHAZ, respectively. Eq. 6-2-1 is used to fit the statistical distribution of hard particles, which provides input for the cleavage modelling.
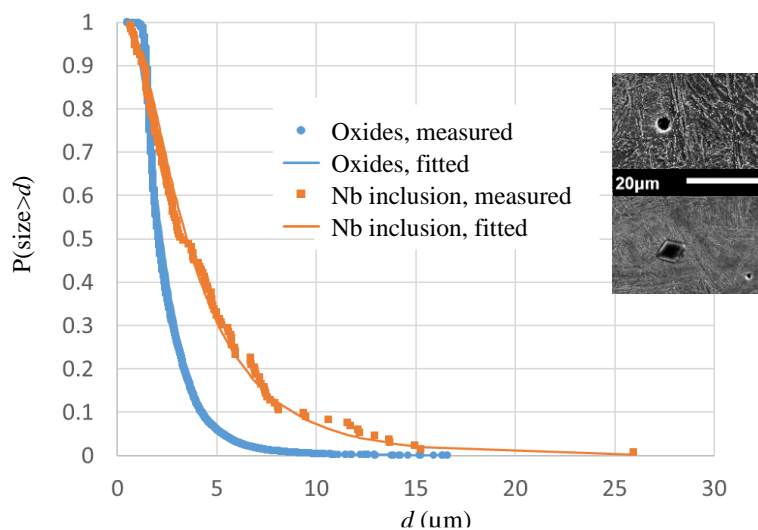
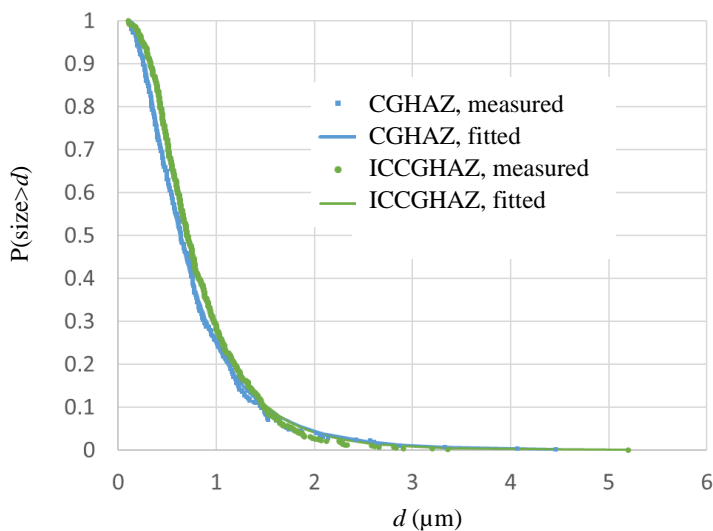Fig. 6. 3 Size distribution of inclusions (with SEM micrographs showing the morphology)

Fig. 6. 4 Distribution of longer axis of M-A constituents in HAZs

6.2.2 Tensile properties

Tensile tests were carried out at room temperature. The stress-strain relationship of the steels is characterized by Ludwik's law, which is defined with the flow stress (σ) and the effective plastic strain (ε_p) as:

$$\sigma = \sigma_y + K\varepsilon_p^{n_L}.$$

6-2-2

where, σ_y, K and n_L are material parameters. The parameters of Ludwik's law are fitted from tensile tests at room temperature and are converted to tensile curves at the fracture temperatures (according to ISO 12135 [32]) to generate material input for FE models.

$$\sigma_{low\ temperature} = \sigma_{room\ temperature} + \frac{10^5}{(491+1.8T)} - 189. \qquad \text{6-2-3}$$

where T is the low temperature in °C. Fig. 6. 5 shows the comparison of flow stress versus plastic strain relationships fitted for the steels and converted to the fracture temperatures.
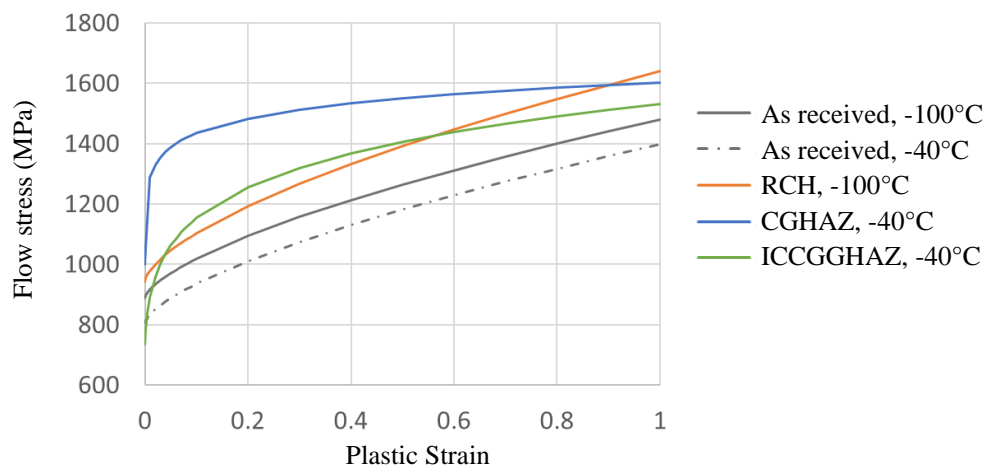

Fig. 6. 5 Flow stress vs plastic strain curves of steels

As the hardening behaviour shows differences among the steels, the representative flow stress for comparison is defined by the average of yield strength (0.2%-offset stress) and the ultimate tensile strength. The refined grain size after RCH treatment results in a flow stress increase of 7%. The changed phases in CGHAZ and ICCGHAZ lead to an increase of the flow stress in comparison with the as received steel, by 44% and by 14%, respectively.

6.3 Methods

6.3.1 Finite element model

Fracture tests to study grain refinement were performed on deep cracked (a/W=0.5) single edge notched bending (SENB) specimens, and fracture tests to study HAZs were performed also on shallow cracked (a/W=0.1) specimens. Fig. 6. 6 shows the geometry of the SENB specimens, including crack length a and specimen height W. For high constraint specimens (a/W=0.5), the initial crack length is 10 mm, including a 8.6 mm notch and a 1.4 mm pre-fatigued crack. For low constraint specimens (a/W=0.1), the initial crack length is 2 mm, including a 1.4 mm notch and a 0.6 mm pre-fatigued crack. Table 6.1 summarizes the number of samples and test temperatures for each material.
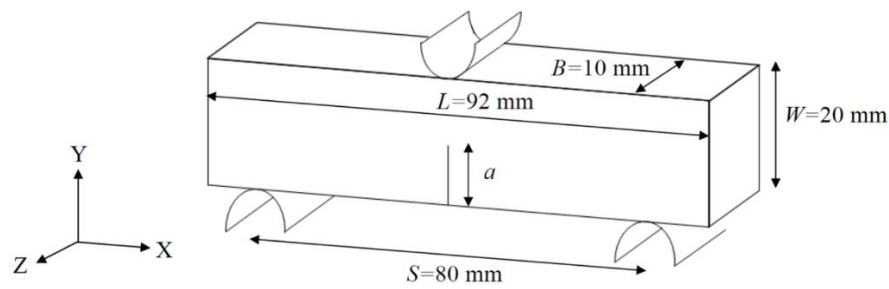
6

Fig. 6. 6 Geometry layout of the SENB specimen

Table 6.1 Number of samples and test temperatures

a/W	Material	Number of samples	Test Temperature °C
	As received	14	-100
		9	
0.5	CGHAZ	10	-40
	ICCGHAZ	9	
	RCH	8	-100
	As received	13	
0.1	CGHAZ	10	-40
	ICCGHAZ	9	

SENB specimens are modelled in Abaqus 2017 for each type of steel. A quarter of the specimen $(L/2 \times B/2 \times W)$ is modelled as a 3D deformable solid by using symmetry as shown in Fig. 6. 7 (a). The support and load roller are modelled as analytical rigid surfaces. The contact surface between rollers and the specimen is frictionless. Fig. 6. 7 (b) shows the mesh near the crack tip. The initial pre-fatigued crack tip is modelled as a finite notch that is 0.005 mm in radius. A 20-noded hexahedral element with reduced integration (C3D20R) is used for the mesh. The smallest element near the crack tip has the dimension 0.001 mm×0.005 mm×0.067 mm. A convergence study on element size has been conducted. Displacement control is used to apply a total deflection of 1 mm. A full Newton-Raphson algorithm is used to solve the geometric and material nonlinearity in an implicit method.
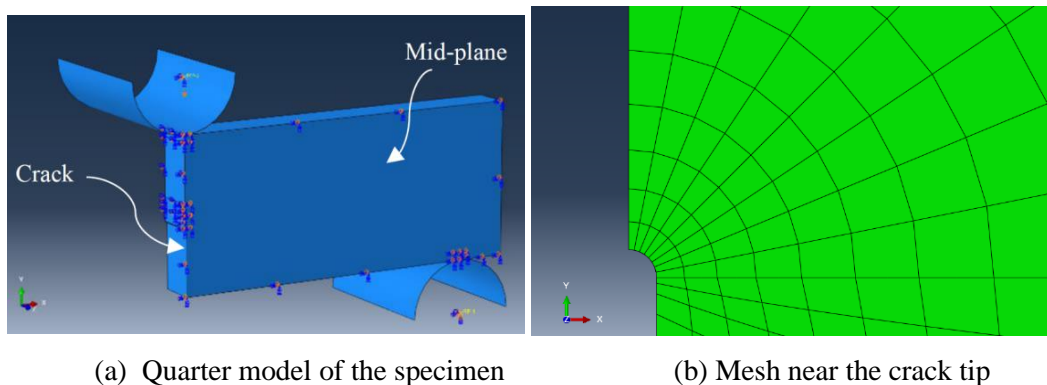
(a) Quarter model of the specimen   (b) Mesh near the crack tip

Fig. 6. 7 Finite element model of the three-point bending test

6.3.2 Micromechanism-based cleavage model

The model applied in this paper is developed in [26] and is based on a multiple-barrier theory of the cleavage mechanism [27, 28]. Cleavage fracture of steels is regarded as the result of successive occurrence of three events (as illustrated by Fig. 6. 8):

I: nucleation of a slip-induced crack in a brittle second-phase particle or inclusion;

II: propagation of the microcrack across the particle/matrix interface;

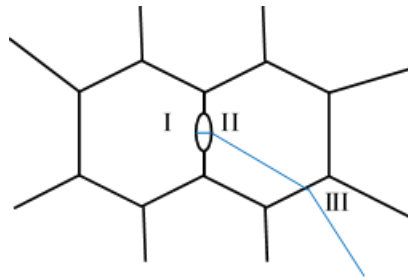III: propagation of the crack of a grain-size length scale across the grain boundary.

Fig. 6. 8 Critical events of cleavage fracture

The stress level needed for inclusion cleavage is characterized by particle strength σ_H^C (event I). It is assumed that the value of inclusion strength is uniformly distributed in the range [σ_H^C, $\sigma_H^C + \Delta \sigma_H^C$]. For a volume that contains N inclusions, the number of cracked inclusions (N_{cr}) is proportional to the stress σ_H at the inclusion, and can be calculated for $\sigma_H > \sigma_H^C$ as:

$$N_{cr} = \min\{N \times (\sigma_H - \sigma_H^C)/\Delta \sigma_H^C, N\},$$
6-3-1

where the stress σ_H at the inclusion is calculated from the first principal stress of the matrix $\sigma_{1,m}$ and the equivalent von Mises stress of the matrix $\sigma_{eq,m}$, by

$$\sigma_H = \sigma_{1,m} + f_\alpha \sigma_{eq,m},$$
6-3-2

where the factor f_α is based on the inclusion geometry and is determined using the analytical expression in [33].

A critical stress is usually used as a criterion for the crack propagation across the particle/matrix interface (event II) or across the grain boundary (event III). In the present paper, the equivalent toughness at the particle/matrix interface is characterized by the local cleavage parameter K_{Ia}^{pm}, and the equivalent toughness at the grain boundary is characterized by the local cleavage parameter K_{Ia}^{mm}. A minimum crack size equal to particle size (d_c) (event II) or rather grain size (D_c) (event III) is calculated for the first principal stress within the grain ($\sigma_{1,m}$) to propagate the micro-crack across the particle/matrix interface or the grain boundary, respectively by:

6

$$d_c = (K_{Ia}^{pm}/\sigma_{1,m})^2 \qquad\qquad 6\text{-}3\text{-}3$$

$$D_c = (K_{Ia}^{mm}/\sigma_{1,m})^2. \qquad\qquad 6\text{-}3\text{-}4$$

Fig. 6. 9 gives a flow chart of the computational model to calculate the cleavage probability of macroscale specimens. Finite element analysis (FEA) of a macroscopic volume gives the stress/strain distribution (which contains $\sigma_{1,m}$, $\sigma_{eq,m}$, and ε_p values for each finite element) at each load increment. The cleavage probability is calculated from a cleavage check based on the stress level, shape of the stress field, and statistical information of the microstructure. By accounting for the cleavage probability of all finite elements in the fracture process zone (areas that are plastically deforming), the total failure probability (P_f) of the specimen is calculated and expressed as a function of the global load. In addition to FEA stress and strain results, the required input includes f_α calculated from inclusion geometry, the distribution function of the grain size $P(D)$, the distribution function of the hard particle size $P(d)$, number of inclusions N per unit of volume, and cleavage parameters K_{Ia}^{pm}, K_{Ia}^{mm} and σ_H^C. Other predefined parameters are threshold plastic strain $\varepsilon_{p,t}$, elementary volume V_0, and scatter of the inclusion fracture strength $\Delta\,\sigma_H^C$. All predefined values are summarized in Table 6.2.
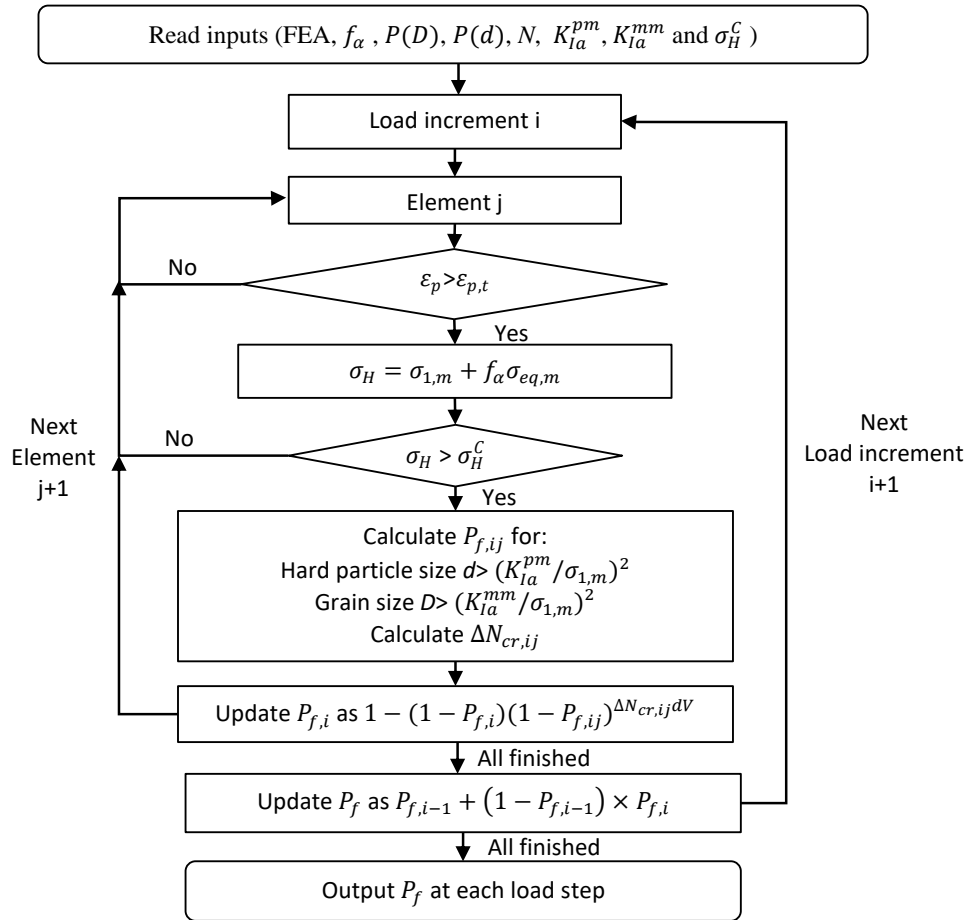

Fig. 6. 9 Flow chart of the computational scheme [26]

Table 6.2 Value of the pre-defined input parameters

Parameters	Values
Threshold plasticity strain $\varepsilon_{p,thre}$	10^{-5}
Elementary volume V_0	0.001 mm^3
Stress concentration factor of spherical inclusion f_α	0.239
Scatter of the inclusion fracture strength $\Delta \sigma_H^C$	100 MPa

6.4. Results

6.4.1 Simulation of base material

Analysis of the as-received steel indicates that micro-crack propagation is grain-size controlled [26], as the brittle inclusions have a relatively large dimension (95% of brittle inclusions are larger than 1.5 µm), and the nucleated microcracks are in sizes that enable them to propagate into the surrounding grain. Examination of fracture surfaces of the reference steel was performed in our previous study using SEM to characterize the mode of failure and to locate and identify microstructural features that can trigger cleavage [34]. The smallest inclusions that are identified as local cleavage fracture initiation sites are of sizes 1.22 ± 0.08 µm (in specimen a/W=0.5) and 1.27 ± 0.10 µm (in specimen a/W=0.1). The micro-cracks originating from such inclusion sizes are able to propagate across the inclusion/matrix interface and form cleavage facets in neighbouring grains. FEA shows that $\sigma_{1,m}$ is in the range of 2000 – 2500 MPa at the location of crack initiation sites. K_{Ia}^{pm} can be determined by eq. 6-3-3 with the identified particle size and stress state at the crack initiation site as 2.5 MPa$\sqrt{\text{m}}$. Cleavage parameters K_{Ia}^{mm} (grain boundary property) and σ_H^C are determined by inverse analysis (maximum likelihood fitting) from the measured crack tip opening distance (CTOD) of high-and low-constraint specimens. The failure probability, P_f, of a specimen fractured in experiment, was calculated as a rank probability according to [35]:

$$P_f = \frac{i - 0.3}{N + 0.4}$$
<div align="right">6-4-1</div>

where *i* is the rank number in terms of CTOD and *N* is the total number of experiments.

The fitting on specimens fractured at temperature -100°C is reported in [26], which results in σ_H^C equals to 2.7 GPa for oxides and 2.2 GPa for rectangular inclusions; K_{Ia}^{mm} equals to 19.5 MPa$\sqrt{\text{m}}$ for both. Fitting on specimens fractured at temperature -40°C is performed assuming the same value for σ_H^C, and K_{Ia}^{mm} is determined by inverse analysis on high constraint specimens. The resulting K_{Ia}^{mm} is

$22.6\ \text{MPa}\sqrt{\text{m}}$. Fig. 6. 10 shows the comparison of experiments and the simulation using the fitted parameters.
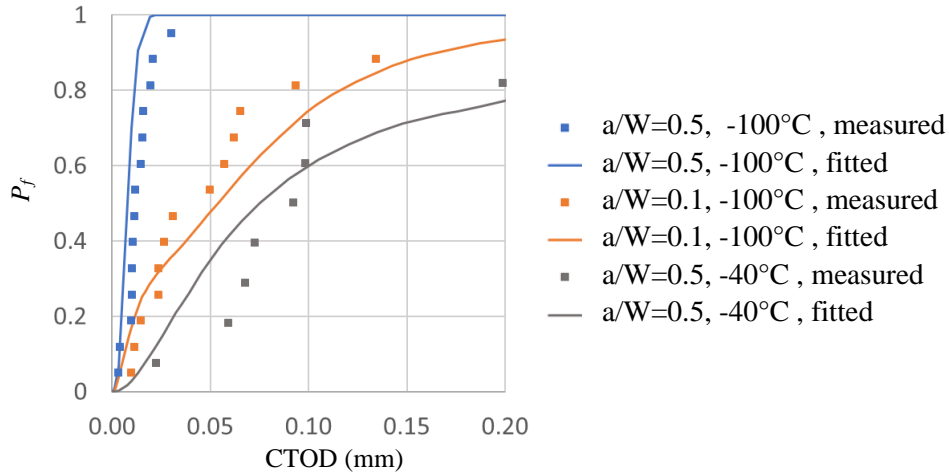

Fig. 6. 10 Cleavage probability calculation of as-received steel

6.4.2 Simulation of grain size refinement specimens

After RCH, the inclusions are unaltered (same size, composition, shape, and distribution), and σ_H^C is assumed to have the value determined from the reference steel, 2.7 GPa for oxides and 2.2 GPa for rectangular inclusions. Cleavage parameter K_{Ia}^{mm} (grain boundary toughness) is determined by inverse analysis (maximum likelihood fitting) from the measured CTOD of high-constraint specimens. The resulting K_{Ia}^{mm} is $17.6\ \text{MPa}\sqrt{\text{m}}$. Fig. 6. 10 shows the comparison of experiments and the simulation using the fitted parameters.

If the grain refined material is simulated with the K_{Ia}^{mm} value of the as-received steel, rather than with the fitting, the distribution of calculated CTOD is shown by the dashed line in Fig. 6. 11. The assumption of unaltered K_{Ia}^{mm} results in calculated CTOD much higher than the experimental values. With unaltered K_{Ia}^{mm}, the grain refinement corresponds to the measured fracture toughness will be 46%. It is lower than the actual grain refinement by 55%. In another words, the experimental improvement of toughness based on grain size refinement is 80% of what would be expected based on simulations.
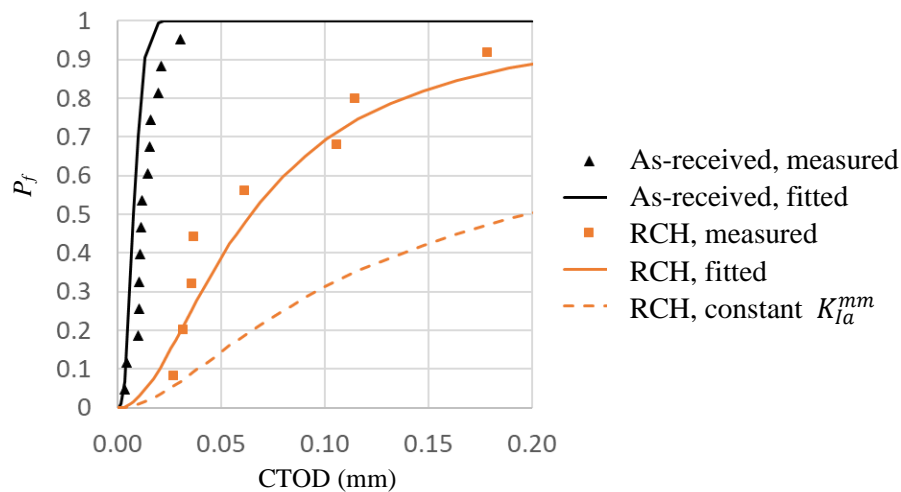
6

Fig. 6. 11 Cleavage probability calculation of *a/W*=0.5 specimens fractured at -100°C

6.4.3 Simulation of HAZ

Clear river lines were not observed on the fracture surface of HAZs, which may suggest multiple initiation sites [30]. Particles that resemble M-A constituents are present at cleavage facets where river lines appear to be converging, which are likely initiation sites [30]. Therefore, three types of simulations are performed based on three different underlying assumptions: (i) inclusions initiate cleavage, (ii) M-A constituents initiate cleavage, (iii) and cleavage triggered by both inclusions and M-A constituents.

The fittings are performed on both high-and low-constraint specimens with the following procedures: when inclusions are assumed to trigger the final fracture, the fracture stress σ_H^C for circular and rectangular inclusions are the same as in the base material, and K_{Ia}^{mm} for grain boundaries is fitted for the HAZ material; when M-A constituents are assumed to trigger the final fracture, cleavage parameters σ_H^C for M-A and K_{Ia}^{mm} for grain boundaries are fitted; when cleavage is assumed to be triggered by both inclusions and M-A constituents, σ_H^C for M-A and K_{Ia}^{mm} for grain boundaries are fitted. σ_H^C for M-A is assumed to be constant among CGHAZ and ICCGHAZ, while K_{Ia}^{mm} is assumed to be varied. The fitted cleavage parameters are summarized in Table 6.3 and the comparison of simulations and experiments are shown in Fig. 6. 12.

Table 6.3 Fitted cleavage parameters for HAZ and as received steel at -40°C

Initiator of micro-crack	σ_H^C of M-A (GPa)	K_{Ia}^{mm} (MPa$\sqrt{m}$)			σ_H^C of inclusion (GPa)*
		CG	ICCG	As received	
Inclusion	--	38.5	33.4	22.6	2.7 for oxides and 2.2 for rectangular inclusions
M-A	2.0	39.4	32.2	--	
M-A & inclusion	2.2	41.1	35.0	--	

* Fitted from as received steel and is considered as a constant value after heat treatment.
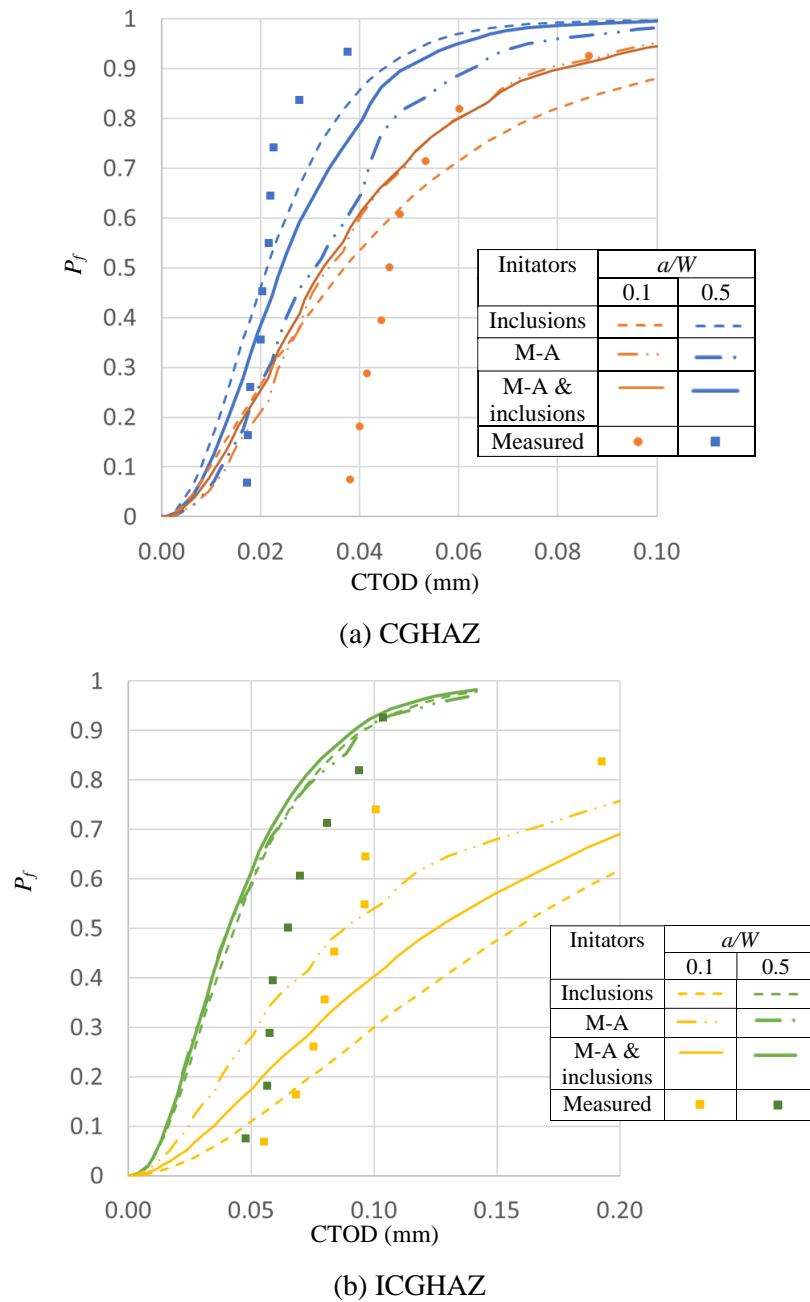
(a) CGHAZ

(b) ICGHAZ

Fig. 6. 12 Cleavage probability calculation of HAZ specimens fractured at -40°C

Three hypotheses are tested, which all yield similar conclusions. The fitted K_{Ia}^{mm} is very high for HAZs; it represents effective resistance to micro-crack propagation. The fitted K_{Ia}^{mm} is lower for ICCGHAZ compared to CGHAZ, which agrees with the finding of Lambert [28]. Assuming that M-A constituents act as the only crack initiator improves the fitting quality for the low-constraint ICCGHAZ specimens.

6.4.4 Numerical study on grain size and flow stress

To compare the heat-treated materials' fracture behaviour with theoretical calculations, a systematic study on grain size and flow stress is performed by means of numerical simulations. A series

of simulations to show the effect of grain size is performed for fracture occurring at -100°C and -40°C with cleavage parameters determined from the as-received material, assuming grain sizes are changed independently from all other modelling parameters. Another simulation is performed for increased flow stress as it can change as a consequence of the refined grain size. Fig. 6. 13 shows the sensitivity of CTOD values to the material factors, where the CTOD and the independent parameters are both normalized by the value of the as-received steel. The calculated CTOD is represented by the median value.
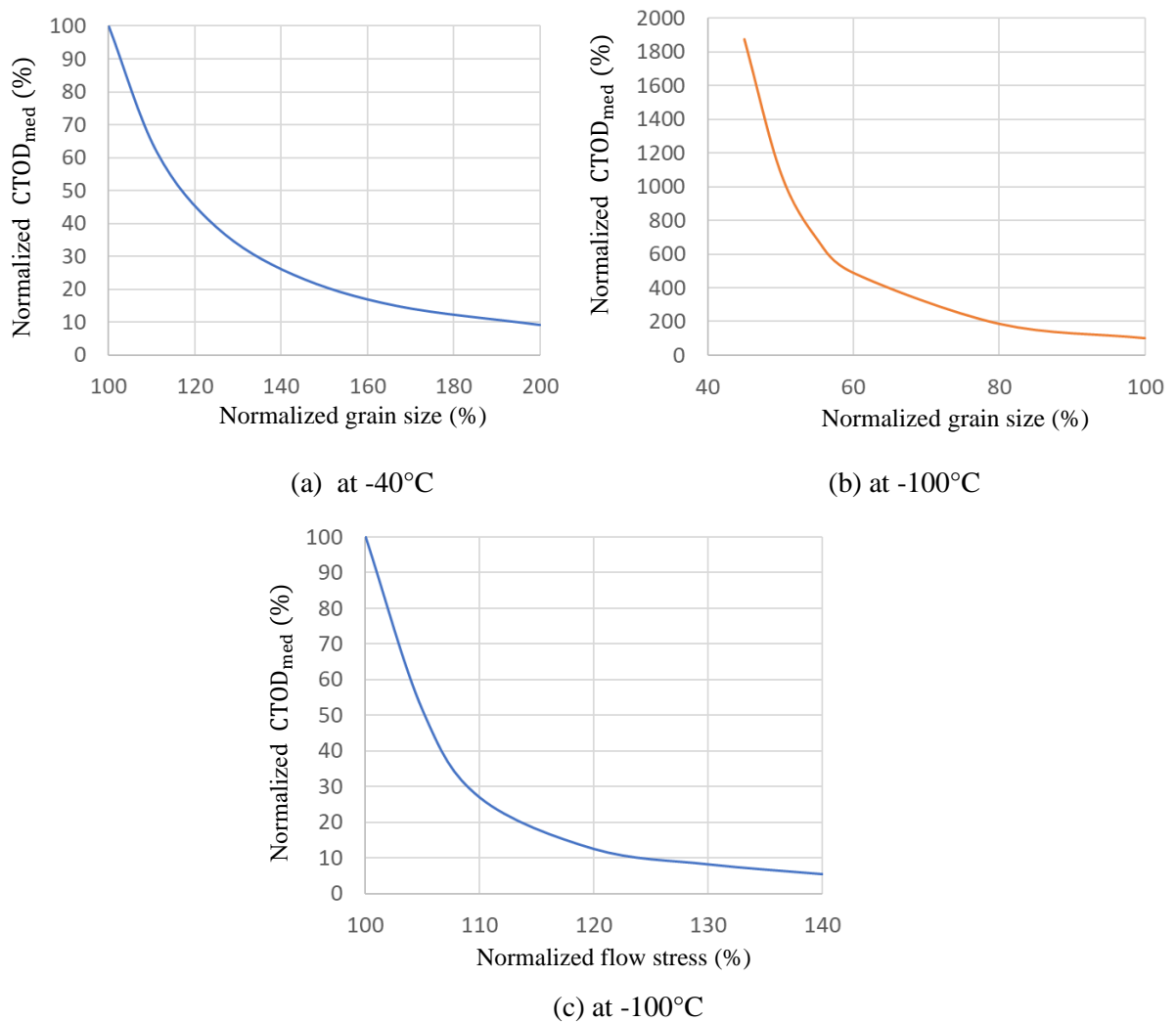

(a) at -40°C

(b) at -100°C

(c) at -100°C

Fig. 6. 13 Simulated median CTOD with (a)increased grain size (b) decreased grain size and (c) flow stress (CTOD values and the independent parameters are normalized by the value of as-received steel)

Although the increased yield stress shows a detrimental effect on toughness, this influence is less than the improving effect of refined grain size for the heat-treated steel, considering that the correlation between grain size and yield strength is a Hall-Petch relationship:

$$\sigma = \sigma_0 + KD^{-1/2} \quad . \qquad\qquad 6\text{-}4\text{-}2$$

6.4.5 Numerical study on particle size and density

Reducing the density or refining hard particles that initiate microcracks is another method to improve toughness through microstructure control [4]. However, for the HAZ specimens, it is not determined if M-A or inclusions are the dominant hard particles that initiate the primary cleavage crack. A sensitivity study on particle size and density is performed by means of numerical simulation of the HAZ specimens.

The simulations are performed for ICCGHAZ specimens fractured at -40°C. The cleavage parameters are determined from the ICCGHAZ with the assumption of both M-A and inclusions initiating the primary cleavage crack. Fig. 6. 14 shows the sensitivity of CTOD values when assuming M-A or inclusions are removed from the material. The results suggest that the simulated CTOD of high constraint specimens is not sensitive to the presence of M-A, while removing inclusions effectively increase the CTOD values. M-A constituents are more responsible for initiating cracks in low constraint specimens, as the effect of removing M-A to improve the CTOD values is at the same level as of removing inclusions.
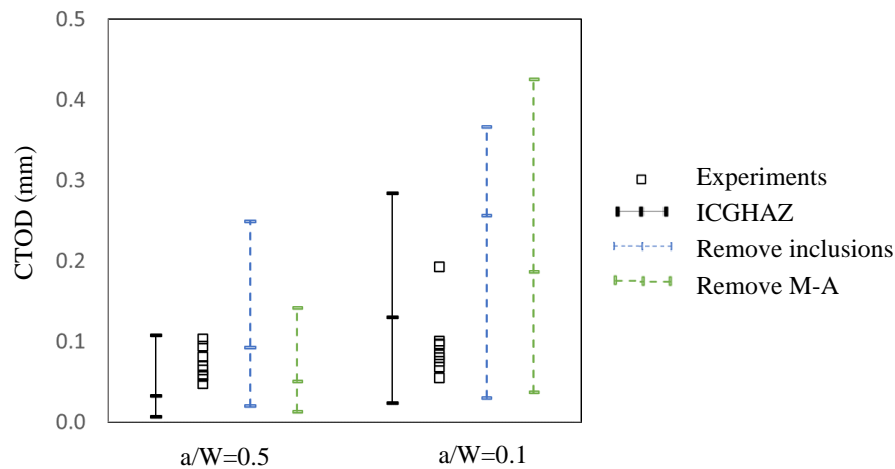

Fig. 6. 14 Changes of simulated CTOD when assuming hard particles are removed (lines correspond to Min-Median-Max in simulated CTOD values)

Alternative to removing hard particles, refining hard particles can also effectively improve toughness [24]. Fig. 6. 15 shows the changes of simulated CTOD when assuming inclusions sizes are refined. The results show that refining inclusions sizes by 20% can effectively increase the CTOD values of both high and low constraint specimens, and further refining will contribute less. For M-A, the simulated CTOD of high constraint specimen is not sensitive to refining the M-A, while in low-constraint specimens, the effect of refining M-A is at the same level as of refining inclusions.
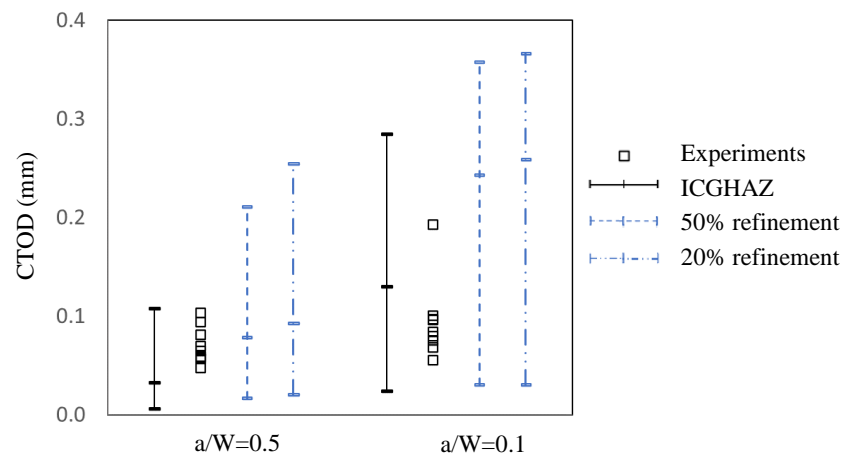
Fig. 6. 15 Changes of simulated CTOD when assuming inclusions are refined (lines corresponds to Min-Median-Max in simulated CTOD values).

6.5 Discussion

In this research, cleavage behaviours of heat treated S690 QT steel at -100°C and -40°C are modelled. The simulation results are discussed and compared in this section. Table 6.4 summarizes the changes in key properties of the steels after three different heat treatments.

Table 6. 4 Changes of properties relative to as-received steel

Heat treatment	Flow stress	Grain size	CTOD
RHC	↑7%	↓57%	↑516%
CGHAZ	↑44%	↑195%	↓80%
ICCGHAZ	↑14%	↑237%	↓35%

6.5.1 Temperature dependence of K_{Ia}^{mm} for as-received steel

It has been shown in [27] that the cleavage parameter of particle/matrix interface K_{Ia}^{pm} is independent of temperature and the cleavage parameter of grain boundaries K_{Ia}^{mm} is strongly temperature dependent in the ductile-to-brittle transition range. In the present paper, K_{Ia}^{mm} of as-received S690 QT steel is found to increase by 13% when the temperature is raised from -100°C to -40°C. The tendency agrees with reported findings in [27]. The increasing K_{Ia}^{mm} with temperature also agrees with the observations obtained from acoustic emission measurements in [28], which suggests that at increasing temperature, cleavage is controlled by the propagation of microcracks arrested at grain boundaries.

The temperature dependence for surface energy γ_{mm} of grain boundaries was measured in [36, 37] from the analysis of initiation facets. Taking the results from [36] as a reference, the value of γ_{mm} is

6

increased by 46% when the temperature is raised from -100°C to -40°C. Applying the relationship $K_{Ia}^{mm} \propto \sqrt{\gamma_{mm}}$ [36, 37], the 46% increase in γ_{mm} results in a 21% increase in K_{Ia}^{mm}. However, it should be noted that the relationship shows large diversity for different types of steel, and the results in [36, 37] are for ferrite-pearlite microstructures.

6.5.2 The effect of RCH treatment

The objective of the RCH treatment was to reduce the grain size while retaining the phases of the as-received material. After the post-process heat treatment, grain refinement of 57% (in terms of average value) was achieved, with the flow stress increased by 7%. The average CTOD of the heat-treated steel is increased by 516% with respect to the as-received steel. The fitted cleavage parameter K_{Ia}^{mm} is lower than for the as-received steel, which indicates that the grain refinement on toughness improvement is not fully effective as the equivalent resistance to crack propagation decreases.

Grain boundary misorientation angles for the as-received steel and the heat-treated steel are shown in Fig. 6.16. Low-angle misorientations are typically distributed between laths, while high-angle misorientations, including packet and block boundaries, are distributed within PAG. For the studied steel, the fraction of high misorientation angles (>15°) remains constant around 90% after heat treatment. The peaks around 60° show a certain decrease after the heat treatment.
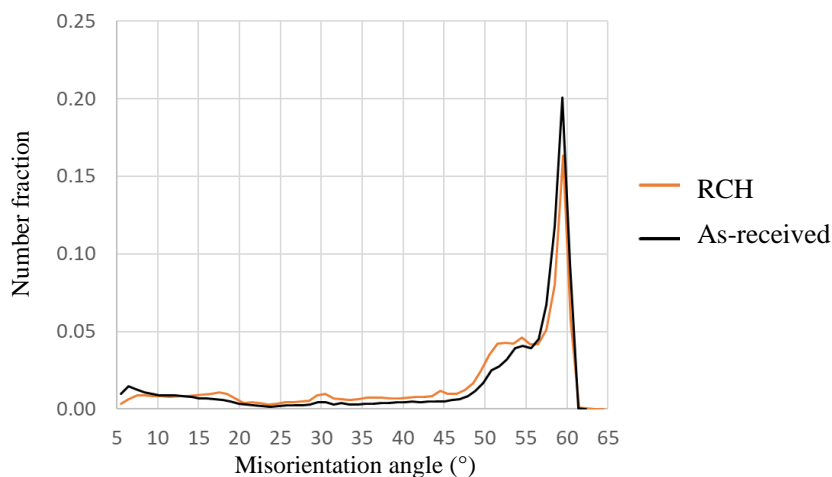

Fig. 6. 16 Grain boundary misorientation angle of as-received steel and steel after RCH [29].

The high-angle misorientations are beneficial for the toughness because they are effective barriers and cause cracks to deviate. The lower number fraction of high-angle misorientations (the peak of the distribution, which is in 55-60°) reduces the efficiency of refined grain size on toughness improvement. In [29], the packet size and block widths for the as-received and the grain-refined S690QT steel are presented. The average packet size and block width were reduced around 60% and 40%, respectively.

The block width reduction is lower than the refinement of PAG size, which explains the lower number fraction of misorientation angles around 60° after RCH.

6.5.3 Effect of CGHAZ and ICCGHAZ

After the heat treatment, grains are coarsened by 195% and 237% (in terms of average value), for CGHAZ and ICCGHAZ respectively. The phase fractions are also changed, which leads to an increase of the flow stress. The flow stress is increased by 44% for CGHAZ and by 14% for ICCGHAZ. The average CTOD of CGHAZ is 80% lower and the average CTOD of ICCGHAZ is 35% lower than for the as-received steel. However, the detrimental effect of the coarse grains and high flow stress is not as pronounced as expected, if compared with sensitivity study shown in Fig. 6. 12 & 13. When fitting the cleavage parameter K_{Ia}^{mm}, the effect is reflected by a very high value of K_{Ia}^{mm} for the HAZ, which represents more effective resistance to micro-crack propagation compared with the as-received steel.

This finding cannot be explained by the differences in the lath/block/packet structures within PAGs. Grain boundary misorientation angles for the as-received material and the HAZ are shown in Fig. 6. 17, which have no significant difference. In [30], M-A constituents are found along the propagation path of secondary cracks by EBSD analysis, and some M-A constituents are observed to deflect the crack. Kernel Average Misorientation (KAM) maps have been measured for the HAZ in [30]. According to the KAM maps, the M-A constituents are the areas with the largest KAM values, indicating a large strain located in M-A constituents. It is a consequence of the residual stresses induced during phase transformation to martensite and the retention of austenite during cooling. The residual stress is compressive in M-A constituents and is tension in the matrix surrounding the M-A constituents [22]. When a crack interacts with M-A constituents, the compressive stresses within M-A constituents can reduce the stress intensity, which possibly explains the crack arrest events in HAZ.
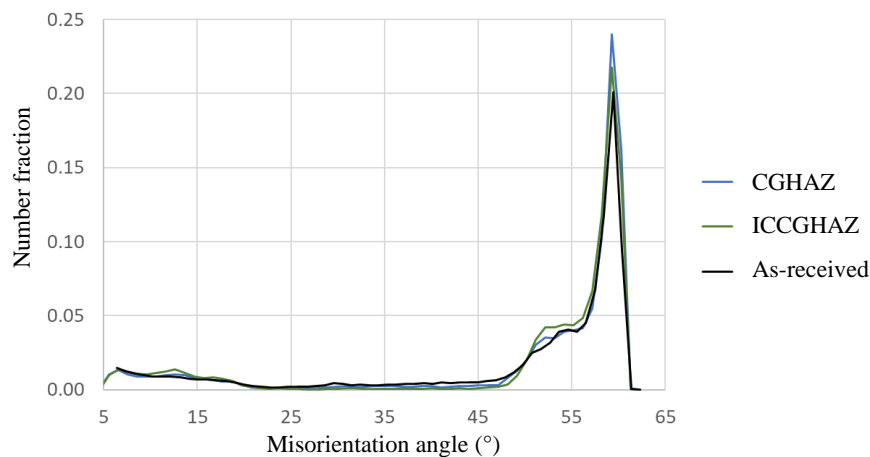

Fig. 6. 17 Grain boundary misorientation angle of HAZ compared to as-received steel [30]

The residual stress in M-A constituents may also have effects on the initiation stage and the propagation of micro-cracks across particle/matrix interface. For example, the residual stress in matrix around the M-A is tension and leads to lower K_{Ia}^{pm}, while the compressive residual stress in M-A leads to higher σ_H^C. The assumption of constant K_{Ia}^{pm} and σ_H^C, which is used in the modelling of HAZ materials, may be violated if the residual stresses are different between CGHAZ and ICCGHAZ. It can be observed that the quality of fittings of simulated HAZs (Fig. 6. 12) are in general worse than the fittings of as received (Fig. 6. 10) and RCH steel (Fig. 6. 11). Not considering the effect of residual stress is a possible cause for the poorer match between experimental and simulation results of HAZ materials.

6.6 Conclusions

In this research, a microstructure-based method with input from Finite Element Analysis is used to model the cleavage behavior of heat treated S690 QT steel at -100°C and -40°C. Cleavage simulations of steel after rapid cyclic heating and heat affect zones are performed. By simulating cleavage fracture of various microstructures and comparing with experiments, the effect of different types of microstructures on cleavage is quantitatively estimated. The following conclusions are highlighted:

- The fitted cleavage parameter K_{Ia}^{mm} decreases 10% after RCH. The experimental improvement of toughness based on grain size is 80% of what would be expected based on multi-barrier simulations. After RCH, the block width reduction is lower than the refinement of PAG size, which is the reason for the lower number fraction of high-angle misorientation boundaries and less effective improvement on fracture toughness.

- The fitted cleavage parameter K_{Ia}^{mm} of HAZs is more than 40% higher than of the as-received steel, which represents effective resistance to micro-crack propagation. The fitted K_{Ia}^{mm} of ICCGHAZ is 13-18% lower than the value of CGHAZ. The more pronounced crack arrest events in HAZ are likely to be explained by the reduction of crack tip stresses due to the interaction with residual compressive stresses in M-A.

- It is not determined if M-A or inclusions are the dominant hard particles that initiate the primary cleavage cracks for the HAZ specimens. While assuming that M-A initiates the microcracks slightly improves the fitting to shallow-cracked specimens of ICCGHAZ, numerical simulations show that reducing or refining inclusions more effectively improves fracture toughness than reduction or refining M-A.

The effectiveness of grain refinement through a simple heat treatment route to improve cleavage fracture is assessed. It reveals how model parameters should be adjusted to account for changes in prior austenite grain sub-structures, which may assist in the fracture behaviour prediction for the

6

improvement of design for high strength steels. The degradations of toughness in CGHAZ and ICCGHAZ are studied considering the changes in grain structure, brittle particles, and yield properties, through both experimental and modeling approaches. It shows that the influence of M-A constituents in HAZs on crack propagation should be studied.

The HAZ specimens in the current paper are produced with Gleeble heat treatment and are considered as homogenous in the model. The work here will enable future work in which macroscopically heterogeneous weld zone are modeled. When the method is applied on an actual weld, the gradient of microstructure and stress should be included. In addition, the current method has the following limitations that should be investigated further:

- This paper only studies pure cleavage; the interaction with ductile fracture is not considered.
- The cleavage parameter K_{Ia}^{mm} used in the current model is found to be temperature dependent. The micromechanism to explain this temperature dependence can be further explored.
- The current model does not directly account for the morphology of M-A constituents and residual stress distributions in/around them.

6

References

[1] EN 1011, CEN (2009). Welding – Recommendations for welding of metallic materials.

[2] Miyata, T., Yang, R. C., Otsuka, A., Haze, T., & Ahira, S. (1989). Cleavage fracture of steels with fine grained ferrite, coarse grained bainitic and martensitic. Advances in fracture research Proceeding of the seventh international conference of fracture. 2563-2571.

[3] Lee, S., Kim, S., Hwang, B., Lee, B. S., & Lee, C. G. (2002). Effect of carbide distribution on the fracture toughness in the transition temperature region of an SA 508 steel. Acta Materialia, 50(19), 4755–4762.

[4] Zhou, M. W., & Yu, H. (2012). Effects of precipitates and inclusions on the fracture toughness of hot rolling X70 pipeline steel plates. International Journal of Minerals, Metallurgy and Materials, 19(9), 805–811.

[5] Li, X., Ma, X., Subramanian, S. V., Shang, C., & Misra, R. D. K. (2014). Influence of prior austenite grain size on martensite-austenite constituent and toughness in the heat affected zone of 700MPa high strength linepipe steel. Materials Science and Engineering A, 616, 141–147.

[6] Trampus, P. (2007). Micro structural aspects of unstable crack propagation in ferritic steels. Materials Science Forum, 537-538, 465-472.

[7] Morrito, S., Saito, H., Ogawa, T., Furuhara, T., Maki, T. (2005). Effect of austenite grain size on the morphology and crystallography of lath martensite in low carbon steels. ISIJ Int., 45, 91–94.

[8] Morris, J.W., Guo, Z., Krenn, C.R., Kim, Y.H. (2001). The limits of strength and toughness in steel. ISIJ Int., 41, 599–611.

[9] Miller, R.L. (1972). Ultrafine-grained microstructures and mechanical properties of alloy steels. Metall. Mater. Trans., 3, 905–912.

[10] Kim, H.J., Kim, Y.H., Morris, J.W. (1998). Thermal mechanisms of grain and packet refinement in a lath martensitic steel. ISIJ Int 38, 1277–1285.

[11] Song, R., Ponge, D., Raabe, D. (2005) Mechanical properties of an ultrafine grained C-Mn steel processed by warm deformation and annealing. Acta Mater 53, 4881–4892.

[12] Park, M.H., Shibata, A., Tsuji, N. (2020) Challenging Ultra Grain Refinement of Ferrite in Low-C Steel Only by Heat Treatment. Front Mater 7, 1–10.

6

[13] Li, X., Zhao, J., Dong, L., et al (2020) The significance of coherent transformation on grain refinement and consequent enhancement in toughness. Materials (Basel) 13, 1–15.

[14] Smoljan, B. (2004) An analysis of combined cyclic heat treatment performance. J Mater Process Technol 155–156, 1704–1707.

[15] Morito, S., Tanaka, H., Konishi, R., Furuhara, T., Maki, T. (2003) The Morphology and Crystallography of Lath Martensite in Fe-C Alloys. Acta Mater., 51, 1789–1799.

[16] Liu, D., Luo, M., Cheng, B., Cao, R., Chen, J. (2018). Microstructural Evolution and Ductile-to-Brittle Transition in a Low-Carbon MnCrMoNiCu Heavy Plate Steel. Met. Mater. Trans. A, 49, 4918–4936.

[17] Shibanuma, K., Nemoto, Y., Hiraide, T., Suzuki, K., Sadamatsu, S., Adachi, Y., & Aihara, S. (2018). A strategy to predict the fracture toughness of steels with a banded ferrite–pearlite structure based on the micromechanics of brittle fracture initiation. Acta Materialia, 144, 386–399.

[18] Rodríguez-Martín, R., Ocaña-Arizcorreta, I., & Martín-Meizoso, A. (2005). Modelling cleavage fracture in high strength steels and their welds. Materials Science Forum, 482, 171–174.

[19] Jiang, Q.M., Zhang, X.Q., Chen, L.Q. (2016). Weldability of 1000 MPa grade ultra-low carbon bainitic steel, J. Iron Steel Res. Int. 23, 705–710.

[20] Lee, S., Kim, B.C., Lee, D.Y. (1989) Fracture mechanism in coarse grained HAZ of HSLA steel welds. Scr Metall 23, 995–1000.

[21] Mohseni, P., Solberg, J.K., Karlsen, M., et al (2012) Investigation of mechanism of cleavage fracture initiation in intercritically coarse grained heat affected zone of HSLA steel. Mater Sci Technol 28,

[22] Davis, C.L., King, J.E. (1994) Cleavage Initiation in the Intercritically Reheated Coarse-Grained Heat-Affected Zone , Part I . Fractographic Evidence. Metall Mater Trans A, 25A, 563–573.

[23] Lee, S.G., Kim, B., Sohn, S.S., et al (2019) Effects of local-brittle-zone (LBZ) microstructures on crack initiation and propagation in three Mo-added high-strength low-alloy (HSLA) steels. Mater Sci Eng A, 760,125–133.

[24] Li, Y., Baker, T.N. (2010). Effect of morphology of martensite-austenite phase on fracture of weld heat affected zone in vanadium and niobium microalloyed steels. Mater Sci Technol 26, 1029–1040.

6

[25] Vassilaros, M.G. (1990). Fracture Behavior of Ultra-Low-Carbon Steel Plate and Heat-Affected Zone. DTIC report, ADA235638.

[26] Jiang, Q., Bertolo, V. M., Popovich, V.A, Sietsma, J., & Walters, C.L. (2022). Microstructure-informed statistical modelling of cleavage fracture in high strength steels considering through-thickness inhomogeneities. Engineering Fracture Mechanics, 267, 108432.

[27] Martín-Meizoso, A., Ocaña-Arizcorreta, I., Gil-Sevillano, J., & Fuentes-Pérez, M. (1994). Modelling cleavage fracture of bainitic steels. Acta Metallurgica Et Materialia, 42(6), 2057–2068.

[28] Lambert-Perlade, A., Gourgues, A. F., Besson, J., Sturel, T., & Pineau, A. (2004). Mechanisms and modeling of cleavage fracture in simulated heat-affected zone microstructures of a high-strength low alloy steel. Metallurgical and Materials Transactions A, Physical Metallurgy and Materials Science, 35(13), 1039–1053.

[29] Bertolo, V. M., Jiang, Q., Vilasi, L., Walters, C.L., Sietsma, J., & Popovich, V.A. Rapid Cyclic Heating Effects on Grain Refinement, Microstructure and Cleavage Fracture Toughness of a S690 High Strength Steel. Materials Science and Engineering A. 868, 144762.

[30] Bertolo, V. M., Jiang, Q., Terol Sanchez, M., Riemslag, A.C, Walters, C.L., Sietsma, J., & Popovich, V.A. Cleavage Fracture Micromechanisms in Simulated Heat Affected Zones of S690 High Strength Steels. Materials Research and Technology. 23, 1919-1933.

[31] De Hoff, R.T. (1962). The determination of the size distribution of ellipsoidal particles from measurements made on random plane sections. Trans TMS-AIME, 224, 474–486.

[32] ISO 12135. (2018). Metallic materials - Unified method of test for the determination of quasistatic fracture toughness.

[33] Jiang, Q., Bertolo, V.M., Popovich, V.A., Sietsma, J., & Walters, C.L. (2021). Relating local stress on a hard microstructural inclusion from far-field stress on matrix to understand cleavage fracture in high strength steel. International Journal of Fracture, 232, 1–21.

[34] Bertolo, V. M., Jiang, Q., Scholl, S., Petrov, R., Hangen, U., Walters, C.L., Sietsma, J., & Popovich, V.A. (2022). A comprehensive characterisation and quantification of the multiphase microstructure of a thick-section high strength steel. Journal of Materials Science, 57, 7101–7126.

6

[35] Wallin, K. (1998). Master curve analysis of ductile to brittle transition region fracture toughness round robin data: The "EURO" fracture toughness curve. VTT Technical Research Centre of Finland. VTT Publications No. 367

[36] Kawata, I., Nakai, H., & Aihara, S. (2018). Experimental evaluation of effective surface energy for cleavage microcrack propagation across grain boundary in steels. Acta Materialia, 150, 40–52.

[37] Martin, J. I. S. (1999). Determination of energetic parameters controlling cleavage fracture in a Ti-V microalloyed ferrite-pearlite steel. Acta Metallurgica, 40(4), 459–464.

6

6

7

General discussions and conclusions

The aim of this thesis is to provide a framework for the modelling of macroscopic cleavage fracture in high strength steel based on microstructural parameters. In this section, the general discussions and conclusions are outlined. The detailed conclusions have been presented within each chapter.

A framework is proposed in Chapter 4 of this thesis to calculate the probability of cleavage failure in high strength steels with complex multiphase microstructures. The framework quantifies the relationship between microscale cleavage events and macroscale fracture toughness in a decoupled method, by incorporating microstructural information with continuum level stress-and-strain field from finite element analysis. It is developed from a multi-barrier theory with particular intention to include the effect of plastic strain and deactivation of hard inclusions. An accurate determination of the local stress on the inclusions is needed for this model. Chapter 3 presents analytical equations to quantitatively calculate the stress on a hard inclusion from far-field stress on a matrix. The analytical equations account for the inclusion shape, the inclusion orientation, the far-field stress state and matrix material properties. Finite element modelling of a representative volume element containing a hard inclusion shows that the equations provide an accurate representation of the local stress state. The analytical solution proposed in Chapter 3 to quantitively determine the stress on a microstructural hard inclusion avoids costly numerical simulations when the features of microstructural inclusions vary widely in the steel. It provides an efficient estimation of fracture of inclusions in the cleavage process, and can be used for identification of anisotropic fracture behavior. The maximum error of $\sigma_{1,inclu}$-$\sigma_{1,matrix}$ is 25% for the studied cases. Because the solution can account for multiple parameters, it can be used not only for a particular material but in general for high strength steels containing heterogeneous microstructures and under various loading patterns.

The framework proposed in Chapter 4 is first validated with examples of specimens taken from S690 QT steel plate fractured at -100°C. Centreline segregation bands (CLs) appear in the middle section specimens, containing smaller grains and elongated inclusion clusters. The model is capable to

identify grain boundaries rather than particle/matrix interfaces as the barrier to microcrack propagation for the sample steel. Two modelling approaches are compared to discuss the effect of CLs in cleavage modelling. A sensitivity study has been performed to explore the influence of volume fractions, yield strength, and spacing of CLs. The results show that the effects of 18% higher yield stress and 22% finer grain size inside the segregation bands approximately cancel, while Niobium carbide inclusions that have 19% lower fracture strength characterize the detrimental effect of CLs. The embrittlement from CLs (i.e., median CTOD is 0.043 mm for top section and 0.012 mm for middle section) can only be adequately reflected if the inhomogeneities of the fracture parameters are accounted for. This conclusion leads to the general suggestion that the cleavage parameter associated to a local brittle microstructure should not be homogenized outside the local brittle zone.

One of the challenges for multi-barrier cleavage models is the strong variations of cleavage parameters across different types of steels. The source of the variations have not been studied in a systematic way in the literature. The modelling approach proposed in Chapter 4 is applied to determine the cleavage parameters across different types of steels in Chapter 5. Cleavage parameters are compared among three tempered bainitic (S690) steels, an as-quenched martensitic steel, and a ferritic steel. The determined cleavage parameters presents a high degree of consistency (15% variation of K_{Ia}^{mm} and 10% variation of σ_H^C) among the three bainitic steels, which allows the further application on microstructure designs to control macroscopic toughness. It is also found that the grain boundary cleavage parameter depends on the hierarchical grain structure while the particle fracture parameter depends on particle morphology and composition. When choosing a process for controlling cleavage toughness of high strength steel, these effects should be considered for the optimisation of microstructural parameters.

One important application of the proposed method is to provide better modelling of the relationship between toughness and the microstructures resulting from heat treatments. The modelling approach proposed in Chapter 4 is used to model the cleavage behaviour of heat treated S690 steel in Chapter 6. Cleavage simulations of steels subjected to heat treatments that cause grain refinement or simulate heat affected zones are performed, and are compared with experiments. It is found that K_{Ia}^{mm} decreases 10% after RCH. The experimental improvement of toughness from grain refinement is 80% of what would be expected based on the model. The 20% difference is due to the lower number fraction of high-angle misorientation boundaries. The fitted cleavage parameter K_{Ia}^{mm} of HAZs is more than 40% higher than of the as-received steel, which represents effective resistance to micro-crack propagation. The hypothesis is that the residual compressive stress in martensite-austenite constituents leads to more effective resistance to micro-crack propagation in heat affected zones. The findings in Chapter 6 provide recommendations on improving the fracture toughness of heat treated high strength steels. It reveals that the model parameters should be adjusted to account for changes in prior austenite grain sub-structures, which is important for fracture behaviour prediction in the improvement of design for high

7

strength steels. It provides the insight that the presence of M-A constituents in HAZs should be studied on influencing crack propagations in addition to crack initiation.

This thesis presents a physics-based statistical method to model the quantitative relationship between multiple critical microstructural parameters and macroscopic fracture toughness of high strength steels. Physical complexity governing cleavage crack initiation and propagation is studied with the model for different types of steels and steels to which heat treatments have been applied. The proposed method is a functional tool for toughness optimization, where microstructural aspects, structural geometry and performance constraints can be simultaneously taken into account.

This dissertation focuses on cleavage fracture, and all the specimens studied are fractured in a brittle model. Ductile fracture is not included in the model. However, a ductile failure model may also benefit from the analytical solution proposed in Chapter 3 to determine when decohesion occurs between the hard particle and the surrounding matrix. To model the ductile-to-brittle transition, the current model requires incorporation of ductile failure models and an estimation of temperature dependence over the transition temperature range. The cleavage parameter K_{Ia}^{mm} used in the current model is found to be temperature dependent. The mechanism to explain this temperature dependence should be further explored at microscale incorporating plasticity models.

In addition, the present modelling approach has the following limitations that can be further investigated:

- While the current method includes corrections on yield properties depending on strain rate, dynamic fracture behaviour is not investigated. There are several factors need to be considered if the current method is extended for dynamic fracture, for example heat release near crack tip and ductile tearing in advance of cleavage.
- This dissertation studies the most common type of cleavage fracture, the Mode I fracture state, in which the crack propagates under tensile stress in the open mode. However, mixed mode fracture is worth to be further investigated by including the shear stress into the driven forces.
- The current model does not account for local fluctuations of stresses, due to phase distribution and/or residual stress distributions. The local fluctuation of stress can result in additional randomness and may lead to a lower accuracy. The influence both hard particles and the matrix. More micro-scale investigations can facilitate the improvement of the model performance.
- The present model is validated with experimental fracture tests in laboratory conditions. The current method would be suitable for further application on an actual weld if the gradient of microstructure and stress is included.

7

Acknowledgement

At the end of thesis, I would like to acknowledge and express my gratitude to all the parties that supported me during the research from 2018-2022.

I am very grateful for the guidance from my supervisors at TU Delft. I would like to thank my promotor Prof. Jilt Sietsma. With a supportive mentoring style and cautious scientific attitude, you always offer prompt and salient help to me. In addition to the guidance on research, you also have a genuine concern for students and colleagues, promoting departmental gatherings and culture sharing that become departmental traditions. Dr. Vera Popovich, I hold deep appreciation for your great effort in daily supervising me and managing the project. In addition to your expertise in experimental mechanics and microstructures, I also learn valuable communication and coordination skills from you. I would like to express gratefulness to Dr. Carey Walters, my daily supervisor. You patiently explore the research details with me, always motivate me to be critical and creative, and continually help me to improve writings and presentations. All my three supervisors are of great importance in my PhD journey, for guiding my research and being my career role models.

I would also like to acknowledge the invaluable feedback and insightful discussions provided by the external committee members: Prof. Bert Sluijs, Prof. Milan Veljkovic, Prof. Jacques Besson, and Prof. Jonas Faleskog. It is my pleasure to present the work and receive your comments.

This thesis is part of the Micro-Tough research project (n. 16350) from the Dutch Research Council (NWO). I would like to acknowledge the great support from the consortium of partners that include Allseas Engineering, Dillinger, Lloyd's Register, The Dutch Ministry of Defence, and TNO. I would like to thank all the experts involved in the project meetings, including Bin, Natalia, Sebastian, Kinshuk, LiLi, Li, Andre, Weihong, Martijn, Okko, Casper, and Mario. I would like to thank the former promotor Ian Richardson for initiating Micro-Tough and supervising the first six months of the project.

Throughout the course of my project, I received a great deal of support and assistance from numerous individuals. I would like to thank Ton and Elise for training me on mechanical testing; Richard for solving software issues; Konstantina and Jesus for sharing knowledge in microscale mechanical simulations; Okko for sharing experience in fracture modelling; Arthur for sharing knowledge on nanoindentation; Kaustubh and Vishnu for performing part of experimental tests; Sakari for providing your experimental data and being a co-author; Wei for sharing experience in preparing dissertation and defence; and Marcelle for reviewing the Dutch summary of this thesis. The greatest appreciation goes to my research partner Virgínia. You are devoted to the experimental work of Micro-

Curriculum Vitae

Quanxin Jiang

Born on 17 April 1994, Jinan

Education

10. 2018 - 3. 2023	Ph.D. in Materials Science and Engineering
	Delft University of Technology, Delft, the Netherlands
9. 2016 - 8. 2018	Master of Science in Civil Engineering
	Delft University of Technology, Delft, the Netherlands
9. 2012 – 6. 2016	Bachelor of Science in Civil Engineering
	Zhejiang University, Hangzhou, China

Working Experience

1. 2023 - Present	Credit Risk Model Validator
	ABN AMRO, Amsterdam, the Netherlands
11. 2017 - 8. 2018	Research Intern
	TNO, Delft, the Netherlands

List of Publications

Journal papers

1. **Jiang, Q.**, Bertolo, V. M., Popovich, V. A., Sietsma, J., Walters, C. (2023). *Microstructure-based cleavage modelling to study grain size refinement and simulated heat affected zones of S690 high strength steel*. Submitted to Materials Science and Engineering A.

2. **Jiang, Q.**, Bertolo, V. M., Pallaspuro, S., Popovich, V. A., Sietsma, J., Walters, C. (2023). *Microstructure-based cleavage parameters in bainitic, martensitic, and ferritic steels*. Accepted by Engineering Fracture Mechanics.

3. **Jiang, Q.**, Bertolo, V. M., Popovich, V. A., Sietsma, J., Walters, C. (2022). *Microstructure-informed statistical modelling of cleavage fracture in high strength steels considering through-thickness inhomogeneities*. Engineering Fracture Mechanics. 267, 108432.

4. **Jiang, Q.**, Bertolo, V. M., Popovich, V. A., Sietsma, J., Walters, C. (2021). *Relating matrix stress to local stress on a hard microstructural inclusion for understanding cleavage fracture in high strength steel*. International Journal of Fracture. 232, 1–21.

Conference proceedings

1. **Jiang, Q.**, Bertolo, V. M., Popovich, V. A., Sietsma, J., Walters, C. L. (2022). *Numerical modelling of cleavage in high strength steels with parametric study on microstructures*. Procedia Structural Integrity, Proceeding of European Conference on Fracture 2022. 42, 465-470.

2. **Jiang, Q.**, Bertolo, V., Popovich, V. A., Walters, C. L., (2019). *Recent Developments and Challenges of Cleavage Fracture Modelling in Steels: Aspects on Microstructural Mechanics and Local Approach Methods*. Proceedings of the ASME 2019 38th International Conference on Ocean, Offshore and Arctic Engineering. Volume 4, OMAE2019-95464, V004T03A033.

Co-authored articles

1. Bertolo, V., **Jiang, Q.**, Terol Sanchez, M, Riemslag, T., Walters, C., Sietsma, J., Popovich, V. (2023). *Cleavage Fracture Micromechanisms in Simulated Heat Affected Zones of S690 High Strength Steels*. Materials Science and Engineering A. 868, 144762.

2. Bertolo, V., **Jiang, Q**., Vilasi., L., Riemslag, T., Scott, S., Walters, C., Sietsma, J., Popovich, V. (2023). *Grain Refinement by Rapid Cyclic Heating and its Effect on Cleavage Fracture Behaviour of an S690 High Strength Steel*. Materials Research and Technology. 23, 1919-1933.

3. Bertolo, V., **Jiang, Q.**, Tiringer, U., Walters, C., Sietsma, J., Popovich, V. (2022). *Cleavage fracture micromechanisms in thick-section quenched and tempered S690 high-strength steels*. Journal of Materials Science, 57, 20033–20055.

4. Bertolo, V., **Jiang, Q.**, Scholl, S., Petrov, R. H., Hangen, U., Walters, C., Sietsma, J., Popovich, V. (2022). *A comprehensive quantitative characterisation of the multiphase microstructure of a thick-section high strength steel*. Journal of Materials Science, 57, 7101–7126.

5. Ghorbanpour, S., Deshmukh, K., Sahu, S., et al. (2022). *Additive manufacturing of functionally graded inconel 718: Effect of heat treatment and building orientation on microstructure and fatigue behaviour*. Journal of Materials Processing Technology. 306, 117573.

6. Ghorbanpour, S., Sahu, S, Deshmukh, K, et al. (2021). *Effect of microstructure induced anisotropy on fatigue behaviour of functionally graded Inconel 718 fabricated by additive manufacturing*. Materials Characterization 179, 111350.

7. Bertolo, V., **Jiang, Q.**, Walters, C. L., Popovich, V. A., (2020). *Effect of Microstructure on Cleavage Fracture of Thick-Section Quenched and Tempered S690 High-Strength Steel*. Characterization of Minerals, Metals, and Materials 2020. The Minerals, Metals & Materials Series. Springer, Cham. 155-168.